Università
Ca'Foscari
Venezia

cmcc
Centro Euro-Mediterraneo
sui Cambiamenti Climatici

Corso di Dottorato di ricerca in
Scienza e Gestione dei Cambiamenti Climatici
Ciclo XXIX

Tesi di Ricerca

A multi-scale energy and vorticity analysis of coupled atmosphere-ocean dynamics in the Mediterranean Sea

Settore scientifico disciplinare di afferenza: GEO/12

Coordinatore del dottorato:
Prof. Carlo Barbante

Supervisore:
Dr. Silvio Gualdi
María del Mar Chaves Montero
Matricola 956100

Co-supervisore:
Dottoranda:

Acknowledgements

This work would not have been possible without the contribution of a number of people, to who I would like to express my gratitude.

My sincere thanks goes to my thesis advisors, Dr. Silvio Gualdi and Dr. Paolo Oddo, who patiently guided me during these years. Thanks for giving me the opportunity, for the lessons I already learned from you, and for the ones that only time will show me.

I would like to acknowledge Prof. San Liang and his students, who provided the MS-EVA codes and contributed with valuable comments.

I am grateful to Prof. Pierre Lermusiaux, who provided me the chance to join his group at the Massachussets Institude of Technology. I am thankful and indebted to him for his time and the precious discussions. Thanks also to the MSEAS group: Dr. Patrick Haley, Dr. Chris Mirabito and the guys (and girl) in the group.

My gratitude extends to the external reviewers of this thesis, Prof. Piero Lionello and Prof. Marcello Vichi, whose insightful comments helped to improve this manuscript.

This dissertation would not have been possible without funding from the University Ca' Foscari Venice and the Euro-Mediterranean Center on Climate Change (CMCC Foundation).

My warmest thanks to my colleges and students at CMCC who made the day-to-day a great experience. They provided moral support and assisted me in many of the problem that any PhD student finds in his way. May I say that they, together with the rest of my dear italian (or "adopted italian") friends, have made my stay in this country so valuable.

I cannot forget to thank the friends I have all around the world, who directly or indirectly supported me in this venture. Distance have not been an impediment for being always close.

Last, but not least, I would not be here without the support of my family. To them I will refer in my own language.

Gracias a mi familia, los que stán y los que nos dejaron, y a mi pareja, sin los cuales no sería quien soy. Vuestro apoyo ha sido incondicional todos estos años. Gracias porque, aun cuando yo no lo viera, siempre confiasteis en mi.

To the memory of my mother...
and to my father.

STUDENT: ID NUMBER:
María del Mar CHAVES MONTERO 956100

PHD PROGRAM IN
SCIENCE AND MANAGEMENT OF CLIMATE CHANGE
XXIX CYCLE

A multi-scale energy and vorticity analysis of coupled atmosphere-ocean dynamics in the Mediterranean Sea

ABSTRACT

The Mediterranean Sea is a small yet interesting basin of study. The number of external forcings acting on it, together with its topography and other local factors confer unique characteristics to the basin. As a consequence, its general circulation is complex and highly variable, with features at diverse and interacting scales. One way to explain the dynamics of ocean and atmospheric processes is trough energy analysis. At this respect, the description of the energy budgets of the Mediterranean is a relatively unexplored topic. The aim of this study is to improve the understanding of physical processes involving diverse scales interaction in the Mediterranean Sea by looking at the energy budgets. Another aim is to define a methodology and tools for an innovative approach to assess models performance based on a multi-scale energy analysis.

Here we make use of two methodologies to evaluate the energy distribution based in two different scale divisions. A decomposition of the fields in a mean and its deviation is the base of what we call classic energy analysis, since this is the most used method. A more innovative method based on spectral decomposition (Multi-Scale Energy analysis) is also used. The approach gives us a means to determine the partition and the transfers of energy between the different scales, and to identify the role of other processes involved in the energy distribution (external forcing, advection, conversion between kinetic and potential energy).

The local energy patterns are inspected for a series of increasingly complex experiments. The methodologies were first validated using an idealized instability model. Two cases are inspected: one with a growing perturbation and a stable flow. The energy distribution evidenced three processes: a redistribution of energy among the domain via advection and pressure work, an energy conversion from APE to KE, and a source of energy via baroclinic conversion as the

triggering mechanism for the growing perturbation. The analyses were coherent between the types of methodologies used. Second, an idealized simulation performed with a state of the art ocean model (NEMO) is used for a first evaluation of energy paths under controlled conditions. The simulations reproduce the generation of a coastal upwelling by a favorable wind forcing in a motionless ocean, under three different topographies. The energy distribution evidences three processes important during the formation of a coastal upwelling: horizontal advection, buoyancy and scale transferences. Mixed instabilities are potentially produced. The topography affect the energy by enhancing and constraining the circulation, and this is reflected in the energy distribution.

Finally, as a realistic study case, we assess the dynamics of an upwelling event along the southern coast of Sicily. For this purpose, we use a high-resolution, coupled atmosphere-ocean regional model (NEMO-COSMO) to simulate the Mediterranean Region. The dynamics of the upwelling revealed in the idealized experiment are contained in the realistic experiment. The presence of a background circulation, and the more complex physics in the realistic experiment lead to some differences in the energy distribution.

Contents

List of Figures

Introduction and motivation

The Mediterranean Sea is a semi-enclosed basin, situated at mid latitudes. In spite of its small size, all the major forces affecting the larger oceans (air-sea interactions, wind stress, buoyancy fluxes) are present in the Mediterranean. Its general circulation is complex and highly variable, with features at diverse and interacting scales (basin, sub-basin and mesoscale) (Robinson et al., 2001). Considering the limited water exchanges through straits, the influence of topography and coasts, and the water mass formation and transformation, the result is a unique field of study.

Because of its position, the Mediterranean is affected by interactions between mid-latitudes and tropical processes. This makes it potentially vulnerable to climatic changes. Taking into account the high population of its coastal areas, the Mediterranean region is one of the *hot-spots* of climate change (Giorgi and Lionello, 2008). Therefore, having a comprehensive understanding of the physical processes affecting the Mediterranean circulation is not only interesting from a scientific point of view, but is also essential in order to provide accurate climate predictions. Since climate is closely related to the sources and sinks of energy, improving our knowledge about the mechanisms controlling the energy budgets at different spatio-temporal scales is crucial.

There are different types of energy: mechanical energy and internal energy (Gill, 1982; Vallis, 2006). The mechanical energy is divided into gravitational potential energy (GPE) and kinetic energy (KE). The potential energy actually is better represented by the available potential energy (APE). The concept was introduced by Lorenz (1955), who defined it as the difference of potential energy with respect to a reference state of minimum energy where the mass is adiabatically rearranged to a reference state with density surface parallel to geopotential surfaces. Energy can transform from one type to the other, so all of them are interconnected.

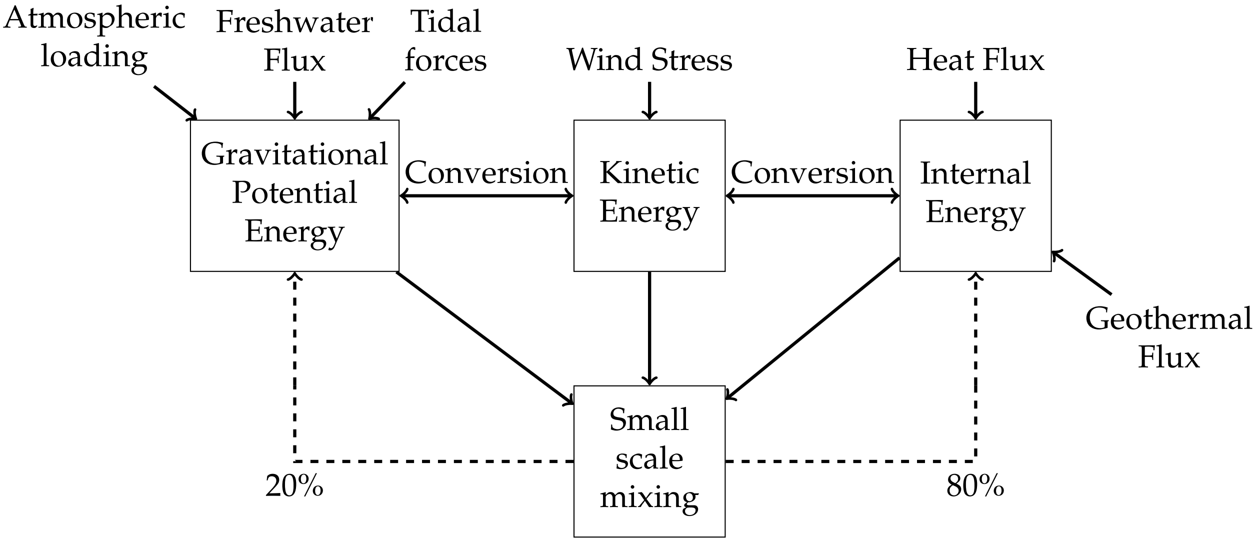

Figure 1: Energetic diagram of the ocean circulation. After Huang (2004).

The relevant equations for energy can be obtained from the momentum and density equations. The equations are usually summarized by energy diagrams as the one in Figure 1, where the main sources of energy for the ocean are indicated. These equations are diagnostic and not predictive, which is maybe one of the reasons why energy studies have been disregarded in comparison with studies of the fluid motion. Estimations of the energy content of each reservoir, and their sources/sinks have been done by many authors (e.g, see review by Ferrari and Wunsch (2008)). However, there is still much to do, specially at the regional level.

When considering energy studies, little attention has been put on the Mediterranean Region. Many studies have been done regarding its circulation, but the energy budgets underpinning the dynamical processes of the basin are not well known. Eddy kinetic energy measures from altimeters corroborate the large energy content of the mesoscale circulation (Pujol and Larnicol, 2005), but they are constrained to the surface layer. Studies considering complete energy budgets either at basin or limited areas are scarce (Korres et al. (2000); Sorgente et al. (2011)).

The aim of this work is to improve our understanding of physical processes involving different scales interaction occurring in the Mediterranean. In order to do this, we investigate the energy paths, transfers and cascades at different scales. In particular, we use some upwelling events as study case. Furthermore, it will provide a diagnostic tool to assess the model's behaviour.

The thesis is organized as follows:

In Chapter 1 we explore the main methods used in energy studies to decompose the field. We describe the main methods employed in literature, and comment their strengths and weaknesses in order to choose the most suitable for our purpose.

Chapter 2 is a validation of the methodology. We studied the energy dynamics produced by an analytical model for baroclinic instability, and compare the results obtained with the two methods used in this study.

Once the methodology was validated, we designed a series of increasingly complex experiments to which apply the energy analysis.

Chapter 3 focus on a set of idealized experiment reproducing a simple upwelling. The main features related to the upwelling circulation are described. The experiments also explore the effect of different topographies on the energy.

In Chapter 4 we performed a realistic experiment. We used a regional atmosphere ocean coupled model to simulate the Mediterranean Region. We investigated the energy distribution during an upwelling event, and compared them with the ones obtained in the idealized experiments.

Finally, the thesis concludes with a short summary of the findings and future work.

Chapter 1

Energy and scale decomposition

1.1 Introduction

Climate processes occur in a wide range of lengths and time scales, varying from second to years and from tenths millimeters to thousands of kilometers, and all these signals are unavoidably mixed in nature. The Navier-Stokes equations describing the fluid motions reproduce a great variety of processes that occur simultaneously in fluids at different time and length scales. The fact that all the processes are mixed makes difficult their study, so scientists make use of diverse techniques to disentangle their dynamical mechanisms and evaluate them separately. The separation of the field in scales is hence a natural choice in the study of geophysical flows.

In the present work, we use a new methodology called Multiscale Energy and Vorticity Analysis (hereafter, MS-EVA), developed by Liang and Robinson (2005, 2007), which allows to study the energy contain and transferences between different scales. The scale decomposition in MS-EVA is achieved with the use of a functional analysis called Multiscale Window Transform (Liang and Anderson, 2007). However, this is not the only approach for decomposing scales. There are other methods for function decomposition with different mathematical or empirical approaches, degree of complexity and areas of application. The choice of the method profoundly affects the way to approach the problem and hence the solutions, so it has to be carefully done.

In this chapter, we review some of the methodologies found in literature, including the one assessed in this thesis. We focus on the ones for which energy equations have been explicitly formulated for atmospheric or oceanic flows. We will briefly describe each method, and discuss their strengths and limitations.

1.2 The equations of motion for the ocean

The fundamental set of equations describing the motion of the ocean and atmosphere are called the Primitive Equations. The Primitive Equations are formulated from the Navier-Stokes equations, which describe the momentum bancealance for a fluid element based on Newton's second law with Coriolis force, under the Boussinesq, incompressible and hydrostatic approximations, and Reynolds-averaged. To fully describe the fluid, more information is needed and equations for the conservation of mass, conservation of thermal energy and a equation of state are also included.

$$\frac{\mathrm{d}\mathbf{u}}{\mathrm{d}t} = -f\mathbf{k} \times \mathbf{u} - \frac{1}{\rho_0}\nabla p + \nabla \cdot (A_m \nabla \mathbf{u}) + F \tag{1.1a}$$

$$\nabla \cdot \mathbf{U} = 0 \tag{1.1b}$$

$$\frac{\partial p}{\partial z} = -\rho g \tag{1.1c}$$

$$\frac{\mathrm{d}T}{\mathrm{d}t} = \nabla \cdot (A_t \nabla T) + F \tag{1.1d}$$

$$\frac{\mathrm{d}S}{\mathrm{d}t} = \nabla \cdot (A_t \nabla S) + F \tag{1.1e}$$

$$\rho(T,S) = \rho(T,S,p) \tag{1.1f}$$

In these equations, the unknowns are the three dimensional velocity $\mathbf{u} = (u\mathbf{i}, v\mathbf{j}, w\mathbf{k})$, the pressure p, the temperature T and the salinity S. f is the Coriolis term and ρ_0 is the reference density. $\mathrm{d}/\mathrm{dt} = \partial/\partial t + u(\partial/\partial x) + v(\partial/\partial y) + w(\partial/\partial w)$ is the total derivative and $\nabla = (\partial/\partial x, \partial/\partial y, \partial/\partial w)$ is the divergence operator. A_m and A_t are the eddy viscosity and eddy diffusivity coefficients for momentum and tracers, respectively. F terms represent additional sources, as wind or heat fluxes.

1.3 Reynolds decomposition

From his studies on turbulence, Reynolds (1895) understood that the problem was too complicated to permit a detailed description of the flow. The approach he used was hence aimed at reproducing its statistical properties. Indeed, he proposed the decomposition of any flow variable (ϕ) into a mean part ($\overline{\phi}$) and the fluctuation around the mean (ϕ'):

$$\phi = \overline{\phi} + \phi'$$

The average can be done in different ways. Often, temporal and volume averages are defined as:

$$\overline{\phi} = \lim_{\tau >> 0} \frac{1}{\tau} \int_0^{\tau} \phi(\mathbf{x}, t) dt$$

$$\overline{\phi} = \frac{1}{V} \int_V \phi(\mathbf{x}, t) dV$$

Generally, an ensemble average can be used:

$$\overline{\phi} = \frac{1}{N} \sum_0^n \phi(\mathbf{x}, t)$$

In any case, the average of the fluctuations is, by definition, zero.

The Reynolds decomposition applied to the Navier-Stokes equations are used to parametrize the small scale processes. In the so called Reynolds-Averaged equations, which are part of the Primitive Equations, the viscosity coefficient A_m contains the molecular viscosity and the eddy viscosity, a term arising from the decomposition that takes into account the effect of the nonlinear interaction of the perturbations. The Reynolds decomposition can be further applied on the Primitive Equations in order to obtain the energy equations for the mean and fluctuation flows.

The variables characterizing the flow are decomposed and inserted into the governing equations before taking the average. Let's apply the decomposition rule to the velocity field ($\mathbf{u} = u(\mathbf{x}, t)$) and then substitute into the continuity equation:

$$\nabla \cdot \mathbf{u} = \nabla \cdot (\overline{\mathbf{u}} + \mathbf{u}') = 0 \tag{1.2}$$

When averaging, it follows that both the mean flow and the perturbation are incompressible:

$$\nabla \cdot \overline{\mathbf{u}} = 0\,; \nabla \cdot \mathbf{u}' = 0 \tag{1.3}$$

Now we apply the decomposition to the equation of motion in the Primitive Equations:

$$\frac{\partial \mathbf{u}}{\partial t} + \mathbf{u} \cdot \nabla \mathbf{u} = -\frac{1}{\rho_0} \nabla p - f\hat{k} \times \mathbf{u} + \nabla \cdot (A_m \nabla \mathbf{u}) \tag{1.4}$$

After applying the decomposition to all the variables and averaging, the mean momentum equation looks like:

$$\frac{\partial \overline{\mathbf{u}}}{\partial t} + \overline{\mathbf{u}} \cdot \nabla \overline{\mathbf{u}} = -\frac{1}{\rho_0} \nabla \overline{p} - f\hat{k} \times \overline{\mathbf{u}} + \nabla \cdot (A_m \nabla \overline{\mathbf{u}}) - \overline{\mathbf{u}' \cdot \nabla \mathbf{u}'} \tag{1.5}$$

The total kinetic energy is defined as the sum of the kinetic energy of the mean flow (MKE), and the mean kinetic energy of the perturbation or eddy kinetic energy (EKE):

$$K = \frac{1}{2}\rho_0 \mathbf{u}\cdot\mathbf{u} = \underbrace{\frac{1}{2}\rho_0 \bar{\mathbf{u}}\cdot\bar{\mathbf{u}}}_{MKE} + \underbrace{\frac{1}{2}\rho_0 \overline{\mathbf{u}'\cdot\mathbf{u}'}}_{EKE}$$

The equation for the evolution of the kinetic energy of the mean flow is obtained by multiplying (1.5) by $\overline{\mathbf{u}}$.

$$\frac{\partial MKE}{\partial t} = -\overline{\mathbf{u}}\cdot\nabla MKE - \overline{\mathbf{u}}\cdot\nabla\bar{p} - g\bar{w}\bar{\rho} + \rho_0\Big[-\bar{\mathbf{u}}\cdot(\overline{\mathbf{u}'\cdot\nabla\mathbf{u}'}) + \nabla\cdot(A_m\nabla MKE)\Big] \tag{1.6}$$

Indicating that the local rate of change of MKE is due to advection by the mean flow, the pressure work, conversion between MKE and EKE, and dissipation.

An analogous equation is obtained for the EKE by subtracting (1.5) to (1.4), and multiplying by $\mathbf{u}'$:

$$\begin{aligned}\frac{\partial EKE}{\partial t} =& -\overline{\mathbf{u}}\cdot\nabla EKE - \mathbf{u}'\cdot\nabla EKE - \mathbf{u}'\cdot\nabla p' - g\overline{w'\rho'}\\ &+\rho_0\Big[-\mathbf{u}'\cdot(\mathbf{u}'\cdot\nabla\overline{\mathbf{u}}) + \mathbf{u}'\cdot\overline{(\mathbf{u}'\cdot\nabla\mathbf{u}')} + \nabla\cdot(A_m\nabla EKE)\Big]\end{aligned} \tag{1.7}$$

The local change of EKE is due to advection by the mean and the eddy flow. The rest of the terms are the perturbation pressure work, the conversion between MKE and EKE, the nonlinear interactions of the eddy flow, and dissipation. The interaction term represents a redistribution of energy. It is not a source or sink of energy so does not change the global energy budget. Indeed, this term vanishes under proper averaging.

This method has been widely used. For example, mean and eddy energy equations for the atmosphere are found in Reynolds (1895); Mieghem (1952) or Arakawa (1953), to name some. Its use has surely contributed to the knowledge we have now about atmospheric and oceanic circulations at global scale. However, it presents some limitations.

One is how to calculate properly the average. For stationary flows, or flows varying slowly with respect to the process studied, time-averages are useful. But only if the average is computed over sufficiently long times. Spatial averages are suitable for homogeneous flows. However, since most natural flows are nor stationary or homogeneous, the use of this method can produce energy budgets that are not completely consistent with the dynamics of the flow. An alternative to consider time integrals is to compute the average over regional areas as it was done in Harrison and Robinson (1978). Nevertheless, the selection of appropriate areas to perform the integration, where the interpretation of the energetic terms is meaningful, is difficult. One should define regions whose dynamical behaviour is homogeneous, but diverse between different regions, which is not an easy task. This method has been also used in studying the routes of equilibration in different types of models (e.g. Molemaker et al. (2010)). In this case, averaged mean-fluctuation energy patterns are checked when the statistical equilibrium is reached. Again, this is not the condition we find in real flows. Real flows are time-varying and inhomogeneous in space.

The basis of the Reynolds decomposition, the averaging, implies a loss of information in time and/or space. The locality must be preserved in explaining the energy budgets. In order to overcome the averaging problem, Pinardi and Robinson (1986) formulated a local energy and vorticity analysis (EVA) for a quasigeostrophic model. A version for the primitive equation was also developed by Spall (1989).

Another limitation of the Reynolds approach is that no information is given about the behaviour of the separate scales of eddies, apart from the evolution of mean eddy kinetic energy. Fjørtoft (1953) demonstrated that changes in the kinetic energy of one scale of motion are accompanied by changes in the kinetic energy of eddies of both smaller and larger scales. It is hence desirable to resolve eddy processes splitting the contributions of different scales. With the Reynolds decomposition, the interactions that occur inside the eddy flow are integrated into an averaged quantity, so the inter-scale transferences cannot be explained.

1.4 Spectral Methods

1.4.1 Fourier

With the Fourier decomposition, the problem is approached in a different way. Generally, the analysis consists in the decomposition of real functions $f(x)$ into a linear combination of orthogonal basis, multiplied by some coefficients. For one dimensional functions:

$$f(x) = \int_{-\infty}^{\infty} \hat{f}(\kappa) e^{i\kappa x} d\kappa \tag{1.8}$$

In the case that x is time, κ is the frequency. In the Fourier case, the basis are trigonometric functions, while the coefficients ($\hat{f}(\kappa)$) are:

$$\hat{f}(\kappa) = \int_{-\infty}^{\infty} f(x)e^{-i\kappa x}dx \tag{1.9}$$

With this decomposition we can separate the diverse frequencies composing a signal. As in the Reynolds case, the Fourier decomposition can be applied to the variables into the Navier-Stokes equations by multiplying by the basis and integrating. This was done for the first time by Saltzman (1957), and revisited by Hansen and Chen (1982) and Fournier (2002). The resulting equations are transformed from the physical domain to the domain of wave number, allowing the multi-scale interpretation. In fact, the transformed equations describe the evolution of the single *Fourier modes*.

Energy equations can be derived for the rate of change of energy of disturbances at each wave number (m), and the total kinetic energy:

$$\overline{K} = \sum_{m=1}^{\infty} K_m$$

where $K_m = \frac{1}{2}\hat{\mathbf{u}}_{-\mathbf{m}} \cdot \hat{\mathbf{u}}_{\mathbf{m}}$ is the kinetic energy of each wave number. Schematically, the equation describing the evolution of kinetic energy for a given wave number m is:

$$\frac{\partial K_m}{\partial t} = MK_m + C_m + D_m + TK_m \tag{1.10}$$

MK_m measures the interaction between the mean flow and the individual scales of disturbances; C_m is the conversion between potential and kinetic energy at given wave numbers; D_m is the dissipation, and TK_m measures the transfer of energy between different wave numbers. There is hence a correspondence between the equations in the physical domain and in the frequency domain. The expression (1.10) is analogous to the MKE equation from Reynolds decomposition (1.6), but involving all the scales of disturbance. Specifically, TK_m represents the transfer of KE from wavenumber m to all other nonzero wave numbers. It describes the nonlinear interactions redistributing energy along the spectrum. Therefore, as in the Reynolds case, it vanishes when integrated over the domain.

Fourier analysis, together with Reynolds decomposition, is the most used method for energy analysis. This is in part because Fourier transforms have some useful properties, as orthogonality of modes or energy conservation. Also, many partial differential equations problems are easier to approach using Fourier formulation. The orthogonality is an essential characteristic from the physical point of view. It avoids the information to be "repeated" among the modes, and reduce the number of modes that are necessary to reproduce a function, which is important when truncating the series.

When used to study stationary fields, or flows that have reached an equilibrium, the Fourier analysis gives a "general picture" of how energy flows among scales. It proves a more straightforward understanding of the energy cascade. For example, one of its applications is the study of the dynamical routes towards energy dissipation. However, it does not take into account how this picture can change over time.

Furthermore, the projection into modes implies always a relation between the original function and the analyzing function. This must been taken into consideration when interpreting the transformed fields, because some features can be just mathematical artifacts of the decomposition. Since the basis are periodic, trigonometric functions, Fourier analysis is suited to very regular, periodic signals such as flows that are a superposition of waves, but may not be so effective in a more general case. Moreover, the oscillating character of the trigonometric functions causes the information content to be delocalized among all the spectral coefficients. Local characteristics of the signal become global characteristics of the transform. Hence, Fourier decomposition fails also in the localization.

1.4.2 Wavelet

Localization can be achieved with the use of wavelets. The basic approach is similar to the Fourier transform: we decompose functions into a basis multiplied by coefficients. The coefficients tell how the analyzing function (sines and cosines, or wavelets) have to be weigthed to reconstruct the signal. The computation of the coefficients is also similar: the function and the basis are multiplied, and the integral of the product is computed. The difference is that wavelets allow to divide the field into both, space *and* time. The space-scale division is achieved by squeezing and stretching the analysing function to change the frequency and adapt to the signal.

Generally, the wavelet transform:

$$f(t) = \int_{-\infty}^{\infty} \hat{f}_n^j \psi(2^j t + n) dt \tag{1.11}$$

Where j and n indicate scale and location. The coefficients:

$$\hat{f}^j_n = \int_{-\infty}^{\infty} f(t)\psi^j_n(t)dt \tag{1.12}$$

The choice of the wavelet basis determines the nature of the information that can be extracted from the function. Many types of wavelets have been defined (Harr, Dauchebies, Meyer, Mexican hat, ecc.). For example, Fournier (2002) reformulated the atmospheric energy equations for any orthogonal wavelet, using the *coiflet* wavelet from Daubechies (1992). In his paper, the total energy is defined as:

$$\overline{K} = \sum_{j=0}^{\infty} \sum_{n=0}^{\infty} K_{j,n}$$

where $K_{j,n} = \frac{1}{2}(\hat{\mathbf{u}}^j_n \cdot \hat{\mathbf{u}}^j_n)$ is the contribution to the kinetic energy from distinct scales (j) and time locations (n). Its evolution is defined at each scale and location, schematically, by:

$$\frac{\partial K_{j,n}}{\partial t} = MK_{j,n} + C_{j,n} + D_{j,n} + TK_{j,n} + \sum\sum BK_{j,n} \tag{1.13}$$

Where $MK_{j,n}$ is the transfer to scale j at location n from the mean flow; $C_{j,n}$ and $D_{j,n}$ are the conversion from potential energy and dissipation, and $TK_{j,n}$ are the transferences to scale j and location n from other scales and locations. The eddy interactions do not create or destroy energy, so when summed up over all locations and scales, they are zero. In this formulation, some of the interaction terms were collected to form boundary transports that vanish when integrating over a closed domain, forming the $BK_{j,n}$ term. Again, we can see a correspondence of the energetic terms in the wavelet space with the terms in the Reynolds and the Fourier decompositions, except now the physical processes are resolved in both space (j) and time (n).

1.4.3 Multi Window Transform

As we already noticed, the choice of the basis is important in any spectral decomposition. Another wavelet-based method was developed by Liang (2002), the Multi Window Transform (in short, MWT) taking into account which characteristics should have the basis to ensure the suitability of the transform for energetic studies. In the MWT, the basis must meet some requirements: it must be orthonormal (and if not, it has to be orthonormalised), maximum around the origin and vanish far from the origin. The basis he chose was based on $\beta - splines$, symmetrical functions piecewise defined by polynomials that were normalized. With the use of the MWT, he developed the method for localized energy analysis that we used here, the MS-EVA. It was thought as a generalization for the mean-eddy decomposition and the original EVA of Pinardi and Robinson (1986). MWT provides the foundation of an orthonormal decomposition in scale windows satisfying the properties needed to perform an energy and vorticity analysis, particularly: orthogonality, localization and multi-scale representation.

MWT theory states that, being $\{\phi_n^j(t)\}$ an orthonormal basis, for any square integrable function $p(t)$, there exists a scaling transform:

$$\hat{p}_n^j = \int_0^\varrho p(t)\phi_n^{\varrho,j}(t)dt \tag{1.14}$$

for any scale level j and location $n = 0, 1, 2, ..., 2^{j_2}$. With this decomposition, given the window bounds, any function $p(t)$ can be projected on each window obtaining the respective synthesis or reconstructions. For example, for a three scale decomposition, the window bounds would be j_0, j_1 and j_2, each scale would be indicated with the superindex $S = 0, 1, 2$, and referred as the large scale, the mesoscale and sub-meso scale synthesis or reconstructions, respectively. The synthesis of each window is given by:

$$p_n^{\sim S}(t) = \sum \hat{p}_n^{\sim S}\phi_n^{\varrho,j_2}(t) \tag{1.15}$$

and the multi scale window transform is:

$$\hat{p}_n^{\sim S} = \int_0^\varrho p_n^{\sim S}(t)\phi_n^{j_2}(t)dt \tag{1.16}$$

where $\varrho = 1, 2$ indicates correspond to periodic and symmetric extension schemes in Liang and Anderson (2007).

The MWT can be applied to the Primitive Equations, and energy equations are derived for each scale. The kinetic energy at each scale S is thus defined as:

$$K_n^S = \frac{1}{2}\left(v_n^{\sim S} \cdot v_n^{\sim S}\right) \tag{1.17}$$

and the its evolution in each window S for each location n (for simplicity, we will skip the subindex) is written in schematic way as:

$$\frac{\partial K^S}{\partial t} = \Delta_h Q^S_K + \Delta_v Q^S_K + \Delta_h Q^S_P + \Delta_v Q^S_P + b^S + F^S_{K,h} + F^S_{K,v} + T^S_{K,h} + T^S_{K,v} \tag{1.18}$$

Where Q terms implicate transport of energy due to horizontal and vertical advection of the flow at each scale ($\Delta_h Q^S_K$ and $\Delta_v Q^S_K$, respectively) and pressure work ($\Delta_h Q^S P$ and $\Delta_v Q^S_P$); b^S represents the conversion from APE to KE, and F^S is the dissipation. The T_K terms are the transferences of kinetic energy among the scales due to nonlinear interactions.

The advantage of wavelet over Fourier formulation is in the physical interpretation. With Fourier, interaction over scales can be identified, and this was an advantage with respect to Reynolds formulation. But wavelets provide also information about the scales and locations. Also, they act like "microscope", adapting their resolution to the scale, while with Fourier the resolution is lower in lowest scale levels.

The fact that wavelets retain time-frequency localization make them suitable to study features of the signal locally, with details related with their scale, as opposed to Fourier. This property is especially useful for signals that are non stationary, have transient components or features at different scales.

Because the wavelet coefficients combine information about both the signal and the wavelet, the choice of the transform and the wavelet is important and depends on the information we want to extract from the signal. At this respect, MWT has been specially thought to fulfill the needs of EVA analysis. A limitation is that the selection of the window bounds is subjective, based in interpretation of the flow for each particular case.

1.5 Other methods

Besides the classical Reynolds decomposition, there are other statistical methods that can be applied to decompose the flow. Recently, the growing amount of data generated has lead to the development of some data driven methods that can extract meaningful information from the datasets. Among these methods there are some that take a set of data and numerically compute a set of *modes*, or characteristic features. Of course, the meaning of these modes depend on the particular decomposition used. But the idea is that modes can identify features enlightening the underlying physics.

The most common modal decomposition in fluid dynamics is the Proper Orthogonal Decomposition (POD) (Berkooz et al., 1993), a statistical technique that identifies a set of orthogonal modes that best reconstruct the dataset. POD is also known as principal component analysis, Karhunen-Loève decomposition, or empirical orthogonal Functions, depending on the field of study. The base of all of them is to compute the Singular Value Decomposition of the dataset. Since the basis are fixed (they are obtained from the data, but do not change), POD may not be able to represent evolving processes generated by nonlinear dynamics. Moreover, these methods are global in the sense that they consider only the mean and variance or covariance of the data, but lack the ability to give local representation for the processes.

Another method is the Dynamical Mode Decomposition (Schmid, 2010). The modes extracted contain information about the frequencies of oscillation of the data, but also about growth rates, and spatial structures for each mode. This makes the method appropriate for the analysis of nonlinear evolving fluid flows. A generalization of these methods has been recently formulated for the study of energy transferences in flows with uncertainty (Sapsis and Lermusiaux, 2009; Sapsis et al., 2013). They decompose each flow field into the statistical mean and an set of dynamical orthogonal modes. Using this decomposition, and some additional conditions, they reformulated the system formed by the stochastic Navier-Stokes equations to a lower order dynamical model for the coherent structures. This model is further adjusted to account for the neglected effects of small-scale turbulence via stochastic terms. In this way, they obtain a division between a mean, deterministic, part of the flow and a stochastic part, for which the characteristics modes are found. With the base of the Dynamical Mode Decomposition, they derived expressions for the stochastic energy transferences between the mean flow and the principal dynamical orthogonal modes, and also for the exchanges between the modes.

1.6 Conclusion

In this chapter we briefly summarized the main methods of scale decomposition used in energy studies.

The first method considered is the classical Reynolds decomposition. Energy studies based in Reynolds decomposition have undoubtedly contribute to the knowledge we have now. It is especially useful for stationary, homogeneous flows. Nevertheless, it presents some disadvantages. One is how to compute the mean (e.g. time, spatial, ensemble mean). Another is that any average results in a loss of information. In particular, no information is given about the interaction between separate scales, which is clue to understand how the energy is transferred between the large scales of the forcing to the dissipation scales. A local formulation of the energy equations (EVA) was developed in order to overcome the problem of averaging, but it misses the multi-scale approach.

Another method used in energy studies is the Fourier transform. With Fourier, the interpretation of the energy cascade is straightforward since it gives a general picture of how energy flows among scales. However, the use of trigonometric functions as basis influences the results. It is especially useful for regular, periodic flows, but this may not be the general case. Moreover, the oscillating character of the basis causes the delocalization of the signal.

Wavelets retain information about the spatial structure of the flow. As in the Fourier case, the transference between scales can be identified, but wavelets also represent particular locations of the interacting scales, within a resolution corresponding to the scale. An advantage is the physical interpretation of the energetics. When looking to Fourier space, one see cascades of energy being transferred from one wavenumber to another. However, the relation of these cascades in the physical space is not straightforward. With wavelets, one can face both sides of the problem, frequency and spatial domain. The choice of the wavelet basis is again a critical issue. At this respect, MS-EVA was formulated with a wavelet based approach, putting especial attention in the selection of the basis. The properties of the MS-EVA basis (as locality and orthogonality) provide a coherent physical framework for the energy formulation.

There are other methods for decomposition of the flow in modes depending on the data variance that are not addressed in this study.

Since real oceanic flows are non stationary, heterogeneous flows, the methodology that we will use need to combine locality and a multi scale representation of the flow. Among the methods reviewed, MS-EVA fit both conditions.

Chapter 2

Understanding instability and energy using MS-EVA: a analytical problem

2.1 Introduction

In this chapter we will use a classical linear stability problem to validate the MS-EVA implementations. For complete derivation of the problem mentioned here the reader is encouraged to consult Pedlosky (1987). In order to elucidate how a flow may become unstable, a series of assumptions are made, starting with the choice of a suitable model of the flow's behavior that simplifies the problem. If one assumes that the fluctuations which initially take place are small compared to a time-independent basic state, the model can be linearized and the resulting equations become simpler. We then consider modal solutions to the linear equations. In linear stability theory, the problem is reduced in order to determine in which conditions a small wave-like disturbance will evolve in time (growing or decaying), given a certain basic flow, which resembles more or less the state of flows found in nature.

Even though simple, the solutions are still useful to understand the basic processes underlying the instabilities, of course in the limits of the method: since the perturbation is ensured to be small, it is only valid at the beginning of the growing process; also, the definition of a basic flow consistent with the process is difficult.

The linear method has been extensively used in the past to study instabilities in linear zonal flows Charney (1947); Eady (1949); Kuo (1952); Phillips (1956), nonlinear flows Pedlosky (1987, Chapter 7).

Hydrodynamic instabilities are often classified into different categories depending on the primary mechanism from which the instability evolves. We will focus on barotropic and baroclinic instabilities due to their prevalence in the mesoscale of the world's oceans. Barotropic instability is a mechanism through which perturbations extract energy from the kinetic energy associated with horizontal shear of the mean flow, while baroclinic instabilities extract energy from the available potential energy asssociated to horizontal density gradients of the fluid.

Eady and Charney have been credited as giving the first quantifiable models of baroclinic instability. This mechanism of instability is prevalent in mid-latitudes and is responsible for weather patterns in the atmosphere and eddies in the oceans. Frontal flows exhibit the steepest slopes of density interfaces, and are therefore subject to the baroclinic instability mechanism. Frontal instabilities of western boundary currents trigger mesoscale eddies that produce swift flow also in the abyssal ocean (benthic storms, Rowe and Menzies (1968)).

For baroclinic instability to occur the system requires stratification and strong rotation. Baroclinic instability is classified by perturbations extracting available potential energy (APE) from the background flow that is typically in thermal wind balance.

The source of baroclinic instability is a depth variation of the horizontal flow in a stratified fluid, associated with tilted density interfaces. Disturbances in such flow lead to fluid stretching and squeezing at different locations of the disturbance, generating self enforced patterns of relative vorticity and disturbances growth in time. Perturbations of a wavelength of about 4 times the internal radius of deformation have the greatest initial growth rate (Vallis, 2006).

In this chapter we make use of the Eady problem to validate the MSEVA implementation, by contrasting the results with the more classical Reynolds decomposition. The validation will help to understand how MSEVA can be used in interpreting basic oceanic and atmospheric processes, before moving to the more complex real cases.

2.2 A brief introduction to MS-EVA

The MS-EVA is a new methodology thought for the investigation of multiscale processes that are non stationary and heterogeneous in space. The basic idea is to apply the Multi Window Transform introduced in Chapter 1 to the Primitive Equations in order to derivate the energy equations on each defined scale. The full development of the method can be found in Liang and Robinson (2005, 2007). Here a brief description of MS-EVA is given in a symbolic form, in order to facilitate the understanding of the results presented along the thesis. A more detailed description of how the energy equations are obtained at each scale and the link with the traditional mean-deviation decomposition is given in the Appendix A.

With MS-EVA, the processes are presented on scale windows. The first step in the implementation is hence to determine the scale windows for the decomposition. The limits of the windows are chosen depending on the characteristic scales of the studied processes, and by looking at the energy spectra. The MWT gives two outputs, the transform coefficients and the reconstructed fields. These outputs are used to compute the terms in the energy equations at each scale. For a three scale decomposition the scales are indicated with the superindex $S = 0, 1, 2$, or alternative with the letters L, M, S, standing for *large scale* and *mesoscale* and *sub-mesoscale*.

Schematically, the tendency of KE and APE on each window (S) and at time step (n) are governed by:

$$\delta_t K_n^S = \Delta Q_{K_n^S} + T_{K_n^S} + \Delta Q_{P_n^S} - b_n^S + F_n^S \tag{2.1a}$$

$$\delta_t A_n^S = \Delta Q_{A_n^S} + T_{A_n^S} + TS_{A_n^S} + b_n^S + F_n^S \tag{2.1b}$$

In the equations, the ΔQ terms represent the transport processes on the specific window; T terms are the transferences between scales, including the generation of APE due to the vertical shear of the mean density profile (TS); b terms are the buoyancy term indicating the conversion between APE and KE, and the F terms represent the dissipation by friction. Transport, transferences and friction terms can be further decomposed into their contribution in the horizontal and vertical directions (in the case, it is indicated by h or z subindexes).

Furthermore, the method provides a criterion for the identification of instabilities (Liang and Robinson, 2005), understood as the transferences ocurring from the larger scales to smaller scales. With this purpose, two indicators are defined: one taking into account the APE transferences to smaller scales (identified as BC), and another for the KE transferences (BT). For example, in a two scale decomposition, the indicators are the transference terms from the large scale ($S = 0$) to the mesoscale ($S = 1$):

$$BC = T_{A_n^1}^{0\to 1} + TS_{A_n^1}^{0\to 1} \tag{2.2a}$$

$$BT = T_{K_n^1}^{0\to 1} \tag{2.2b}$$

When these indicators are positive, the flow is locally unstable. Depending on the sign of the indicators, we identify the instabilities as purely baroclinic (only BC is positive), purely barotropic (only BT is positive) or mixed (both BC and BT are positive).

The energy relations between scales can be illustrated with an energy diagram as the one in Figure 2.1.

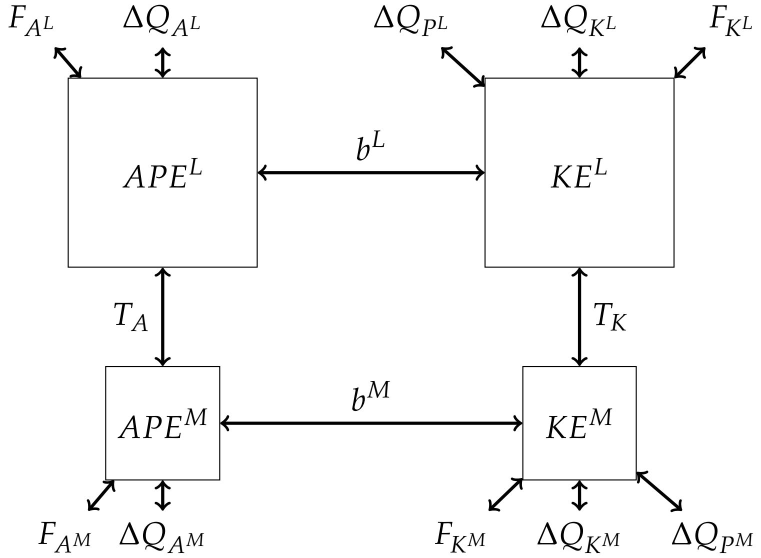

Figure 2.1: Diagram of energy and energy fluxes for a two scale decomposition. APE is Available Potential Energy, KE is the Kinetic Energy. Superscripts indicate Large scale (L) and Mesoscale (M) respectively. ΔQ_K and ΔQ_A are transports of APE and KE. ΔQ_P is the pressure work. F_A and F_K are the losses by friction. Buoyancy conversion is represented by b and the transferences between the two scales scales are T_A and T_K. After Liang and Robinson (2009).

2.3 Energy analysis

2.3.1 The Eady problem: review of the theory

Baroclinic instabilities are the dominant mechanisms for the growth of storms in mid latitudes, and mesoscale oceanic eddies. Eady (1949) formulated a simple model for baroclinic instability. In spite of the simplicity, the Eady model catches the main processes driving the early development of baroclinic instabilities. We will use the analytic solutions of the Eady model in order to validate the MS-EVA. This will help us to understand how MS-EVA represents baroclinic instabilities.

Consider a system characterized by the primitive equations under Boussinesq, hydrostatic and f-plane approximation, with the x, y, z axes indicating the zonal, meridional and vertical directions. Friction is neglected, since the energy of the perturbations is considered to be much larger than the loss by friction. Diffusion is also neglected. The governing equations are:

$$\frac{\partial u}{\partial t} = -u\frac{\partial u}{\partial x} - v\frac{\partial u}{\partial y} - w\frac{\partial u}{\partial z} + fv - \frac{1}{\rho_0}\frac{\partial P}{\partial x} \tag{2.3a}$$

$$\frac{\partial v}{\partial t} = -u\frac{\partial v}{\partial x} - v\frac{\partial v}{\partial y} - w\frac{\partial v}{\partial z} - fu - \frac{1}{\rho_0}\frac{\partial P}{\partial y} \tag{2.3b}$$

$$0 = \frac{\partial u}{\partial x} + \frac{\partial v}{\partial y} + \frac{\partial w}{\partial z} \tag{2.3c}$$

$$\frac{\partial P}{\partial z} = -\rho g \tag{2.3d}$$

$$\frac{\partial \rho}{\partial t} = -u\frac{\partial \rho}{\partial x} - v\frac{\partial \rho}{\partial y} - w\frac{\partial \rho}{\partial z} \tag{2.3e}$$

The flow is described by a background state, on which a small perturbation is superimposed. The peculiarities of the basic flow determine the problem. In our case, we consider a steady state baroclinic flow, with uniform motion at each layer, and a constant vertical shear:

$$\bar{u} = \bar{u}(z), \text{ and } \frac{\partial \bar{u}}{\partial z} = \Lambda = \text{constant} \tag{2.4}$$

The basic density profile is a linear function of y and z:

$$\bar{\rho} = B_y y + B_z z \tag{2.5}$$

At any point, the flow is stably stratified and density increases in the meridional direction. By thermal wind relation, $B_y = \rho_0 f \Lambda / g$, while the static stability B_z is constant. The flow fields can be decomposed into the basic state (indicated by an overbar) and the perturbation (indicated by primes):

$$\begin{aligned} u(x,y,z,t) &= \bar{u}(z) + u'(x,y,z,t) \\ v(x,y,z,t) &= v'(x,y,z,t) \\ w(x,y,z,t) &= w'(x,y,z,t) \\ \rho(x,y,z,t) &= \bar{\rho}(y,z) + \rho'(x,y,z,t) \end{aligned} \tag{2.6}$$

and substituted into the governing equations (2.3). In the Eady problem, only small perturbations are considered. This implies that we can neglect quadratic terms. The corresponding linearized equations describing the evolution of the perturbation are:

$$\frac{\partial u'}{\partial t} = -\bar{u}\frac{\partial u'}{\partial x} - v'\frac{\partial \bar{u}}{\partial y} - w'\frac{\partial \bar{u}}{\partial z} + fv' - \frac{1}{\rho_0}\frac{\partial P'}{\partial x} \tag{2.7a}$$

$$\frac{\partial v'}{\partial t} = -\bar{u}\frac{\partial v'}{\partial x} - v'\frac{\partial \bar{v}}{\partial y} - w'\frac{\partial \bar{v}}{\partial z} - fu' - \frac{1}{\rho_0}\frac{\partial P'}{\partial y} \tag{2.7b}$$

$$0 = \frac{\partial u'}{\partial x} + \frac{\partial v'}{\partial y} + \frac{\partial w'}{\partial z} \tag{2.7c}$$

$$\frac{\partial P'}{\partial z} = -\rho' g \tag{2.7d}$$

$$\frac{\partial \rho'}{\partial t} = -\bar{u}\frac{\partial \rho'}{\partial x} - v'\frac{\partial \bar{\rho}}{\partial y} - w'\frac{\partial \bar{\rho}}{\partial z} \tag{2.7e}$$

Eady reduced this system to one single partial differential equation involving w as the only dependent variable. The problem was still too difficult to be solved, but it is possible to seek for simple types of solutions that may mimic what is seen in nature. Consider the existence of a solution with a wave-like form:

$$\begin{bmatrix} u' \\ v' \\ w' \\ \rho' \\ P' \end{bmatrix} = Re(\begin{bmatrix} \tilde{u}(z) \\ \tilde{v}(z) \\ \tilde{w}(z) \\ \tilde{\rho}(z) \\ \tilde{P}(z) \end{bmatrix} e^{i(kx+ly-\omega t)}) \tag{2.8}$$

If it exists, the perturbation fields can be described by an amplitude function times and exponential, where k and l are the horizontal wave numbers, while ω is the wave frequency. When these solutions are substituted into (2.7), the problem is reduced to an ordinary differential equation for the vertical structure of the vertical velocity:

$$X(X^2-1)\frac{\partial^2 \tilde{w}}{\partial X^2} + 2(1 - i\sigma X)\frac{\partial \tilde{w}}{\partial X} + (R_\sigma X + 2i\sigma)\tilde{w} = 0 \tag{2.9}$$

In obtaining this equation, a change of the vertical coordinate has been done:

$$X \equiv X(z) = \frac{\bar{u}(z)k - \omega}{f} \tag{2.10}$$

and other terms are defined as:

$$\begin{aligned} \sigma &\equiv \frac{l}{k}\,, \\ R_\sigma &\equiv (1+\sigma^2)Ri, \end{aligned} \tag{2.11}$$

where Ri is the Richardson number of the unperturbed flow:

$$Ri = -\frac{g/\rho_0 \cdot \partial\bar{\rho}/\partial z}{(\partial u/\partial z)^2} = -\frac{gB_z}{\rho_o\Lambda^2} \tag{2.12}$$

A further simplification is done by defining:

$$W \equiv W(z) = \left(\frac{1-X}{1+X}\right)^{-\frac{i\sigma}{2}} \tilde{w}(z) \tag{2.13}$$

Finally, the ordinary differential equation to solve is:

$$\frac{\partial^2 W}{\partial X^2} - \frac{2}{X}\frac{\partial W}{\partial X} - R_\sigma W = 0 \tag{2.14}$$

This equation has a general solution of the form:

$$W = a_1 W_1 + a_2 W_2 \tag{2.15}$$

where a_1,a_2 are constants, and W_1, W_2 have the form:

$$\begin{aligned} W_1 &= e^{\sqrt{R_\sigma}X}(1-\sqrt{R_\sigma}X) \\ W_2 &= e^{-\sqrt{R_\sigma}X}(1+\sqrt{R_\sigma}X) \end{aligned} \tag{2.16}$$

Consider a system that is infinite horizontally, and bounded vertically. The vertical velocity must vanish at the walls. Thus, the boundary conditions are:

$$W = 0, \quad \text{at } X = X_{top}, X_{bottom} \tag{2.17}$$

The constants a_1, a_2 are related:

$$\frac{a_2}{a_1} = -e^{2\sqrt{R_\sigma}X_{top}}\left(\frac{1-\sqrt{R_\sigma}X_{top}}{1+\sqrt{R_\sigma}X_{top}}\right) = -e^{2\sqrt{R_\sigma}X_{bottom}}\left(\frac{1-\sqrt{R_\sigma}X_{bottom}}{1+\sqrt{R_\sigma}X_{bottom}}\right) \tag{2.18}$$

By writing:

$$\begin{aligned}(\sqrt{R_\sigma}X_{bottom} - \sqrt{R_\sigma}X_{top}) &= 2\alpha \\ (\sqrt{R_\sigma}X_{bottom} + \sqrt{R_\sigma}X_{top}) &= -2i\beta\end{aligned} \tag{2.19}$$

we have:

$$\beta^2 = (\alpha - \tanh\alpha)(\coth\alpha - \alpha) \tag{2.20}$$

that is the condition to satisfy. α (the scaled wavenumber) is defined as:

$$\alpha = \frac{\sqrt{R_\sigma}}{2f}(-\Lambda)kH = \frac{\sqrt{R_\sigma}}{2f}(u_{bottom} - u_{top})k \tag{2.21}$$

α is real, but β can be either real or imaginary. Unstable solutions occur only when β is real (so $\beta^2 > 0$), which occurs for $|\alpha| < \alpha_{critical} \approx 1.1997$.

The wavenumber cutoff is function of $\alpha_{critical}$:

$$|k_{critical}| < \frac{2f}{\sqrt{R_\sigma}}\Lambda H \cdot \alpha_{critical} \tag{2.22}$$

Finally, the problem defined by (2.14) and (2.17) has nontrivial solutions if, and only if:

$$\begin{aligned}\omega_0 &= \frac{k}{2}(u_{top} + u_{bottom}), \\ \omega_1 &= \beta\frac{f}{\sqrt{R_\sigma}}\end{aligned} \tag{2.23}$$

The first equation in (2.23) indicates that the perturbation moves with the basic flow. The second determines the growth rate.

The amplitude function $\tilde{w}(z)$ can be obtained reverting (2.13) as:

$$\tilde{w}(z) = \left(\frac{1-X}{1+X}\right)^{\frac{i\sigma}{2}} W(z) \tag{2.24}$$

The other fields are all related to $\tilde{w}(z)$ and can be obtained from:

$$\tilde{u}(z) = \frac{-\Lambda/f}{1+\sigma^2}\left[-\frac{\sigma}{X}\frac{\partial\tilde{w}}{\partial X} - i\left(\sigma^2\frac{\tilde{w}}{X} + \frac{\partial\tilde{w}}{\partial X}\right)\right] \tag{2.25}$$

$$\tilde{v}(z) = \frac{-\Lambda/f}{1+\sigma^2}\left[\frac{1}{X}\frac{\partial\tilde{w}}{\partial X} + i\sigma\left(\frac{\tilde{w}}{X} - \frac{\partial\tilde{w}}{\partial X}\right)\right] \tag{2.26}$$

$$\tilde{P}(z) = \frac{-\Lambda/f}{1+\sigma^2}\cdot\frac{f\rho_0}{ik}\left[\left(\frac{1}{X}\frac{\partial\tilde{w}}{\partial X} + i\sigma\frac{\tilde{w}}{X}\right) + \left(\tilde{w} - X\frac{\partial\tilde{w}}{\partial X}\right)\right] \tag{2.27}$$

$$\tilde{\rho}(z) = \frac{(-\Lambda/f)^2}{1+\sigma^2} \cdot \frac{f\rho_0}{g} \cdot \frac{i}{X} \cdot \left[\left(\frac{1}{X}\frac{\partial \tilde{w}}{\partial X} + R_\sigma \tilde{w} \right) + i\sigma \left(\frac{\tilde{w}}{X} - \frac{\partial \tilde{w}}{\partial X} \right) \right] \tag{2.28}$$

The growth rate is maximum when the meridional wavenumber $l = 0$. Thus, by considering $\sigma = 0$, the equations simplify to:

$$\tilde{w}(z) = W(z) \tag{2.29}$$

$$\tilde{u}(z) = -\Lambda/f \left[-i\frac{\partial \tilde{w}}{\partial X} \right] \tag{2.30}$$

$$\tilde{v}(z) = -\Lambda/f \left[\frac{1}{X}\frac{\partial \tilde{w}}{\partial X} \right] \tag{2.31}$$

$$\tilde{P}(z) = -\frac{\Lambda\rho_0}{ik} \left[\left(\frac{1}{X}\frac{\partial \tilde{w}}{\partial X} \right) + \left(\tilde{w} - X\frac{\partial \tilde{w}}{\partial X} \right) \right] \tag{2.32}$$

$$\tilde{\rho}(z) = \frac{\Lambda^2\rho_0}{fg} \cdot \frac{i}{X} \cdot \left[\left(\frac{1}{X}\frac{\partial \tilde{w}}{\partial X} + \tilde{w}Ri \right) \right] \tag{2.33}$$

Substituting these amplitude functions back into the wave solutions (2.8), one obtains the perturbation fields. We will use these analytical solutions evaluated at different times to create a dataset to which we will apply the energy analysis.

2.3.2 Dataset preparation

Once stated the problem, we need to create the dataset that we will use for the energy analysis. Because the first objective is to validate the MS-EVA, we have chosen the same configuration that Liang and Robinson (2005, 2007), in order to facilitate the comparison. Figure 2.2 shows the relation between wavenumber and growth rate. For wave numbers above the wavenumber cutoff there is no growing perturbation. Below this limit we have positive growth rates. The results shown here correspond to the unstable case, where $k = 1 \times 10^{-5}\, m^{-1}$.

The configuration parameters are shown in table 2.1. The values are typical for mid-ocean. Some relevant derived quantities are also shown.

The solution is evaluated at different times to form a series of $2^{10} = 1024$ data, spanning for a time long enough to complete two cycles (97 days for the unstable mode).

The constant $a_1 = 2 \times 10^{-7}$ in order to keep the perturbation small enough over the whole period. The data are mapped in a C grid with a grid spacing of

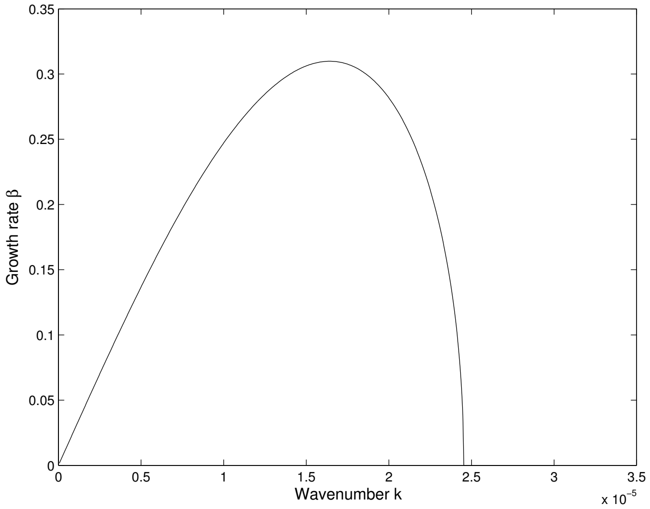

Figure 2.2: Growth rate versus wavenumber

Table 2.1: Experiment parameters

$\bar{u}_{top}$	=	$0.2\, m/s$	Velocity at the upper boundary
$\bar{u}_{bottom}$	=	$0.1\, m/s$	Velocity at the lower boundary
ρ_0	=	$1025\, kg/m^3$	Reference density
H	=	$1000\, m$	Depth
f_0	=	$1 \times 10^{-4}\, s^{-1}$	Coriolis frequency
B_z	=	$-1 \times 10^{-2}\, kg/m^4$	Vertical stability parameter
Λ	=	$1 \times 10^{-4}\, s^{-1}$	Velocity shear
B_y	=	$1.046 \times 10^{-6}\, kg/m^4$	Meridional density gradient
Ri	=	9.561×10^{-3}	Richardson number

20 km x 50 km x 10 m in the vertical. The horizontal domain is 1000 km x 1000 km.

The phases of the perturbation fields are shown in figure 2.3. At each level, the perturbation is seen as a series of ridges and troughs of similar absolute amplitude. The phase angle of the velocity and pressure fields tilt westward with depth, while the tilting of the density isolines is opposite. This is due to the advance of the upper level phase perturbation with respect to the lower level, which is a typical feature of baroclinic instabilities.

2.3.3 Evaluation of the energetics

We use the total Eady field (basic flow plus perturbation) to test the MS-EVA. The total fields are decomposed in scales with the MWT. The fields can be decomposed and reconstructed in three scales, called *large scale*, *meso scale* and

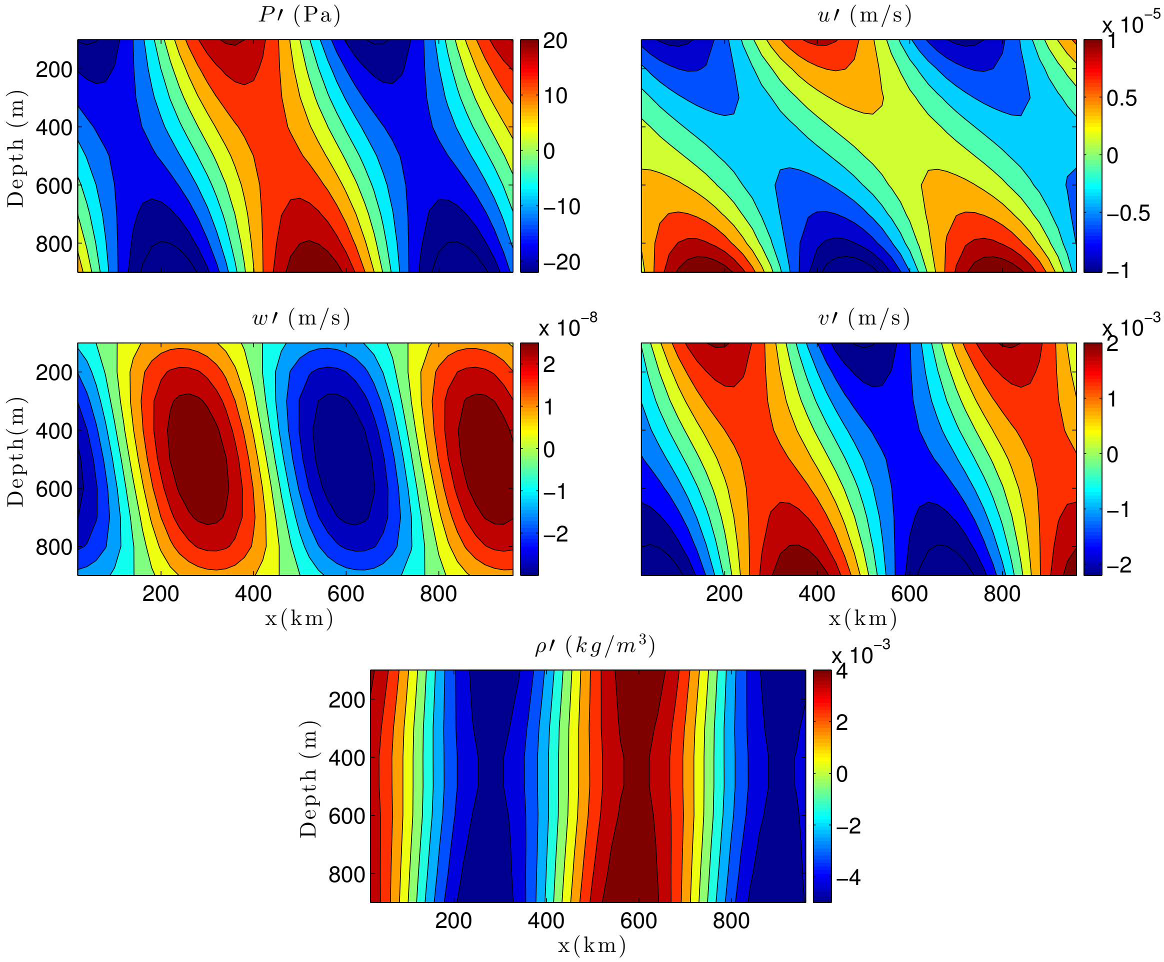

Figure 2.3: Phases of the pressure (a), zonal, vertical and meridional velocities (b,c,d) and density (e) perturbations. Snapshots of 10th day, at section at $y = 500km$.

submeso scale. The size of each window is determined by its limits, as illustrated in Figure 2.4. In particular, we perform a two scale decomposition (the window limits are set as $j_0 = 0, j_1 = j_2 = 10$, which is the maximum resolution of our series). A periodic extension is used for the boundaries. Under this conditions, the MS-EVA is a generalization of the classical Reynolds decomposition, and the time mean and perturbation fields correspond to the large scale and mesoscale reconstructions, respectively. This connection between the two formulations allows us to contrast the MS-EVA results with the energy fluxes computed for the analytical Eady solutions.

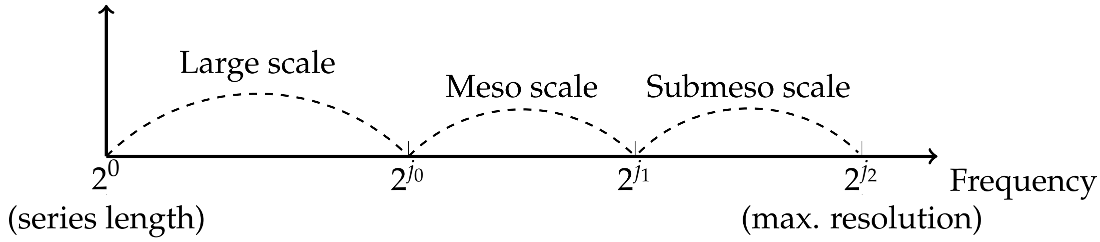

Figure 2.4: Schematics of scale window limits in the MWT.

The large and mesoscale reconstructions are shown in Figures 2.5 and 2.6. The large scale is equal to the time mean of the total flow computed with a mean-deviation decomposition where the average is taken over all the time period. The basic state is discernible in the sheared zonal velocity and the pressure field. Since we are interested in the APE evolution, we subtracted the mean density profile from the basic density flow. As a consequence, the large scale density is of the same order of magnitude as the perturbation density, and exhibits a wave-like pattern in the zonal direction. The vertical and meridional mean fields are equal to the time average of the perturbation, since the basic fields are zero. The mesoscale reconstructions contain the perturbation fields. The reconstructed fields are indeed equal to the panels showed in figure 2.3, confirming that the MWT with two scales is equivalent to the mean-deviation decomposition.

The energy terms are calculated for the reconstructed fields from the potential and kinetic energy equations in each scale as described in Appendix A. We focus the energy analysis on the mesoscale, that is where the perturbation lives. MS-EVA provides a time localized energy analysis, which allows to evaluate the time evolution of the decomposed energy. However, in order to be comparable with the mean eddy energy fluxes, the mesoscale energy terms have to be

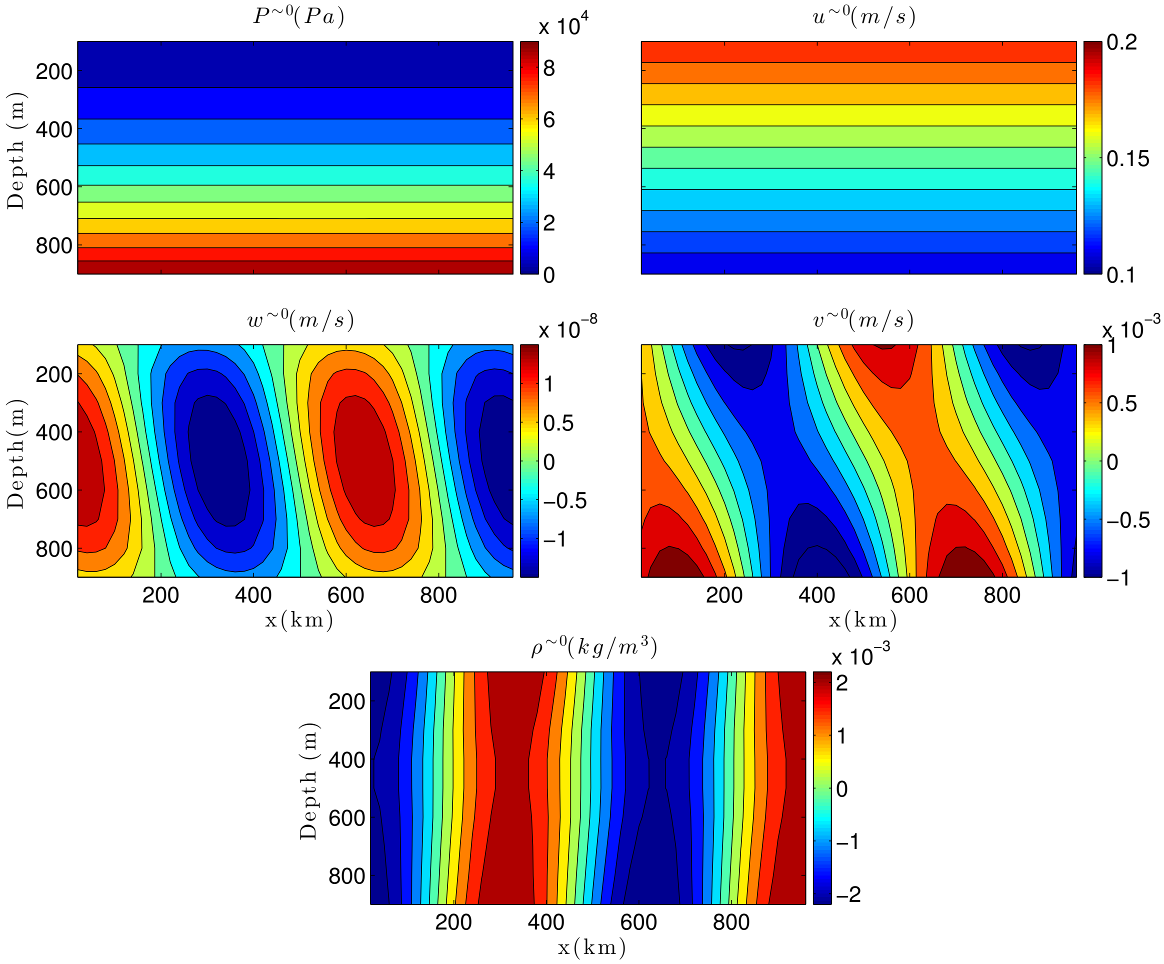

Figure 2.5: Phases of the pressure (a), zonal, vertical and meridional velocities (b,c,d) and density (e) large scale reconstructions. Sections at $y = 500km$.

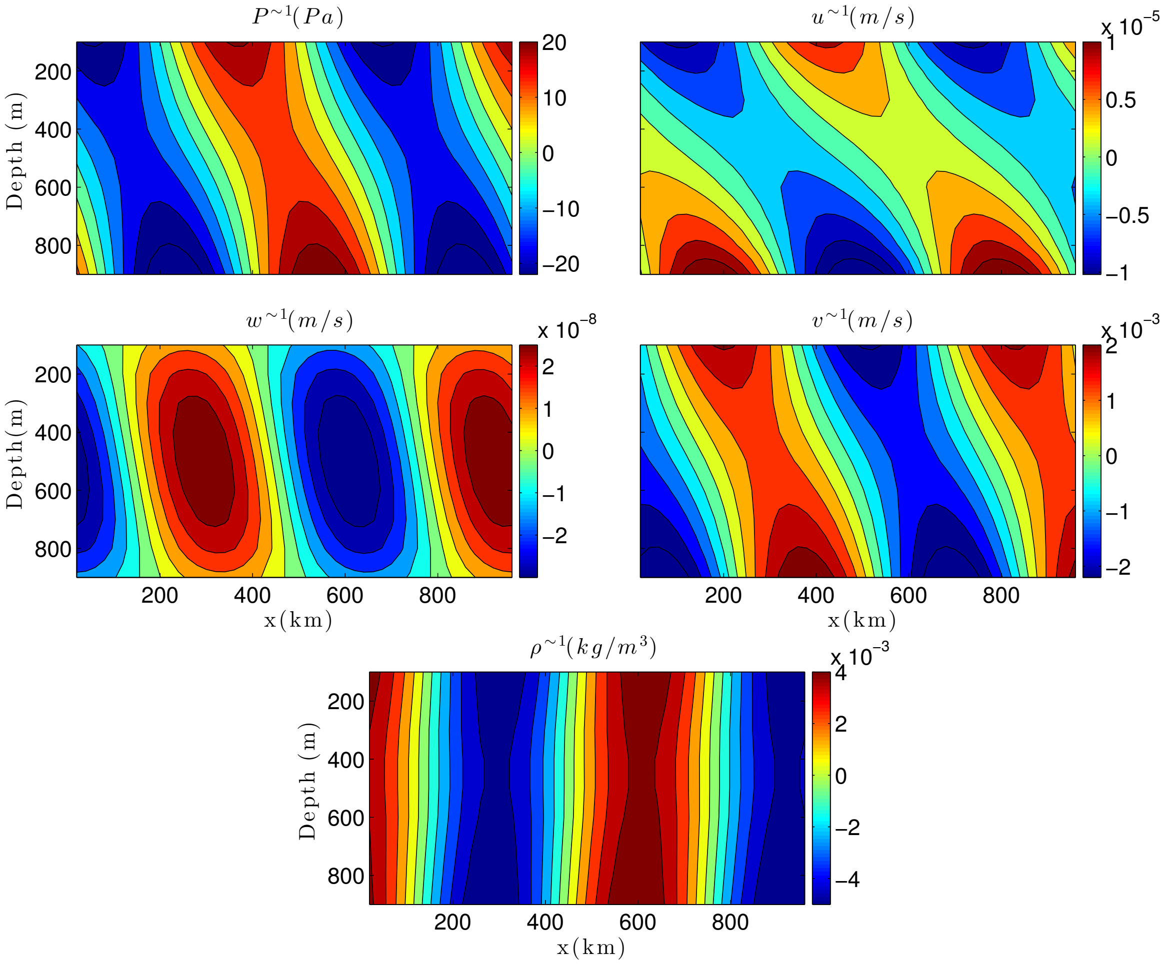

Figure 2.6: Phases of the pressure (a), zonal, vertical and meridional velocities (b,c,d) and density (e) mesoscale reconstructions. Snapshots of 10th day, at section at $y = 500km$.

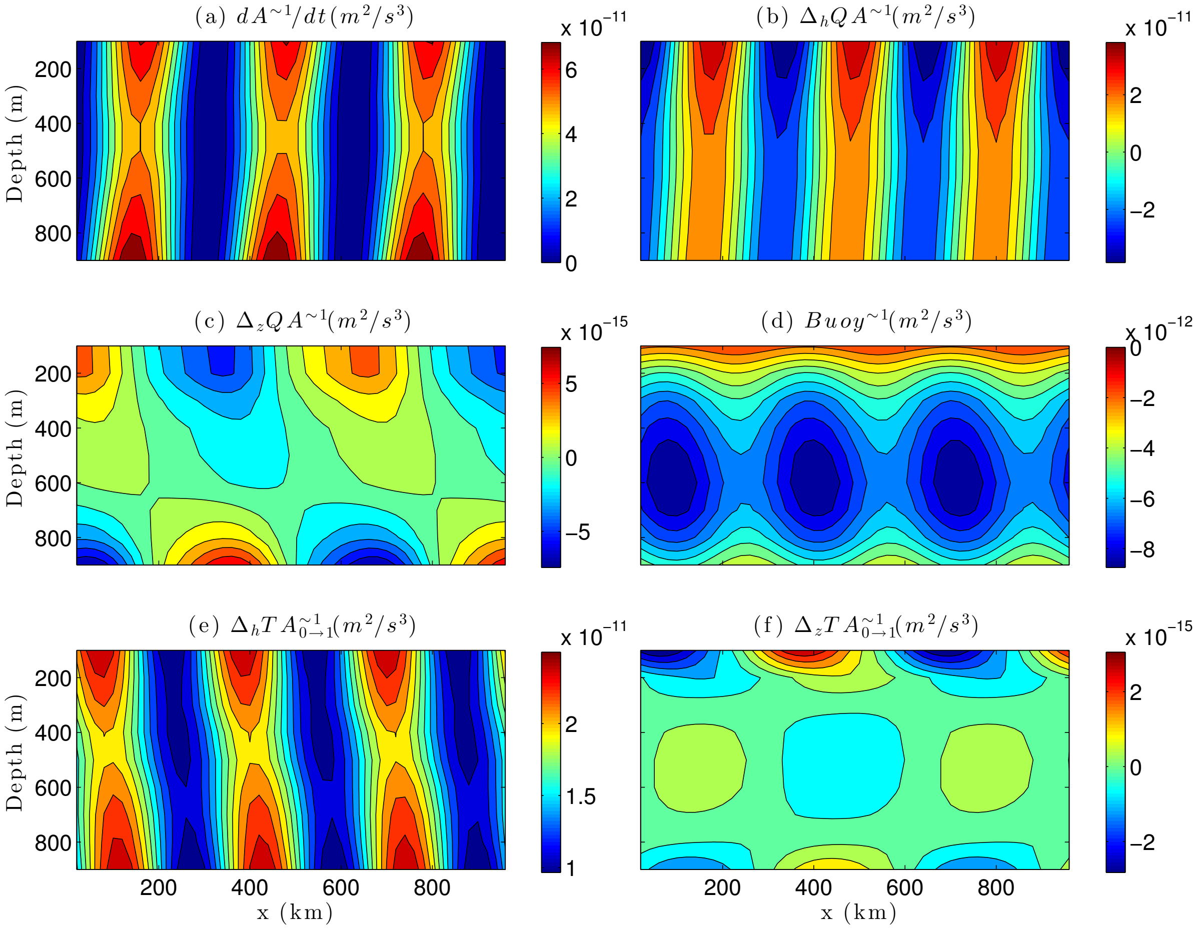

Figure 2.7: APE tendency (a), horizontal and vertical APE transport (b,c), buoyancy conversion (d), horizontal and vertical APE transfer from the large to the mesocale (e,f). Section at $y = 500km$.

integrated over all the time locations[1]. The panels showed in the following are hence the marginalized energy terms.

A careful look at the energy distribution helps us to identify the main processes involved in the perturbation evolution. Figure 2.7 shows the marginalized APE terms. We can see that the APE tendency is mainly due to the horizontal transport and transfer terms (panels b and e). The buoyancy conversion (panel d) is an order of magnitude smaller, but we highlight it here because it has a key role in generating kinetic energy. Vertical transport and transfers (panels c and f) are minor order terms. The horizontal transport is responsible of the pattern of the APE evolution. This term indicates how the energy flux is advected by the flow. Since both the basic flow and the perturbation are eastward, the transport occurs in the zonal direction. Since the transport averages to zero when integrating over the domain, meaning that it does not contribute

---

[1] By the marginalization property of the MWT in (Liang and Anderson, 2007).

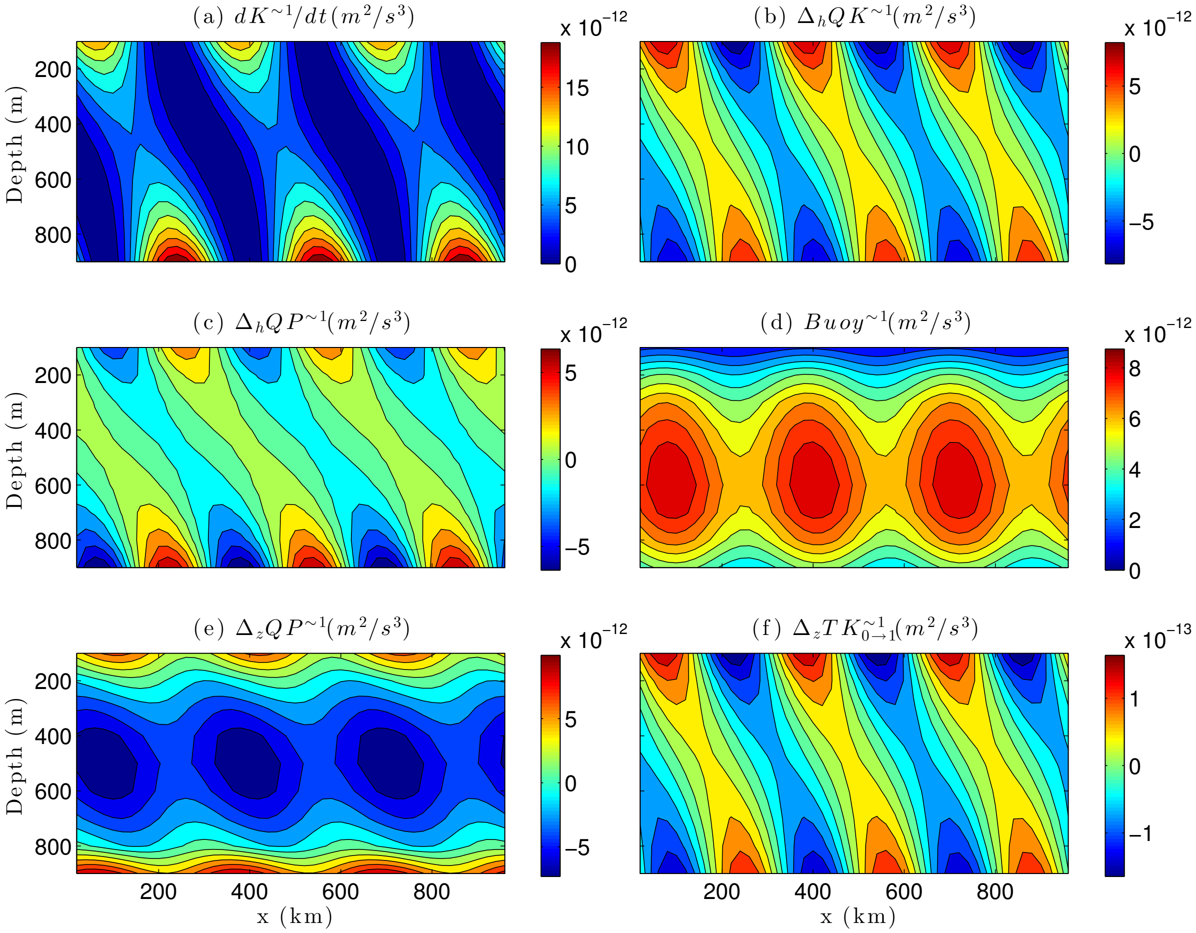

Figure 2.8: KE tendency (a), horizontal and vertical KE transport (b,c), buoyancy conversion (d), horizontal and vertical pressure work (e,f). Section at $y = 500km$.

to the total variation of APE, but acts just to redistribute the energy along the domain. The mesoscale APE increases in time (the positive rate of change of marginalized mesoscale APE) due to the transference of energy from the large scale. The marginalized APE large-to-mesoscale transference is indeed positive in all the domain. In the frictionless context that we are considering, the only sink of mesoscale APE is the buoyancy conversion. The mesoscale APE is transformed in mesoscale KE through the buoyancy conversion term. This conversion is maximum in the mid levels.

The marginalized mesoscale KE terms can be seen in figure 2.8. The distribution of KE is determined by the buoyancy conversion, horizontal transport and pressure work terms (figures b,c,d,e in the panel). The only source of mesoscale KE is the buoyancy conversion. The energy produced by conversion is exported to the boundaries by the vertical pressure work. As in the APE distribution, the horizontal transport redistributes the mesoscale KE over the domain, but averages to zero. The same can be said for the horizontal pressure work. In this case, the transference term is one order of magnitude smaller than the other terms, and averages to zero. This is because the Eady model produces a purely baroclinic instability. There are no KE transferences feeding the perturbation because there are no horizontal gradients of velocity. The perturbation grows only at the expense of the APE stored in the sloping isopycnals of the mean flow.

The described energy patterns were coherent with the mean eddy fluxes computed for the analytical solution (not showed). However, we had to marginalize the mesoscale energetics in order to make them comparable, loosing therefore the temporal information. The potentiality of using MS-EVA is to provide an energy analysis that is localized in both time and space. In the Eady case, the energy is growing in time, but the distribution does not change. One could arrive to the same conclusions by looking at any time location. This is not the case of realistic flows, normally varying in both dimensions. This experiment helped us to test the use of the methodology. In the next, we will run a set of progressively more realistic simulations in order to describe the different processes that we can find in the ocean using M-SEVA.

2.4 Conclusions

In this Chapter, we used the Eady problem to validate the methodology. The use of an analytical model is justified because it provides a well-known framework where the dynamics are reduced to a few physical processes and are well-known. The validation consisted in the interpretation of the dynamics reproduced by the analytical Eady model, and a comparison with an analysis based on a mean-deviation decomposition.

MSEVA was successfully validated with the use of the Eady model. The Eady problem reproduces the evolution of a perturbation on a background flow. In the case of an unstable flow, the perturbation grows due to baroclinic instabilities. Both the mean flow and the perturbation were well reproduced in the reconstructed large scale and meso scale fields, confirming the correspondence of the two scale MWT decomposition with the mean-deviation decomposition. The energy paths were investigated by looking at the meso scale energy evolution (where the perturbation lives). The mesoscale APE and KE energy terms showed that the perturbation grows due to the transference of large scale APE to mesoscale APE, the basic mechanism in baroclinic instabilities. Part of the APE is transformed to KE via buoyancy conversion. Transport term work to redistribute the energy horizontally, and vertically from the mid level, where is maximum, to the upper and lower boundaries. The large scale energy and the marginalized mesoscale energy distribution were contrasted with the mean and eddy energy paths obtained with a mean-deviation decomposition, and proved to be equivalent.

Chapter 3

Dynamics of an idealized upwelling

3.1 Introduction

Real ocean circulation is very complex. Any map of the surface circulation will reveal the presence of a multitude of structures: quasi-steady currents and gyres, different size rings, filaments, etc. This complexity is the consequence of many forces acting at the same time: tidal forcing, atmospheric pressure changes, evaporation and precipitation, or wind blowing in different directions, to name some. Since the dynamics of realistic simulations contains the effect of all these forces combined, in practice the study of the energetics may not be so straightforward. For this reason, first we perform the analysis on a simpler, idealized simulation, where we can study the energetics in a fully controlled system. This chapter hence is devoted to the study of the energetics of an idealized circulation.

One of the major sources of energy for the ocean is the wind (Huang, 2004). Wind stress supports the formation of quasi-steady currents and gyres (the so called wind-driven circulation). It generates surface waves and it is in general responsible for the circulation and mixing in the upper layer of the ocean.

The immediate effect of a wind stress applied to the surface is a water transport in the upper/Ekman layer. Once the water is put in motion by the wind, the Coriolis force deflects the field (to the right in the northern hemisphere, to the South in the southern hemisphere), so the averaged transport occurs in a direction perpendicular to the wind. The basic dynamics consist in a balance between the wind induced frictional force and Coriolis, and were first explained in the Ekman theory's (Ekman, 1905). The ocean motion forced by the wind implies a transference of kinetic energy from the atmosphere to the ocean. Furthermore, the existence of horizontal divergence (convergence) zones in the

Ekman layer generates vertical fluxes in order to satisfy the mass conservation. These vertical fluxes do work against the hydrostatic pressure field that lead to changes in the isopycnals. The change in the stratification is the means by which the kinetic energy of the atmosphere is converted into potential energy in the ocean.

In open water, the divergences in the Ekman drift occur because wind changes in space and time. The wind curl is hence the main factor to consider. However, divergences are created also in the presence of an obstacle, for example, in the vicinity of shoals, ridges and coasts. In this case, the relative direction of the wind with respect to the obstacle is the key factor. The offshore/onshore transport produced by a wind blowing parallel to a coast generates a vertical flux (or Ekman pumping) close to the coast. The process is called *coastal upwelling* or *downwelling*, depending on upward or downward movement.

Coastal upwellings are important because they affect the coastal circulation and the redistribution of physical, biological and chemical components (Brink, 1983). Furthermore, they are often associated with enhanced production (Cushing, 1971). The most important upwelling systems are located at the eastern coast of all the oceans, associated with the main gyres and with cold current systems (California, Peru, Canary and Benguela). Minor upwellings are detected all over the world, included our area of study, the Mediterranean (Bakun and Agostini, 2001).

In addition to the rising (sinking) of water at coast, the onshore (offshore) piling of water associated with the upwelling (downwelling) generates horizontal gradients of pressure that lead to the formation of geostrophic alongshore currents.

The dynamics of coastal upwelling systems are, however, more intricate. In fact, Brink (1983) evidenced the three-dimensional character of coastal upwellings. The upwelling structure depends on various factors as the shelf topography, the former stratification and the wind variability. It is characterized by the development of an Ekman (or mixing) layer where the wind exerts its transport, the existence of an upwelling front (a region of intensified gradients that can be identified with outcropping isopycnals), and the presence of structures as ekman centers and filaments. While these features may be evident in some idealized simulations, in the real world they are embedded in the interior flow regime, which dominates outside the ekman layer.

Here we study the simplest case, which is an uniform upwelling. Of course, we do not find this condition in the real world: wind very rarely is that homogeneous, and the coast changes direction, so the upwellings are intermittent. Moreover, there are other process that could be considered, such as the effect of the background flow, the excitation of inertial oscillations by the wind that may interact with the signal, or the solar radiation cycle that affects the mixing. Nevertheless, we consider this case as a first step in the approximation of the problem, and we focus on the response of the ocean to the onset of an upwelling favorable wind stress.

3.2 Experiment configuration

3.2.1 Model description

We use the Nucleus for European Modeling of the Ocean (NEMO; Madec and the NEMO team (2012)), which is a free-surface primitive equation ocean model. The governing equations of motion are:

$$\frac{\partial \mathbf{U_h}}{\partial t} = -\left[(\nabla \times \mathbf{U}) \times \mathbf{U} + \frac{1}{2}\nabla(\mathbf{U}^2)\right]_h - f\mathbf{k} \times \mathbf{U}_h - \frac{1}{\rho_0}\nabla_h p + \mathbf{D}^U + \mathbf{F}^U \tag{3.1a}$$

$$\nabla \cdot \mathbf{U} = 0 \tag{3.1b}$$

$$\frac{\partial p}{\partial z} = -\rho g \tag{3.1c}$$

$$\frac{\partial T}{\partial t} = -\nabla \cdot (T\mathbf{U}) + \mathbf{D}^T + \mathbf{F}^T \tag{3.1d}$$

$$\frac{\partial S}{\partial t} = -\nabla \cdot (S\mathbf{U}) + \mathbf{D}^T + \mathbf{F}^T \tag{3.1e}$$

$$\rho(T,S) = \rho(T,S,p) \tag{3.1f}$$

where ∇ is the derivative vector operator in the three-dimensional plane (or in the $(\mathbf{i},\mathbf{j})$ plane when the subscript h is indicated), t is time, g the gravitational acceleration constant, and f the Coriolis acceleration. The velocity vector is $\mathbf{U} = \mathbf{U}_h + w\mathbf{k}$, T is temperature, S is salinity, P is pressure, ρ is density and ρ_0 a reference density. **D** is the parametrization of small scale processes, where the superscripts U and T stand for velocity and tracers respectively. **F** represent the surface forcing (i.e, wind, heat and water fluxes).

In our ideal configuration, we use a linear equation of state: $\rho(T,S) = \rho_0(1-(\alpha T - \beta S))$, where $\alpha = 2 \times 10^{-4}\, kg/K\, m^3$ and $\beta = 7.7 \times 10^{-4}\, kg/m^3$

are the expansion coefficients for temperature and salinity, and the reference density is $\rho_0 = 1026\, kg/m^{-3}$.

The momentum equations are formulated in the vector invariant form, and an enstrophy and energy conserving scheme is used for the advection and vorticity terms. Because MS-EVA equations are formulated in a flux form, this can introduce errors in the energy computation. A second order centered advection scheme is applied for tracers. Lateral boundaries are closed and a free-slip and no heat and salt flux conditions are applied on them. The free surface is filtered, and the bottom friction is zero. The horizontal viscosity and diffusivity are neglected, while the vertical coefficients of viscosity and diffusivity are computed using the Mellor-Yamada level 2.5 turbulence closure scheme.

The domain is an f-plane at 35°N. The basin is 250 m deep, with the the eastern boundary representing the coast. The model is solved in a 256×256 Arakawa C grid with regular spacing. The horizontal resolution is 1 km. The computational domain is large enough to avoid the effect of the boundaries, yet we evaluate only a x-z section at the center of the domain. There are 50 z-coordinate levels, with a spacing varying from 5 m in surface layers to 30 m in the deeper ones. The model is run for 6 days, with a time resolution of 600 seconds.

Three cases are considered, corresponding with different bathymetries as shown in Table 3.1. The difference between V2 and V3 is the smoothness of the bathymetry. Differences are mainly in the upper 40 meters, where the bathymetry in V3 present a larger step compared to V2.

Table 3.1: Set of experiments performed

Experiment name	Topography
V1	Flat bottom
V2	Sloping edge
V3	Sloping edge with step

In all the experiments, the model is forced by a spatially uniform wind in the meridional direction. The wind stress is increased to 0.1 N/m^2 during the first two days of simulation, and remains constant over the whole run (Figure 3.1). No surface heat or water fluxes are applied. The simulations are started from rest, with homogeneous temperature (Figure 3.2) and constant salinity, corresponding to a stable stratification.

In order to ensure that we have a controlled run, we compared the model output with the exact analytical solution for an upwelling described by Choboter

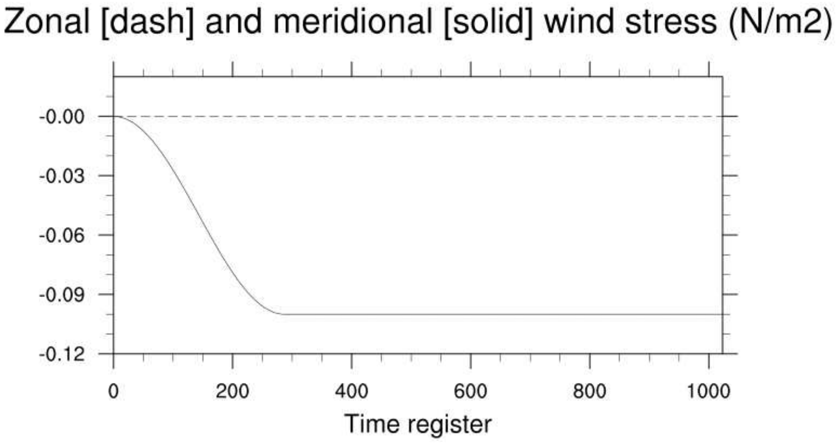

Figure 3.1: Wind stress. The negative sign indicates the southward direction of the wind.

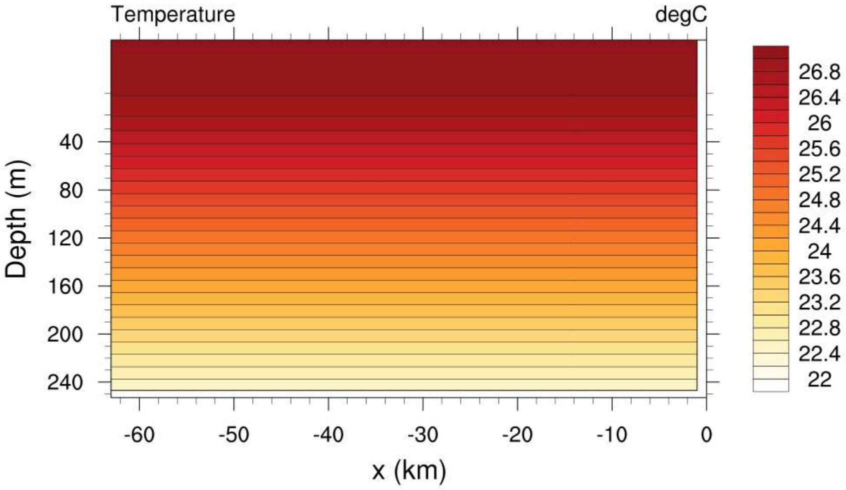

Figure 3.2: Initial temperature (degC) distribution.

et al. (2011). The configuration of the domain and the choices in the model set up and parametrization were in fact chosen to meet the analytical solution.

3.2.2 Data

We first examine the analytical solution to individuate the main features, which should be also present in our simulated upwelling. Figure 3.3 shows the density and along-shore velocity at the 6th day, for the analytical solution developed by Choboter et al. (2011). Results are shown for a flat bottom and a sloping topography. In both cases after this time the pycnoclines are tilted upward that indicates that dense water is being raised close to the coast. This distribution is a consequence of an offshore transport of water in surface, which is compensated by an onshore transport in the interior, and an upward motion at the coast, which is the typical upwelling-induced circulation. The offshore transport generates pressure differences between the coast and the open ocean. The pressure gradient formed generates a geostrophic current that flows in the alongshore direction. The presence of this current is evidenced in the along-shore velocity plots, where we can see a surface jet moving with the wind direction. In the flat bottom case, also an undercurrent is formed, with opposite direction and lower velocity.

The agreement of the numerical simulation is evident when looking at Figure 3.4, which shows the density and along-shore velocity for the model output at the 6th day. In order to make the data comparable with the analytical solution, all the fields are non-dimensional as in Choboter et al. (2011). The figures show vertical sections of a cross-shore transect taken at the middle of the computational domain. We chose a transect located far enough from the domain boundaries, in order to avoid possible interactions. The analysis focus only on this transect that is representative of the circulation, since the domain is homogeneous.

Besides the analytical case, the pycnoclines are shifted upward in the three experiments, but in this case they crop the surface close to the coast. The differences in density seen in the upper layers compared to the analytical solution are doubt to the existence of the Ekman mixed layer in the numerical simulation, which is not present in the analytical solution. Isopycnals in V1 (panel a) are further deflected downward in the presence of the undercurrent. The along-shore velocity plots (panels b, d and f) confirm the existence of an along-shore jet, which is also stronger in V2 (panel d) and V3 (panel f).

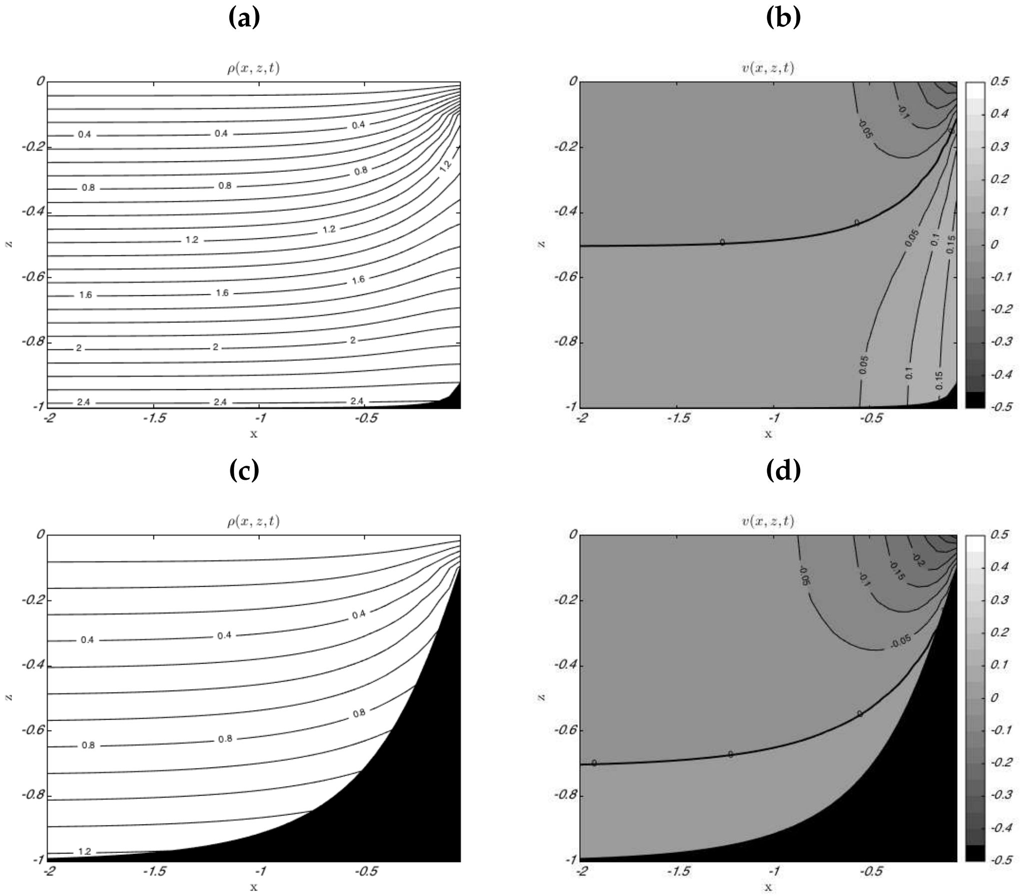

Figure 3.3: Snapshots of the adimensional density and along-shore velocity evaluated at the 6th day for the analytical solution with a flat bottom (upper row) and a sloping topography (lower row).

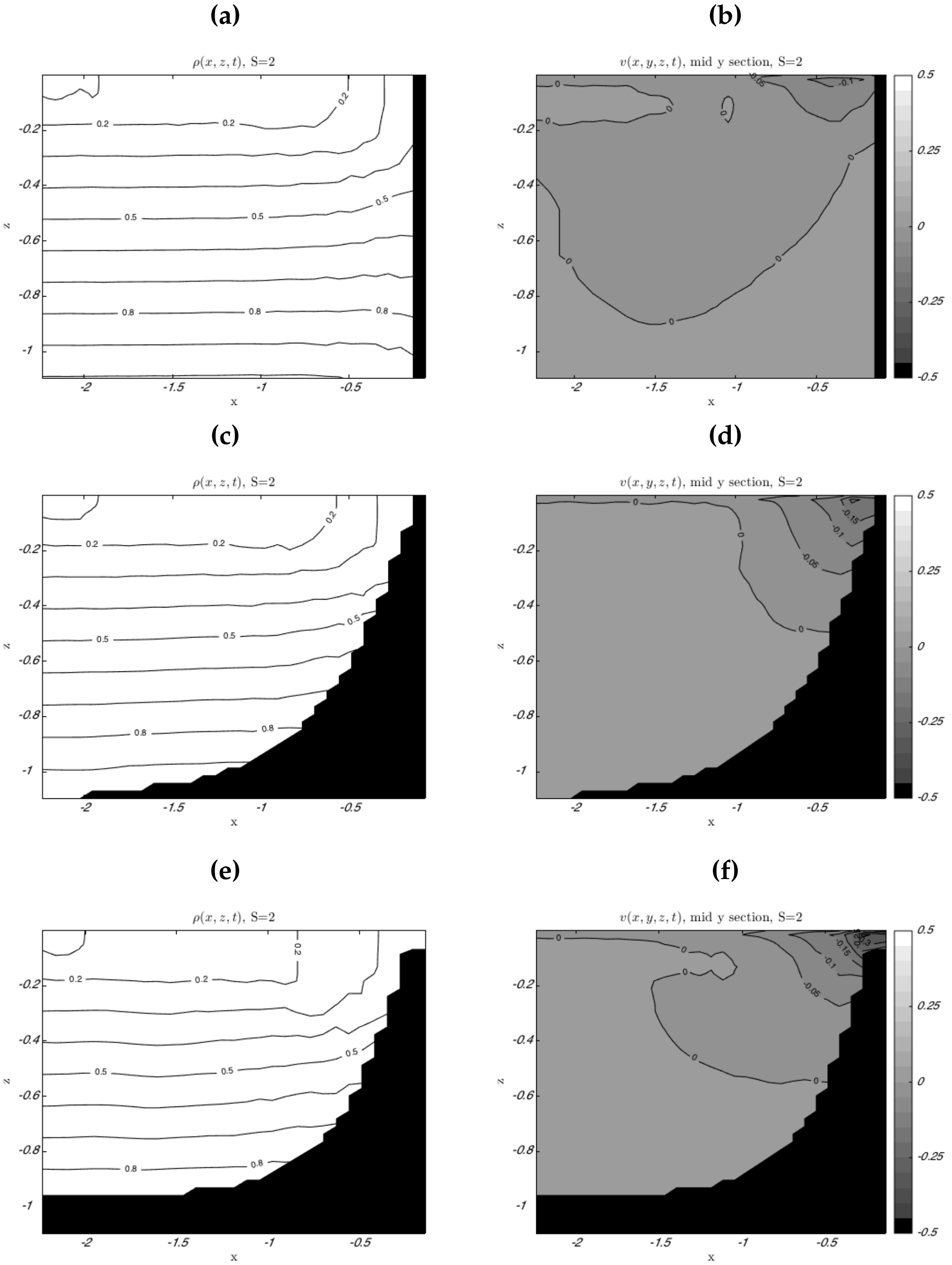

Figure 3.4: Snapshots of the adimensional density and along-shore velocity at the 6th day for the model output the flat bottom (upper row), the sloping topography (middle row) and the step-sloping topography (lower row) experiments. Contour intervals are 0.1 for the density and 0.05 for v. Zero contour is marked with a bold line in b and d.

Figure 3.5 gives more details of the induced circulation in the three experiments. The mean current is offshore in the upper layer, while a much weaker, onshore circulation dominates in the interior. Tilted temperature isolines indicate that the upwelling is set up near the coast. The isolines above 40 m outcrop forming an upwelling front, located at a few km from the coast. This front appears after the second day of simulation (when the forcing is fully set up), and moves offshore, as can be seen in Figure 3.6. The progression is nearly linear during the first days in all the simulations, and around the fifth day the front starts to oscillate. Figure 3.7 shows the instantaneous temperature and velocity fields at the end of the simulation.

While the mean fields are quite similar in the three simulations, and the differences are confined close to the coast, a look to the instantaneous fields reveals major differences (Figure 3.7). In addition to the undercurrent and the enhancement of the jet, the step-topography experiment confirms the important role of topography in shaping the circulation. The large step in V3 produces a small recirculation cell close to the coast, with part of the upwelled water moving towards the coast instead of offshore. A last feature visible in the instantaneous fields found in the the region close to the coast is the intense vertical mixing. Here, the mixed layer is around 80 m depth towards the end of the simulation, compared with a 40 m depth mixed layer offshore. The instantaneous fields of all the simulations show small perturbations at the base of the mixed layer.

3.3 Energy analysis

In this section we show the results for the energy analysis applied to the model output of each of the three experiments V1, V2 and V3. For the local MSEVA analysis, we use the code developed by Liang and Robinson (2005); the equations and symbols are described in Appendix A.

The pre-processing necessary for applying MSEVA is the interpolation of all the data to the same grid (i.e., the tracers grid). The stationary background density profile ($\bar{\rho}(z)$) is the horizontal and time average of the interpolated density data. The stationary profile is subtracted to the total density field. Accordingly, the dynamic pressure is also needed. The vertical density gradient is used to calculate the Brunt-Väisala frequency. We perform a two scale decomposition as we did in Chapter 2. The limits of the transform are hence $j_0 = 0$ and $j_1 = j_2 = 10$ (the length of the series, 6.7 days and the maximum resolution of the data, 600 s).

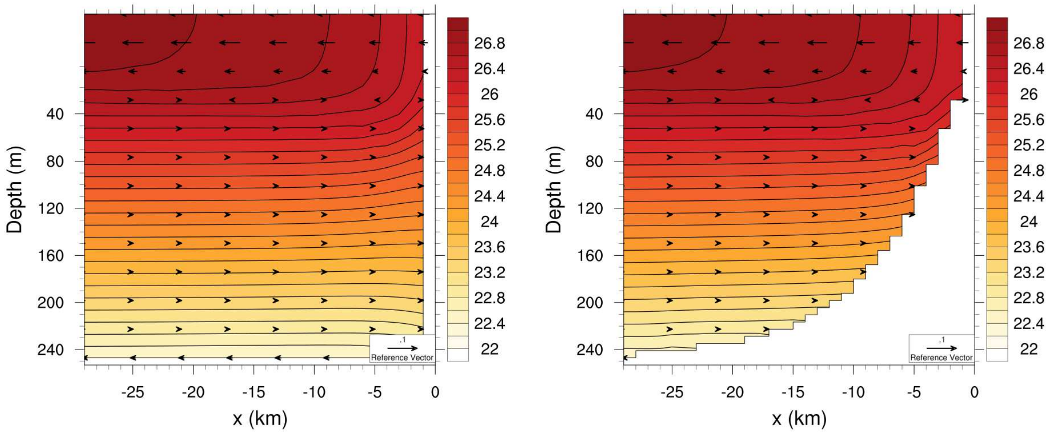

(a) V1 **(b)** V2

(c) V3

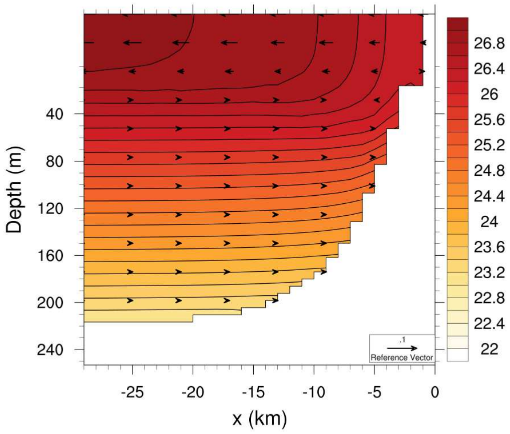

Figure 3.5: Cross-shore section of mean temperature (degC) and velocity (m/s).

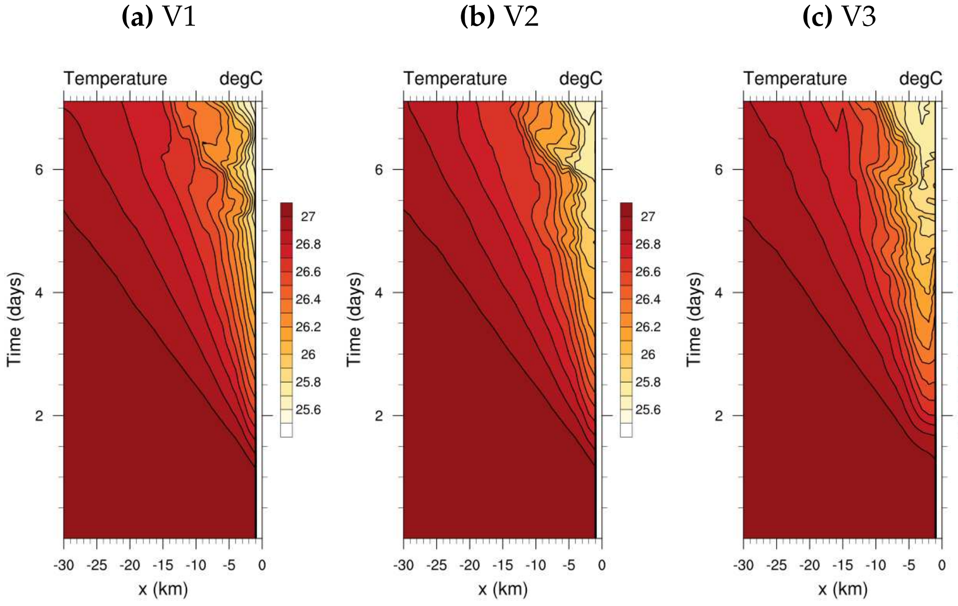

(a) V1 **(b)** V2 **(c)** V3

Figure 3.6: Hövmoller diagrams for the three experiments showing the time-longitude variation of surface temperature (degC). A surface temperature front advance from the coast from the first day of simulation, moving offshore.

Figure 3.8 shows the energy averaged over the cross-shore transect and integrated over the column depth. In all the experiments, both MKE and EKE grow during the first days (when the wind increases gradually), and after a few days, energy starts to fluctuate. While EKE is around 0.03 m^2/s^2 in the three cases, the MKE content is larger in the V2 and V3 simulations, due to the larger velocities. The fluctuations are also stronger in the third run. The energy oscillations can be related to the stability of the upwelling front shown in Figure 3.6.

The wind forcing is the same in the three simulations. However, the wind stress work varies from one experiment to the other (Figure 3.9). The wind stress work is the kinetic energy input in the surface ocean by the wind, computed as the scalar product between wind stress and the surface ocean velocity, $W = \boldsymbol{\tau} \cdot \mathbf{U_h}$. In the three cases, there is a maximum of energy input close to the coast, while offshore the wind work decreases to a nearly constant value of 0.005 N/ms. The minimum is reached around 14 km. This is the area where the coastal upwelling is active, and where the energy dynamics concentrates. Applying the Reynolds decomposition to the wind work:

$$\overline{\boldsymbol{\tau} \cdot \mathbf{U_h}} = \overline{(\bar{\boldsymbol{\tau}} + \boldsymbol{\tau}') + (\overline{\mathbf{U}_h} + \mathbf{U}_h{}')} = \bar{\boldsymbol{\tau}} \cdot \overline{\mathbf{U}_h} + \overline{\bar{\boldsymbol{\tau}} \cdot \mathbf{U}_h{}'} + \overline{\boldsymbol{\tau}' \cdot \overline{\mathbf{U}_h}} + \overline{\boldsymbol{\tau}' \cdot \mathbf{U}_h{}'} \qquad (3.2)$$

The terms depending on $\boldsymbol{\tau}'$ vanish because the wind is homogeneous, hence

(a) V1 **(b)** V2

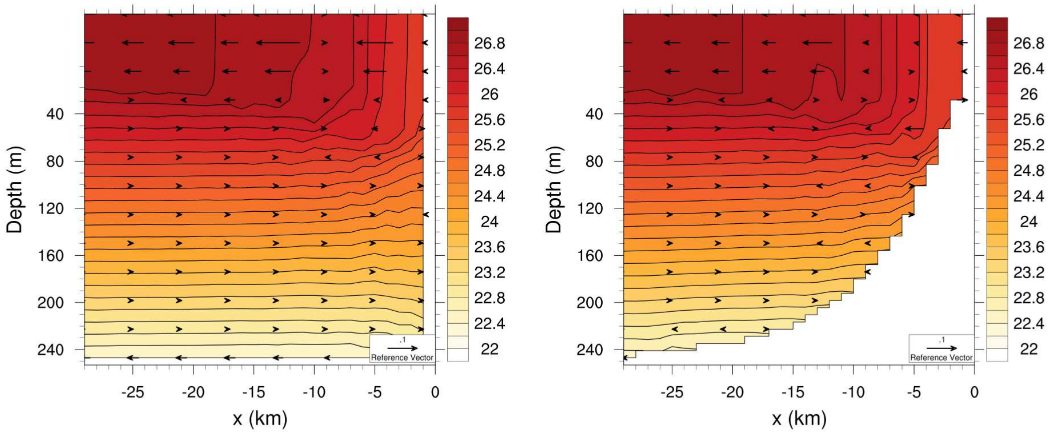

(c) V3

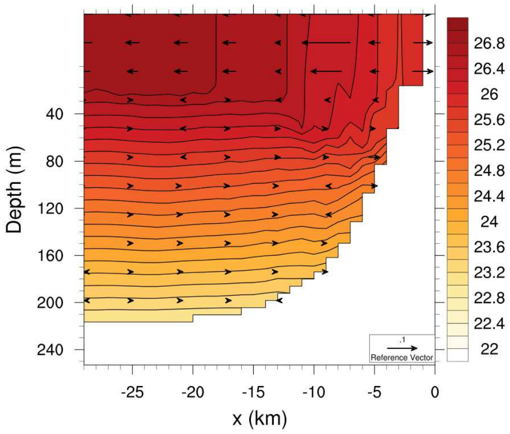

Figure 3.7: Cross-shore section of temperature (degC) and velocity (m/s). Snapshot at the end of the simulation.

(a) V1

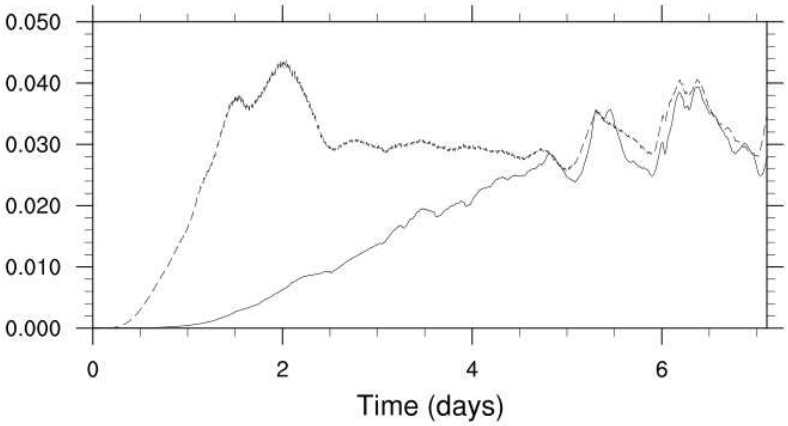

(b) V2

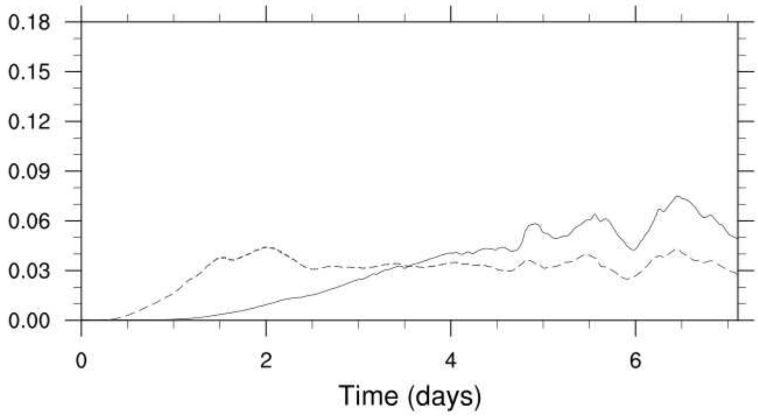

(c) V3

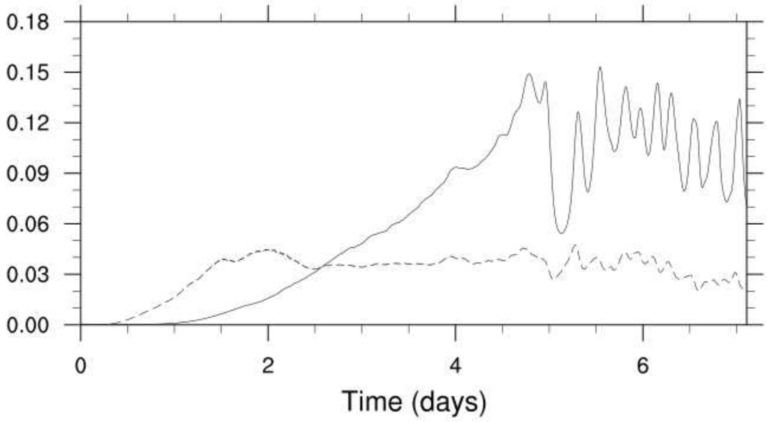

Figure 3.8: Mean Kinetic energy (solid line) and Eddy Kinetic energy (dashed line) for experiments V1, V2 and V3, in m^2/s^2.

$\boldsymbol{\tau}\prime = 0$. Also the second term is zero since $\bar{\boldsymbol{\tau}}$ is constant and $\overline{\mathbf{U}_h{}'} = 0$. Therefore for a wind field that is homogeneous and constant, the total wind stress is equal to the mean wind stress, and all the work is done by the mean fields. Since the rate of energy input is related to the current velocity, larger values are found in the presence of topography, where the current is stronger.

The spatial distribution of energy is evaluated in the next figures by looking at each term in the energy equations. Panels are plotted in a blueish to red based colormap, where blue colors correspond to local export of energy (hence a reduction in time) and red colors indicate a local import (an increase) of energy.

Panels in Figures 3.10, 3.11 and 3.12 show the mean available potential energy terms for the large scale and the mesoscale for each of the experiments. Looking at the large scale figures (left panels), we notice that the mean rate of change of APE (panel a) is positive in the 3 experiments, but only close to the coast. The change is larger in the presence of topography (V2 and V3) than in the flat bottom experiment (V1). A region of negative change is seen below the maximum in the case of topography. Lateral advection (panel b) is one of the major terms, acting to redistribute the energy. It is always positive at 4 km to the coast at subsurface (even if the depth of this maximum is affected by the presence of topography), and negative just below. This feature corresponds to the zonal transport: offshore in surface, onshore below the mixed layer. There is also a region of negative lateral advection attached to the coast, due to the coastal jet. A large path of negative values can be related to the undercurrent in the flat case, while in the topography cases, small positive values are seen following the bathymetry. Note that the dipole positive/negative often seen at about 2 km off the coast is due to the separation of the effective upwelling from the coast. In the V1, the vertical advection (panel c) presents negative values that are spread in the mixed layer except close to the coast, where a maximum is verified. In the presence of a topography, features close to the coast are enhanced, till the point that and in V3 all the activity is concentrated here. The dipole seen in V3 is a consequence of the recirculation cell.

Buoyancy (panel d) is not a main term for the APE change; however, it is interesting since it connects the two types of energy, and we anticipate that it will be important in the KE. Negative values are seen around 3 km off the coast, coinciding with the ascending branch of the upwelling, where cold water is lifted upwards, therefore indicating a conversion to large scale KE. The presence of the topography modifies this pattern, and in V3 it is clear the signature

(a) V1

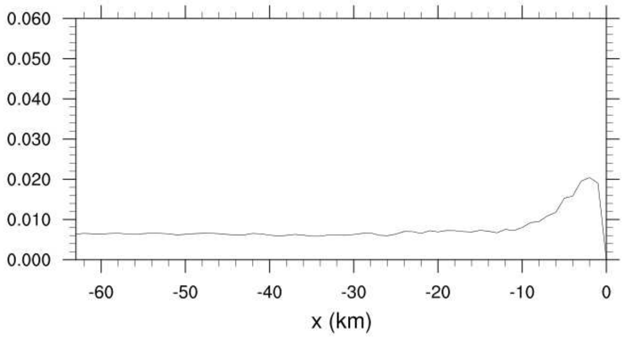

(b) V2

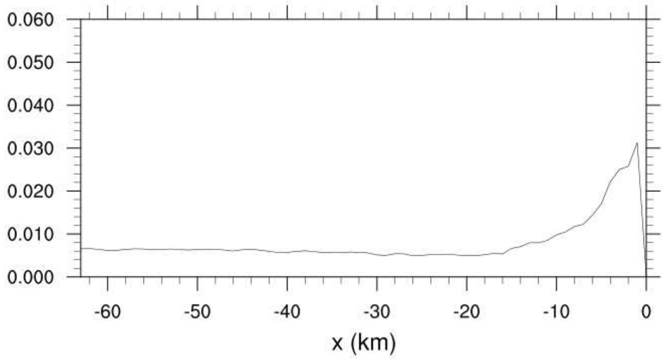

(c) V3

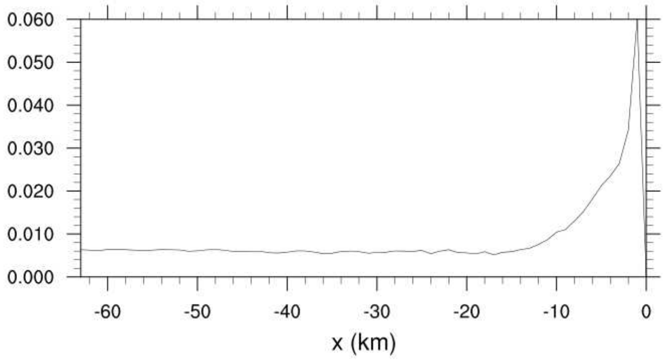

Figure 3.9: Rate of wind energy input (N/ms) to the ocean for experiments V1, V2 and V3. Note the scale in (a) is different.

of the recirculation cell. What happens in V3 is that the mass of water that is recirculated above the step rises close to the coast and, in its way offshore, it encounters the front formed by the main rising jet (at around 3 km). Here, it sinks (hence the positive buoyancy) and moves again to the coast near the bottom.

The transference (panel e) in all the cases is negative at subsurface, and positive below. In V1, a strong influence of the undercurrent is seen. This term is one of the largest, approximately balancing the lateral advection. We remark here that the total transference term includes the exchange of energy between the two scales, plus the transference from other locations within the same scale (Liang, 2002). The fact that most of the transferences coincide with the transference between the large and the mesoscale (panel f) indicates that they contribute mainly to the baroclinic conversion.

Focusing on the mesoscale (right panels), again the mean rate of change (panel a) is positive in the 3 experiments close to the coast, and larger in the cases with topography. In general, mesoscale APE changes (the single panels) are various orders of magnitude smaller than the large scale, and the variations depend on the perturbation from the mean stratification.

Lateral advection (panel b) presents a series of maxima and minima at the base of the mixed layer, corresponding to oscillations propagating there. In V3, however, the dynamics created above the step are dominating, and the main feature is the dipole produced by the recirculation cell. Vertical advection (panel c) presents a patch of negative values in the mix layer that extends offshore.

Mesoscale buoyancy (panel d) in V1 is predominantly negative, suggesting a conversion to mesoscale KE that is maximum in the mixed layer, around 8 km of the coast. The topography affects the buoyancy conversion, even producing a positive patch (hence conversion from KE to APE) close to the coast, where the column is completely mixed, and cold water sinks. This feature is more evident in the third experiment (V3, where the positive conversion is located at the downwelling branch of the recirculation cell).

In V1, transferences (panel e) increase the energy at the base of the mixed layer, while in V2 and V3 negative values appear close to the topography. Transferences leading to baroclinic instability are enhanced in V2 and V3, where larger values of the baroclinic conversion terms (panel f) are seen.

The mean large scale and mesoscale kinetic energy terms are shown in Figures 3.13, 3.14 and 3.15 for each experiment. Focusing on the large scale (left panels), the mean rate of change of large scale KE (panel a) is positive in the 3 experiments and maximum close to the coast, enhanced by the topography.

Lateral advection (panel b) is positive offshore, and the peculiar shape in the V3 experiment is due to the recirculation cell. Vertical advection (panel c) is positive at the surface and slightly negative close to the coast when topography is flat. Values are much larger close to the coast in V2 and V3.

The buoyancy term (panel d) is similar as in the APE terms, but with opposite sign. A positive conversion occurs a little offshore and in the first 40 meters, while the enhanced mixing and recirculation in the topography experiments have a relevant signature. Note that now buoyancy is not a minor order term as in the APE, but it is a major term in energizing the large scale KE.

Pressure work (panels e and f) is positive attached to the coast in all the experiments. In the V1 case, a signature of the undercurrent is visible as a large patch of positive values on the lateral pressure work (panel e). Negative values of lateral pressure work are seen at surface levels in all the experiments. This term is a second order term in all the experiments, not being so important for the energy changes.

The transference term (panel g) is negative close to the coast, with larger values in the cases in which topography is present (V2 and V3). Furthermore, this loss of energy can be attributed to barotropic transferences (panel h).

Concentrating in the mesoscale (right panels), we see that the energy increases in time (panel a) close to the coast in all of the 3 experiments, and the change is larger in V2 and V3. The rate of change is negative in the upper layers offshore.

Lateral advection (panel b) is the main term in the mesoscale, counterbalanced mainly by the transference term. It implies an increase of energy offshore, and a loss of energy close to the coast. Again, we can see the signature of the topography which enhance and confine the pattern close to the coast. In the case of V3 a strong dipole evidences the recirculation cell.

Vertical advection (panel c) is positive at the surface and slightly negative close to the coast when topography is flat (V1). It is greatly enhanced close to the coast in the other two cases. In V3, positive values are seen close to the coast.

Buoyancy conversion (plot d) is an input of energy also for the mesoscale. The signature of the recirculation is seen in both vertical advection and the buoyancy conversion terms.

As in the large scale, the pressure work (panels e and f) is a second order term. Its variation is, in any case, concentrated at the base of the mixed layer and attached to the coast.

The transference term (panel e) is positive close to the coast in all cases, leading to a positive barotropic conversion (panels f) that is larger in the cases with topography (V2 and V3).

The mean energy patterns investigated so far showed that the mean circulation and stratification rules the large scale dynamics, while the mesoscale can be related to perturbations. This is more evident when looking at the instantaneous maps (not shown): large scale terms generally increase their values with time, while the mesoscale presents a series of maxima and minima that are the signature of small perturbations, propagating mainly in the mixed layer. As a result, mean mesoscale fields show more or less homogeneous patterns intensified either in the mixed layer or at its base. The main terms in both APE and KE at any scale are usually advection and transferences, which usually compensate between them. However, the main pattern is related to buoyancy conversion and inter-scale transferences leading to mixed instabilities. The topography plays a role in enhancing the currents and concentrating the dynamics close to the coast. Secondary circulation patterns may be induced by some features in the topography as in V3, where a small recirculation cell is formed.

3.4 Summary and discussion

In this chapter we performed three idealized experiments reproducing a simple coastal upwelling with different coastal topographies. The model configuration was similar in the three experiments, appart from the topography shape. We applied a stationary and homogeneous upwelling favorable wind to a resting ocean with stable stratification. Within a few days, the wind generated a coastal upwelling in the eastern part of the basin.

The main features of the upwelling circulation are well represented in our simulations. Indeed, our results were coherent with the exact analytical solution found by Choboter et al. (2011). The typical circulation was found in each of our experiments: surface water is transported offshore, while a compensating onshore flow develops in depth. Pressure anomalies between the coast and interior lead to a coastal meridional jet directed to the south and an undercurrent in the case of no topography.

The exploration of the spatial patterns of energy associated with this circulation allowed us to point out the main processes involved in the upwelling.

Energy changes are mostly concentrated within a few kilometers from the coast. This is the area where the upwelling is active, where the wind work (and hence the energy input) to the ocean is maximum. The surface mixing in this area is intense and also the change of the background stratification. The isopycnals here pass from being horizontal to crop the surface forming a density front that moves offshore. After a few days, the front becomes unstable and starts to oscillate, and this is also reflected in the energy contain.

The upwelling dynamics are reproduced in the large scale. This is reasonable, since there is no background circulation in the idealized experiments (the initial state is motionless) and all the motion is generated exclusively by the wind action.

The dominant terms in the large scale APE and KE are the transports associated to the large scale flow. Lateral advection reflects the upwelling circulation, with a local exportation of energy in surface offshore corresponding to the offshore Ekman transport and importation at subsurface compatible with the onshore compensating flow. The signature of the alongshore geostrophic current is also visible in the transport terms, inducing a local export of energy. Although the transport terms are dominant, they only serve to redistribute energy within the domain.

Ekman pumping is the center of the upwelling dynamics. Its effects are seen in two terms: the vertical advection and the buoyancy conversion, which are important in the mixed region. This is the area where most changes in the density isolines occur: first because it is the region where upwelling starts, later because the front is constantly moving offshore. A net generation of KE occurs due to buoyancy conversion along the rising branch, where cold water is lifted upward.

While the large scale is linked to the basin scale circulation and reflects closely the upwelling circulation, the mesoscale is related to the deviations from the mean state. Indeed, the mesoscale energetics show mainly the oscillations of the front, appearing as a series of maxima and minima at surface and along the base of the mixed layer. The presence of mixed instabilities was confirmed by positive values of the barotropic and baroclinic terms, which occur in the very first km from the coast.

With our experiments, we also wanted to evaluate the effect of different topographies on the circulation. The presence of a topography modulates the energetics by affecting the circulation. The topography enhances the coastal current, confining it closer to the coast. The resulting current is narrower and stronger, leading to larger amounts of energy contains in each scale. As a consequence, energy patterns, especially the ones directly related to the advection (transport and transference terms) are more intense and concentrated at the coast when a sloping topography is included. In particular, the formation of instabilities (identified with the baroclinic and barotropic terms) is amplified in the presence of a topography.

The existence of the undercurrent can occur only when the topography is deep enough. The undercurrent was also absent in the analytical solutions of Choboter et al. (2011), but the energy analysis pointed at its importance in redistributing the energy via lateral advection.

The presence of shallow features in the bathymetry can largely affect the circulation, modifying the basic pattern. This is what happens in our experiment V3, where the existence of a shallow step close to the coast generated the formation of a two-cell circulation. The dynamics induced by this feature differ from the basic upwelling, as demonstrate the presence of dipole patterns in the energetics of the V3 case. This behavior recalls the problem of whether the upwelling circulation is characterized by one cell or a multi-cell structure (Brink, 1983). The structure of the upwelling overturning cell is illustrated by Estrade et al. (2008) with an analytical model. Their results support the observed upwelling separation from the coast with dynamical arguments and link the size of the cell to the shape of the bathymetry. In our case, the small cell is probably magnified by the stair-shaped bathymetry, and it could be comparable to what happens in the case of having a narrow shelf as the Oregon and Sydney shelfs (Allen et al., 1995; Marchesiello et al., 2000).

The energy path can be summarized as follows: the energy input by an homogeneous and constant wind stress is imposed directly to the large scale ocean circulation. The wind increases the large scale basin energy in two ways: on one side, the wind-forced circulation and the Ekman pumping induce changes in the background stratification that release available potential energy. These changes in the stratification are actually produced by the vertical movement of water. Indeed, vertical advection is in general a source of APE close to the coast in both large and mesoscale. Since the upwelled water is also denser than its surroundings, part of the APE is converted to KE via the buoyancy term. On the other side, the wind directly increases the basin kinetic energy by transferring momentum to the surface. All this energy is redistributed within the domain by the main currents via lateral advection.

While the large scale correlates with the basin scale circulation, the mesoscale is related to small perturbations and instabilities. Both large scale KE and APE are sources of energy for the mesoscale circulation via barotropic and baroclinic conversion, which occur in the very first km from the coast. Schematically, the main path that energy follows can be represented as follows:

$$\begin{tikzcd}
 & \textbf{Wind Work} \arrow[dl, dashed] \arrow[d, Rightarrow] \\
\mathbf{APE^L} \arrow[r, "b^L"] \arrow[d, "BC"'] & \mathbf{KE^L} \arrow[d, "BT"] \\
\mathbf{APE^M} \arrow[r, "b^M"'] & \mathbf{KE^M}
\end{tikzcd}$$

Figure 3.16: Scheme illustrating the main energy paths in the idealized experiments. APE is Available Potential Energy, KE is the Kinetic Energy. b is the buoyancy conversion. BC and BT are the baroclinic and barotropic indicators, respectively. Superindexes L and M in the terms stand for large scale and mesoscale.

The method is not absent of limitations. For example, we used here a two scale decomposition to be consistent with the Chapter 2. However, the scale decomposition is not unique, in the sense that different scale decompositions can be obtained by changing the window limits of the transform. The selection of the scale limits is done by visually inspecting the energy spectra, involving necessarily a subjective interpretation. We noticed that the energy balances were not perfectly closed. The causes are various: the energy equations were derivated from the Primitive Equations written in the flux form, differing from the vector-invariant form of the equations in our simulation. Numerical errors can arise also from the fact that the balances involve the summation of very small negative numbers. In addition, our balances lack two terms: the wind work and the friction. The wind work is not an input term to the energy equations. Still, since the equations are just diagnostics, its effect is included in the equations through the changes in the state variables. The energy dissipation is not accounted in the balances. In despite of these deficiencies, the energy analysis allowed us to identify the main path of energy associated to the reproduced upwelling. It proves its potentiality for evidencing the physical processes underpinning oceanic processes, which makes it a useful diagnostic tool to assess the model representation of physical processes.

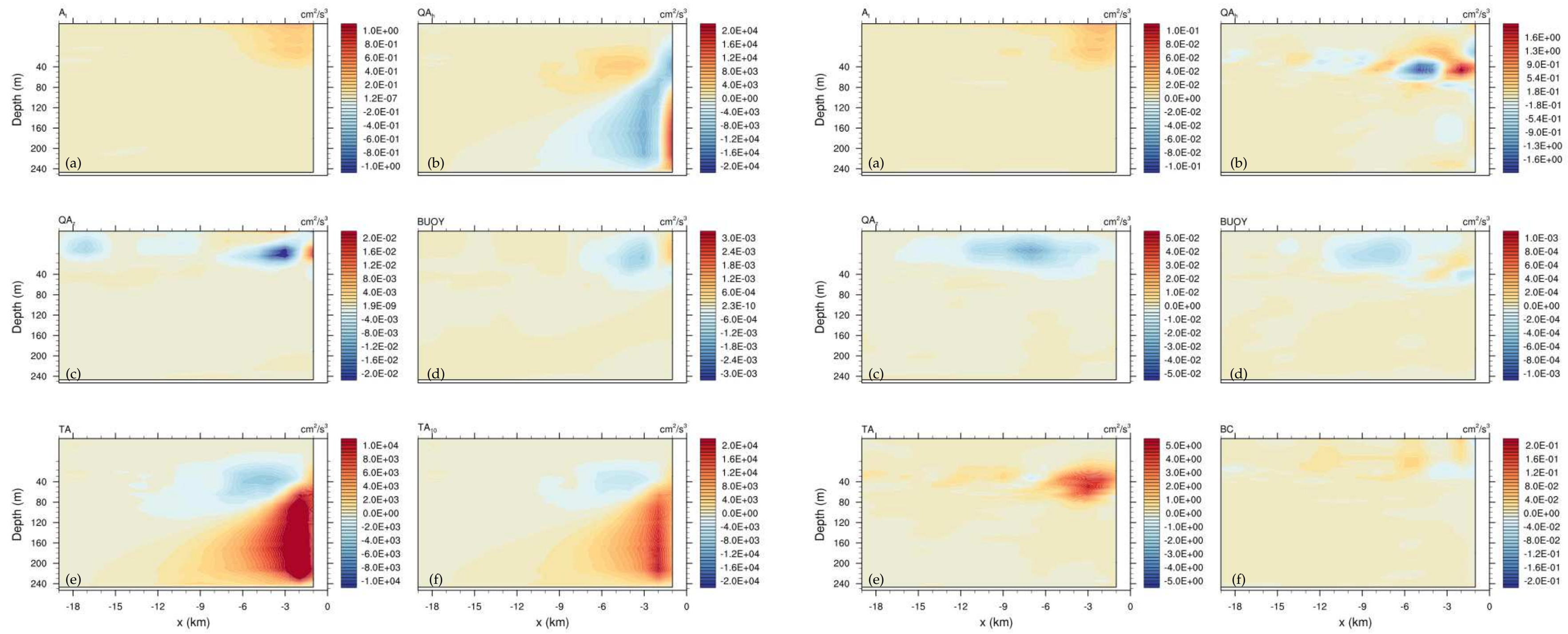

(a) Large scale.

(b) Meso scale.

Figure 3.10: Mean APE terms for V1 in cm^2/s^3. Terms in each panel are the time rate of change of available potential energy (a), horizontal (b) and vertical (c) advection of energy, buoyancy conversion (d), total transference term (e) and large-mesoscale transference (f), which in the case of the mesoscale is the Baroclinic Term (h in right panel).

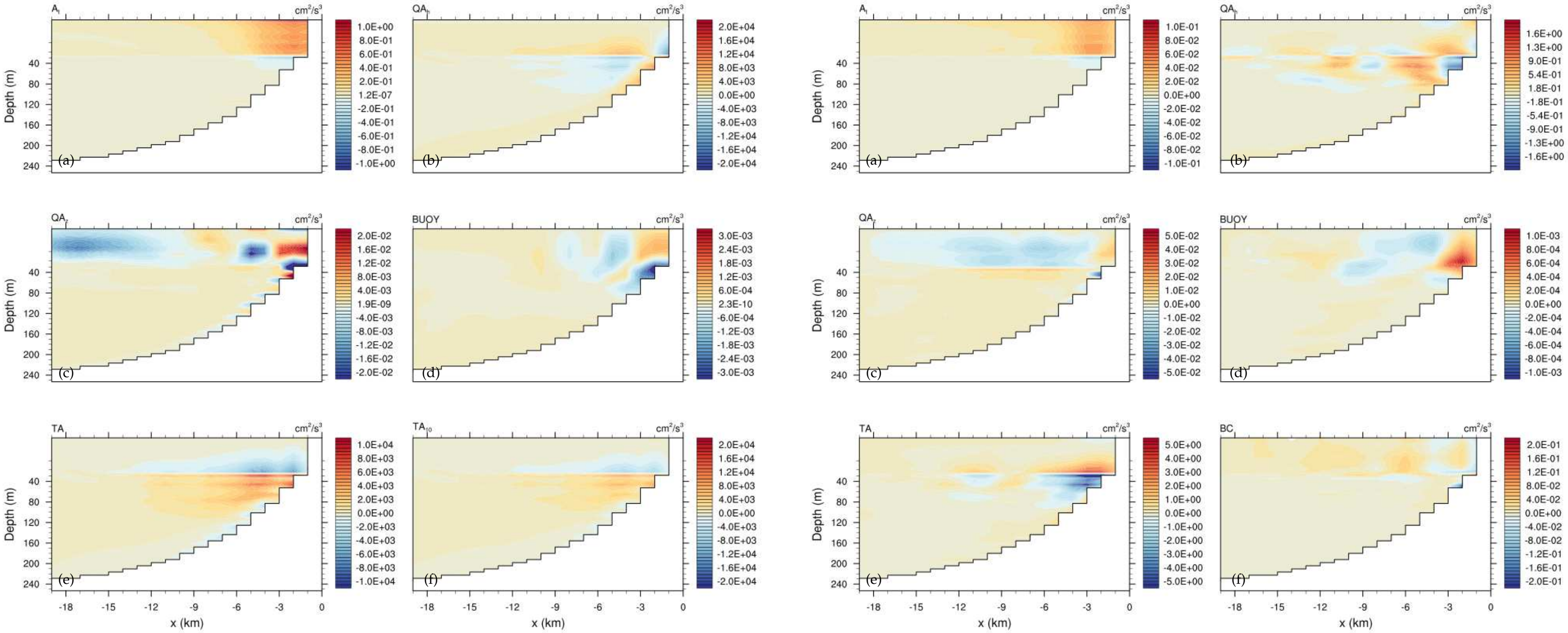

(a) Large scale.

(b) Meso scale.

Figure 3.11: Mean APE terms for V2 in cm^2/s^3. Terms in each panel are the time rate of change of available potential energy (a), horizontal (b) and vertical (c) advection of energy, buoyancy conversion (d), total transference term (e) and large-mesoscale transference (f), which in the case of the mesoscale is the Baroclinic Term (h in right panel).

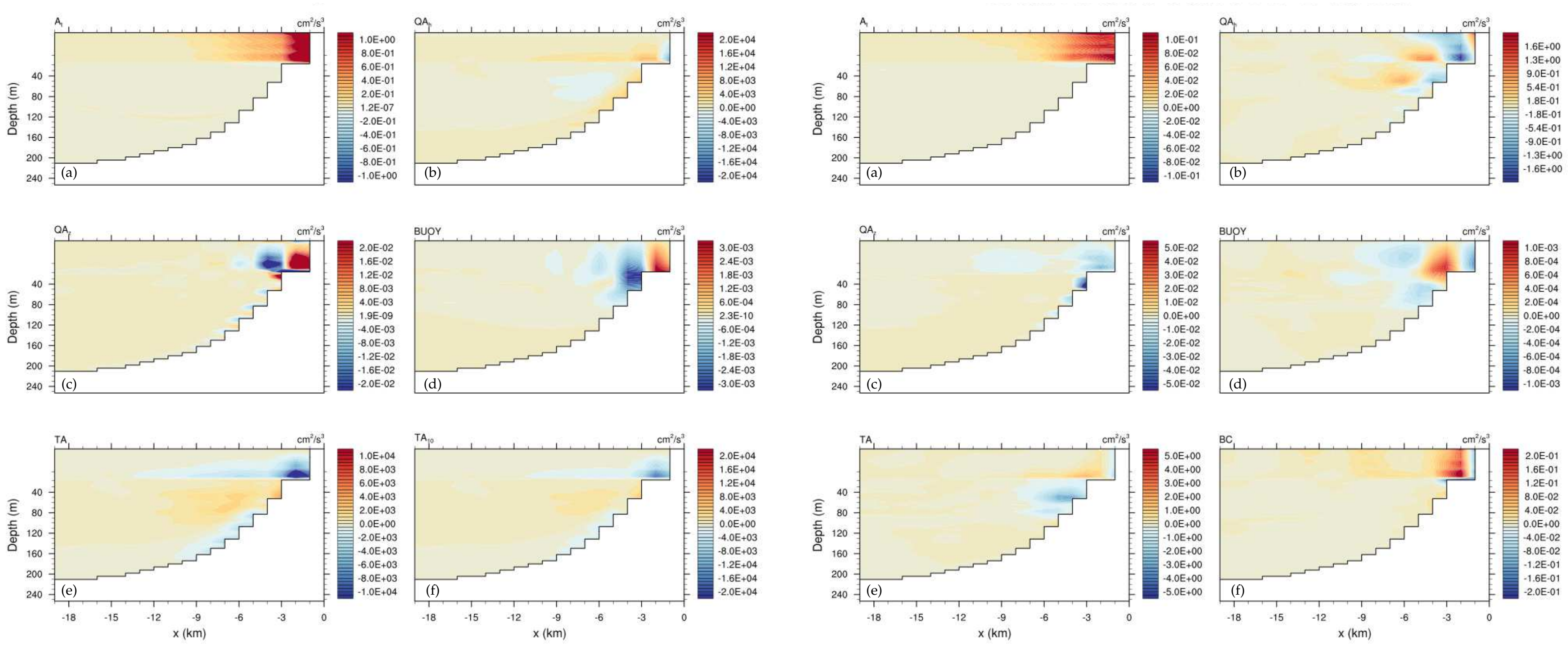

(a) Large scale.

(b) Meso scale.

Figure 3.12: Mean APE terms for V3 in cm^2/s^3. Terms in each panel are the time rate of change of available potential energy (a), horizontal (b) and vertical (c) advection of energy, buoyancy conversion (d), total transference term (e) and large-mesoscale transference (f), which in the case of the mesoscale is the Baroclinic Term (h in right panel).

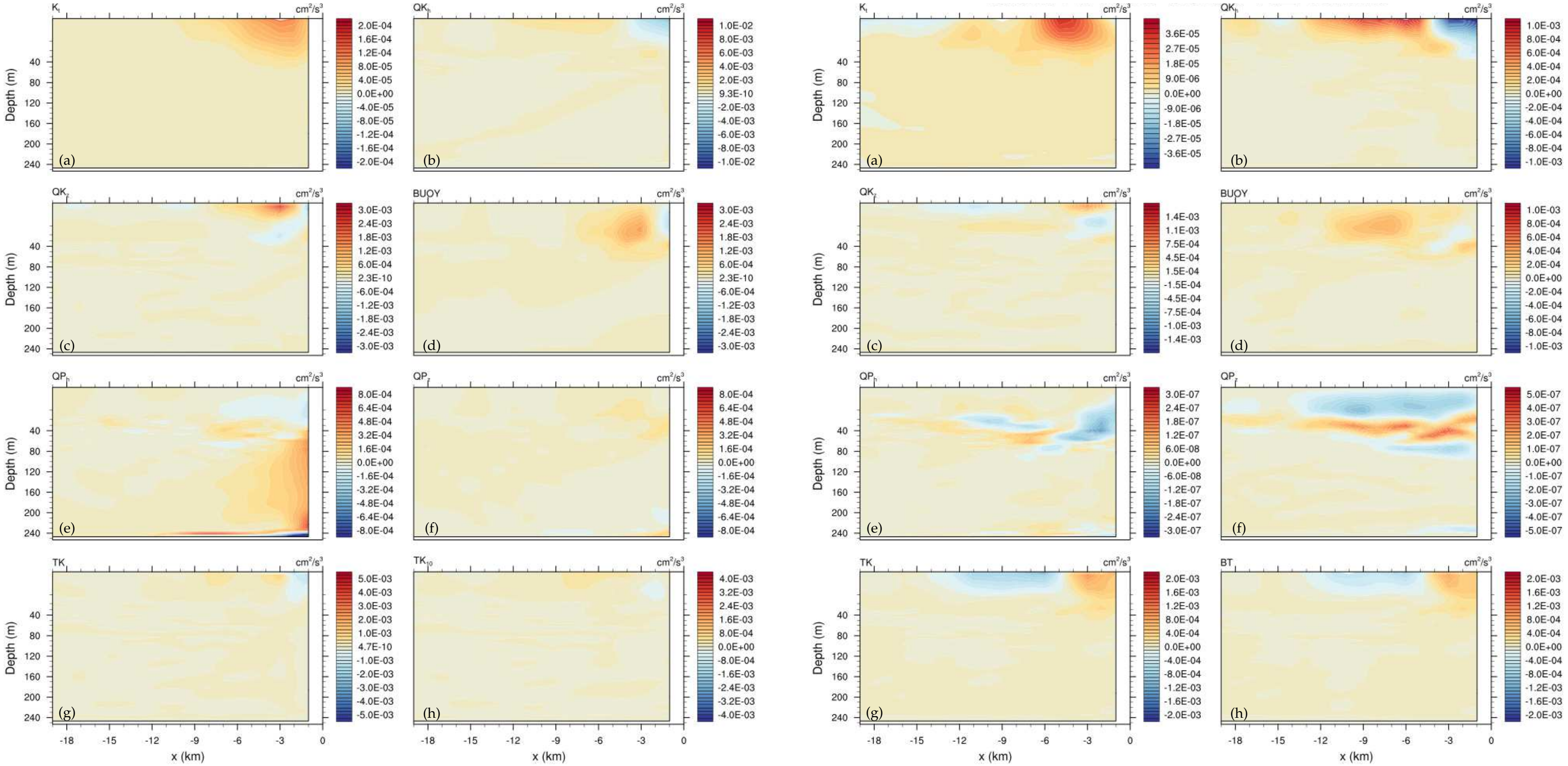

(a) Large scale

(b) Meso scale

Figure 3.13: Mean KE terms for V1 in cm^2/s^3. Terms in each panel are the time rate of change of kinetic energy (a), horizontal (b) and vertical (c) advection of energy, buoyancy conversion (d), horizontal (e) and vertical (f) pressure work, total transference term (g) and large-mesoscale transference (h), which in the case of the mesoscale is the Barotropic Term (h in right panel).

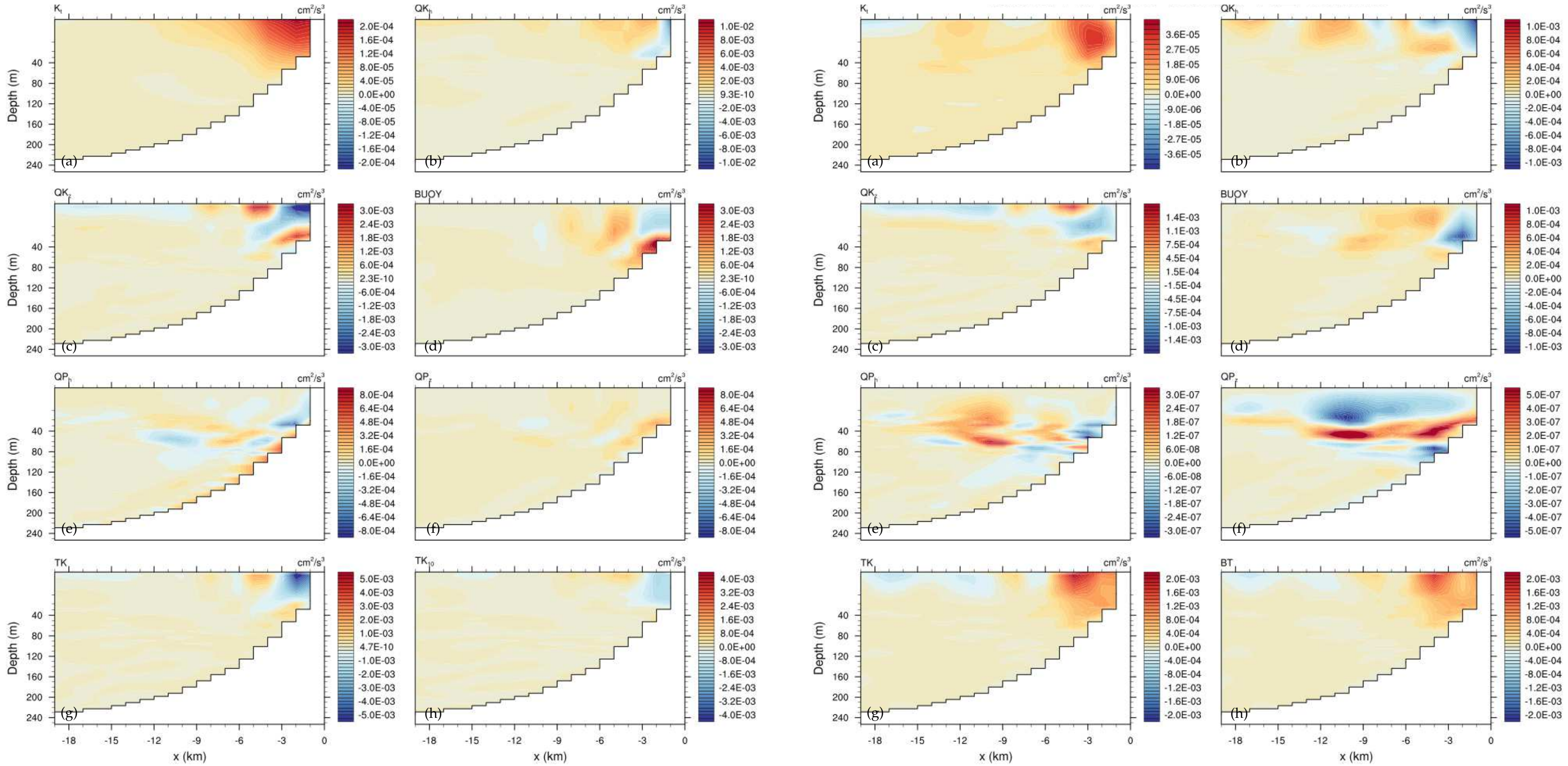

(a) Large scale

(b) Meso scale

Figure 3.14: Mean KE terms for V2 in cm^2/s^3. Terms in each panel are the time rate of change of kinetic energy (a), horizontal (b) and vertical (c) advection of energy, buoyancy conversion (d), horizontal (e) and vertical (f) pressure work, total transference term (g) and large-mesoscale transference (h), which in the case of the mesoscale is the Barotropic Term (h in right panel).

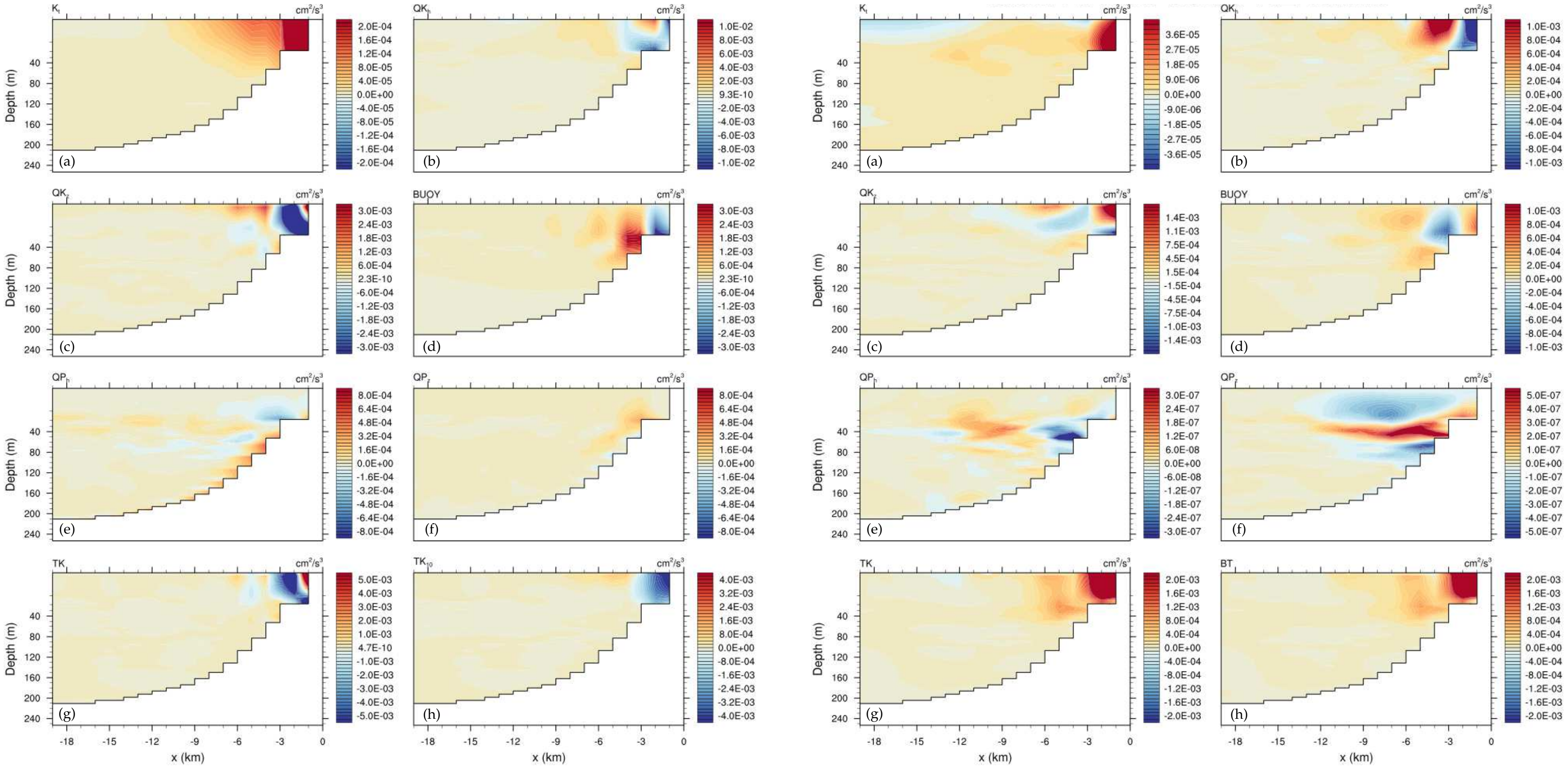

(a) Large scale

(b) Meso scale

Figure 3.15: Mean KE terms for V3 in cm^2/s^3. Terms in each panel are the time rate of change of kinetic energy (a), horizontal (b) and vertical (c) advection of energy, buoyancy conversion (d), horizontal (e) and vertical (f) pressure work, total transference term (g) and large-mesoscale transference (h), which in the case of the mesoscale is the Barotropic Term (h in right panel).

Chapter 4

Dynamics of an upwelling: a realistic simulation

4.1 Introduction

The Mediterranean variability is closely related to the atmospheric forcing. Both momentum and heat fluxes play a role in shaping the Mediterranean circulation at the different scales of variability. The wind variability can explain interannual changes in the circulation and the transport trough the strait of Gibraltar, while heat fluxes are important at the scales at which deep water is formed. The presence of intense, persistent wind regimes (most of them shaped by the orography that generates a channeling effect) makes it one of the main forces driving the circulation, and it is also important for the kinetic energy as evidenced by Pinardi and Masetti (2000).

Since the Mediterranean Sea is surrounded by coasts, the occurrence of upwelling during wind events is high, and widely spread (Figure 4.1). Because of the varying relief of the coastline, the upwelling distribution presents a highly complex spatial pattern as has been shown by (Antonijuan Rull et al., 2015). Despite that, main areas of upwelling are identified, and linked to a seasonality inherent to the wind characteristics. Intense upwelling zones are found in the eastern Aegean Sea, over the west coast of Greece and in the gulf of Lyons, while the southern coast is mainly a downwelling area (Antonijuan Rull et al., 2015). Other areas where upwellings have been noted are the Gulf of Lions due to Mistral winds (Minas (1968), Estrada, 1999), the Adriatic, Ligurian and Tyrrhenian, the catalan coast of Spain (Margalef and Ballester (1967), Fiúza (1983), Estrada (1996)). Around the largest islands, there is a tendency of upwelling on the western and southern coasts, and downwelling on the northern and eastern parts (Bakun and Agostini, 2001).

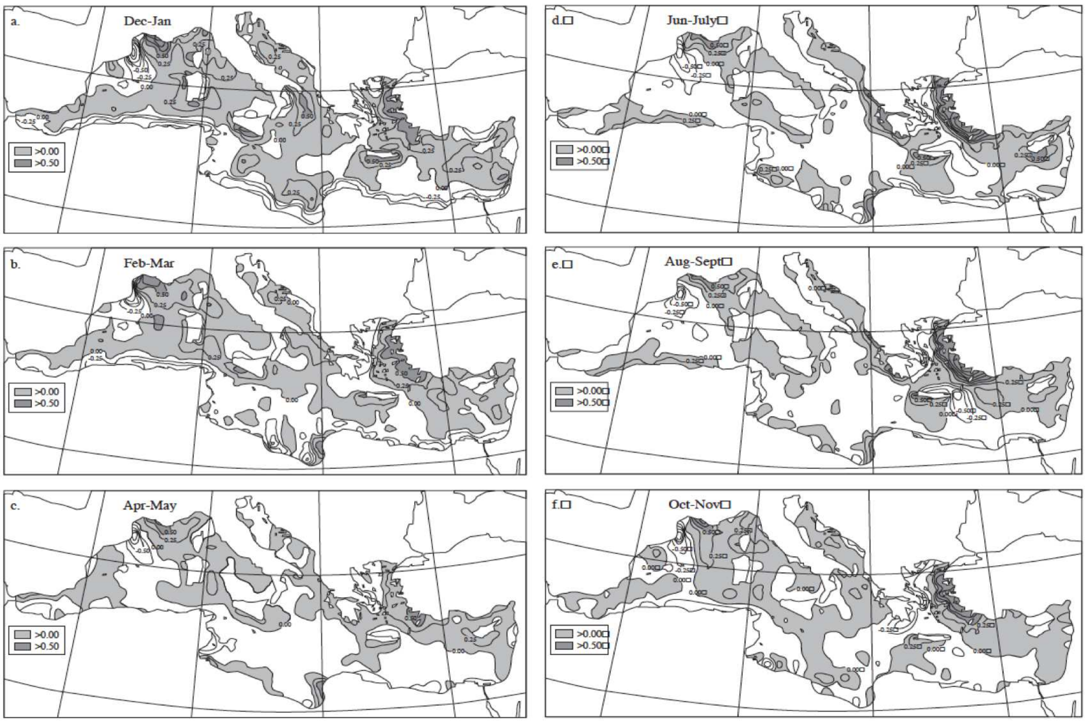

Figure 4.1: Seasonal variation of vertical velocities at the bottom of the surface Ekman layer (m/day). Contour interval is 0.25. Shaded areas indicate zones of upwelling. Darker shading indicates upward velocities greater than 0.5 m/day. Unshaded areas indicate zones of downwelling. From Bakun and Agostini (2001).

In this chapter we deepen into the upwelling dynamics by applying the energy analysis to a realistic simulation of the Mediterranean Sea. For the realistic simulation, we used an atmosphere-ocean coupled model. The reason we used a coupled model and not an ocean forced model is because, although this thesis is focused on the study of oceanic and not atmospheric processes, the method can be applied also to the atmosphere (San Liang, 2016). It was our intent to use a simulation that could potentially serve for both atmospheric and oceanic processes, in view of future works. This chapter is a continuation of the previous one, where we explored the dynamics of an idealized simulation, while we attempt to improve our knowledge about one of the most common processes happening in the Mediterranean.

4.2 Experiment configuration

4.2.1 Model description

The model employed is the regional atmosphere-ocean coupled model for the Mediterranean Sea (COSMO-NEMO-MFS).

The atmospheric component is COSMO-CLM (Rockel et al., 2008), the climatological version of the COSMO model developed at the Deuthscher Wetterdienst (DWD). The COSMO model is a non-hydrostatic, limited-area, atmospheric model. The basic equations are the thermo-hydrodynamical, fully compressible equations in a moist atmosphere, formulated in rotated geographical coordinates and a terrain following height coordinate. The atmospheric component is implemented with a spatial resolution or 44 km and 40 vertical levels. The configuration of the COSMO model used is the one described in the V4 configuration in Cavicchia et al. (2015).

The ocean component is NEMO-MFS (Oddo et al., 2009), the regional configuration of the Nucleus for European Modeling of the Ocean implemented for the Mediterranean Region. It has an horizontal resolution of $1/16°$(around 6.7 km) and a vertical resolution of 72 unevenly spaced levels.

The coupling is done through the Ocean Atmosphere Sea Ice soil version 3 (OASIS3) coupler (Valcke, 2013). The atmosphere and ocean components communicate with a frequency of 120 minutes, when the coupler interpolates and exchanges information between the two models. Heat (radiative and turbulent fluxes), mass (evaporation, precipitation and runoff) and momentum fluxes are provided to the ocean from the atmospheric model, while the atmosphere receives the SST from the ocean model.

The model was run for 6 days in order to create a dataset suitable for the energy analysis. The outputs were analyzed for a box from 35.5625 °N to 39,1875°N and from 9.875 °W to 17.375 °W, including the area surrounding the Sicily island. Outputs were saved at the model time resolution (8 minutes).

4.2.2 Data

We examined the time series of wind over Sicily, and identified an event with wind blowing in the southwestern direction, with an intensity larger than 7 m/s. We chose the year 1052 of the simulation. The data are to be taken carefully; the model is forced with the atmospheric model output and not observations, so a simulated event may not coincide with a real event. Still, we call the simulation the realistic experiment because the configuration of the model includes more complete physics.

Figure 4.2 shows the surface temperature along the period simulated, together with the wind stress. A cold center is seen south of Sicily at the beginning of the simulation. However, the wind stress is low at this time. This is the signature of previous upwellings, since the area is often affected by upwelling-favorable winds. At the second day of simulation, a strong northwestern wind blows over the area, flowing parallel to the southern coast of Sicily. The event lasts three days, time enough to produce the upwelling. In fact, we see that a mass of cold water emerges close to the coast from days 2 to 3. The cold tongue starts to disappear when the wind ceases on the 5th day. The surface flow responds rapidly to the wind forcing, as can be seen in Figure 4.3. The surface current enters the strait and flows eastward during the first day. As soon as wind starts blowing on the second day, an Ekman current is set up to the right of the wind, and the surface current becomes southwestward. As a result, surface water is removed from the southern coast of Sicily, where an upwelling occurs.

Since the upwelling produces a cross-shore circulation, we look at the flow along a few sections south of Sicily (Figure 4.4). Figure 4.5 shows the vertical sections of temperature, zonal and meridional velocity along the cross-shore transects 2 and 5. In transect 2 (left panels), the temperature field exhibits a strong front towards the southern extreme of the transect, close to the island of Pantelleria (at 37 °N and 12 °E). This front is the limit of the cold center south of Sicily seen in Figure 4.2. The current is southward at surface, eastward close of Sicily and westward, close to Pantelleria, indicating in any case a mass transport in the offshore direction with respect to the coast of Sicily. Below the mixed layer, an eastward mass transport compensates the divergence of surface water produced at the coast. The current at the front is southward, occupying all the column depth. The circulation in transect 5 (right panels) shows the signature of the upwelling event. A temperature front is seen a few km to the coast, and subsurface waters emerge close to the coast. The motion is southwestward at surface, and opposite below surface, evidencing an offshore transport at surface and a return flow at depth. Attached to the coast, the current moves in the southeastern direction, the wind direction. The pressure differences at the front are strong enough to create a geostrophic current parallel to the front, with the low pressure on its left. The deeper part of the basin does not feel the upwelling.

The distribution of the main currents, the differences in topography and

(a) Day 1 **(b)** Day 2

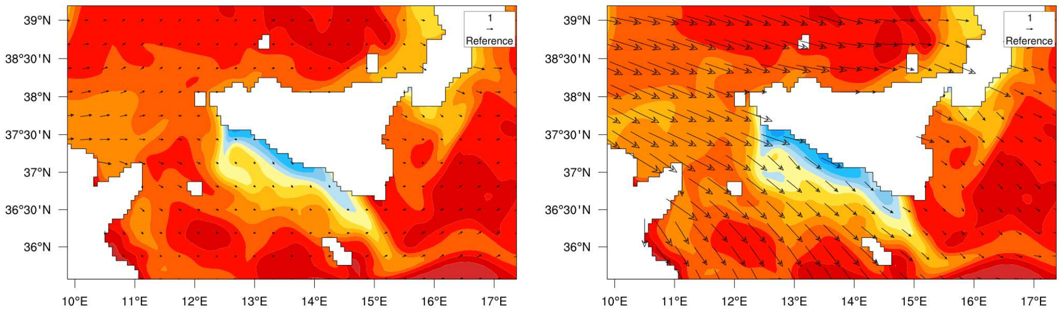

(c) Day 3 **(d)** Day 4

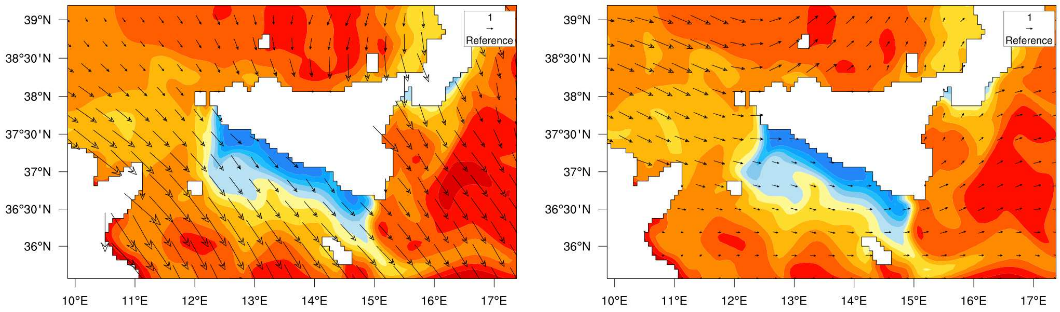

(e) Day 5 **(f)** Day 6

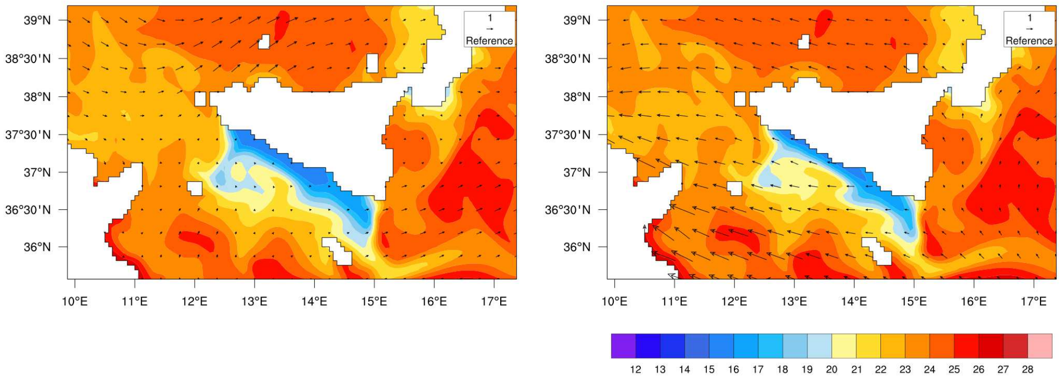

Figure 4.2: Snapshots of surface temperature (degC) and wind stress (N/m^2) at the beginning of each day of the simulation.

(a) Day 1 **(b)** Day 2

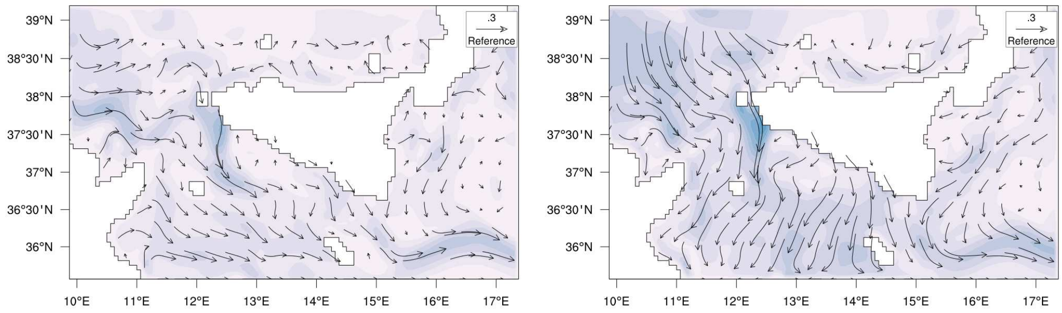

(c) Day 3 **(d)** Day 4

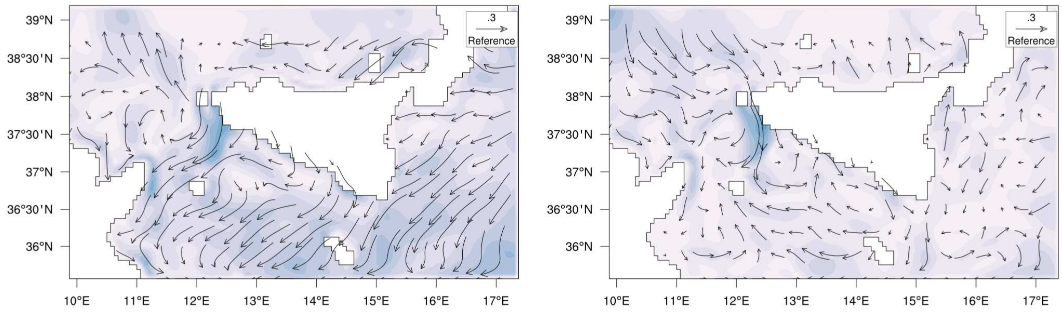

(e) Day 5 **(f)** Day 6

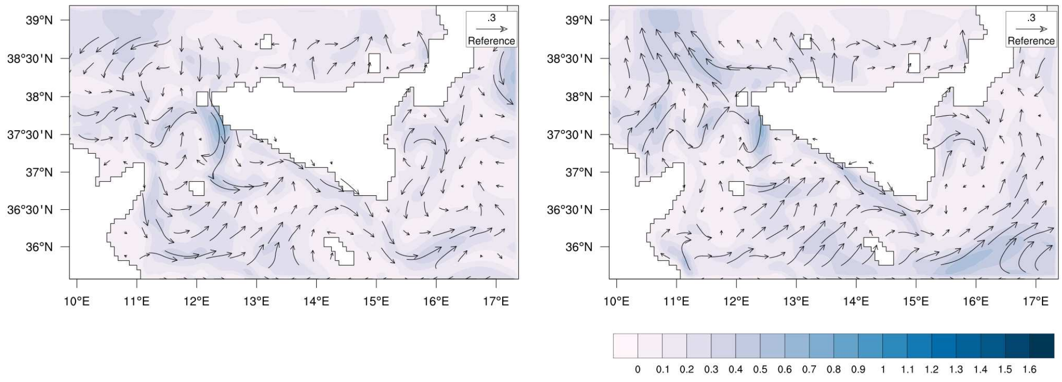

Figure 4.3: Snapshots of surface currents (m/s) at the beginning of each day of the simulation.

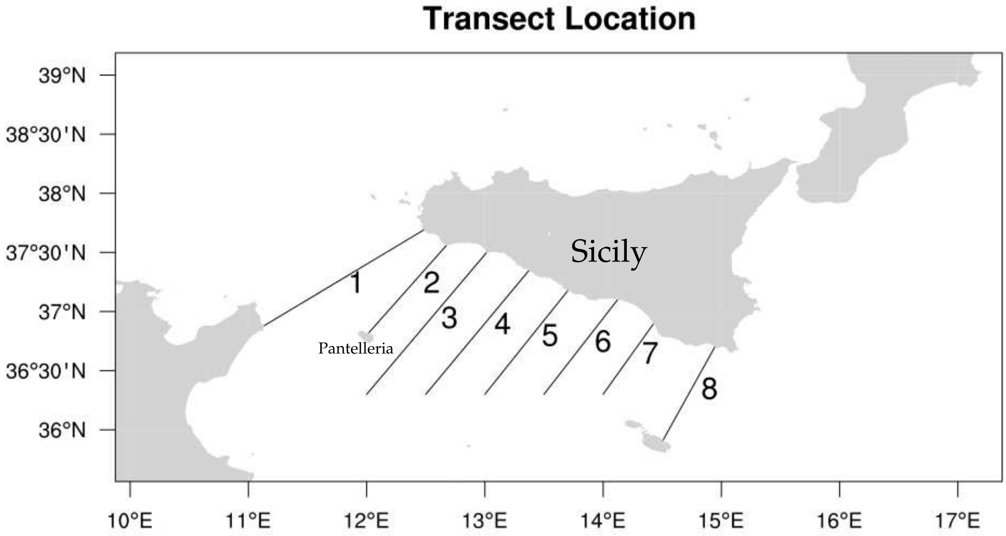

Figure 4.4: Map showing the cross-shore transects examined.

the position of the coast with respect to the wind cause the circulation along the transects to differ between them (not shown). For example, the circulation along transect 1 illustrates the exchange of water at the strait, with a surface flow moving towards the Eastern Mediterranean basin and subsurface waters exiting the strait. How the front delimiting the cold water center south of Sicily constrains the currents is seen in transect 2. Transects 5 to 8 show mainly the upwelling circulation induced by the wind event reproduced in the current simulation. The circulation along transects 3 and 4 is a combination between the front-related circulation and the upwelling circulation. We will focus mainly on transects 2 and 5, since their circulations reflect the characteristic features of the background and the upwelling circulations.

4.3 Energy analysis

In this section we show the results of the energy analysis, performed using the MS-EVA with 2 scales as in Chapter 3. The limits of the scales are $j_0 = 0$ and $j_1 = j_2 = 10$ (6.7 days and 480 seconds, the maximum resolution of the series).

Before discussing the energetics, it is useful to look at the decomposed fields. Figure 4.6 shows the surface zonal velocity, meridional velocity, and density, reconstructed in each scale. The large scale fields (left panels) give us an idea of how is the background field in the area. The large scale zonal velocity (panel

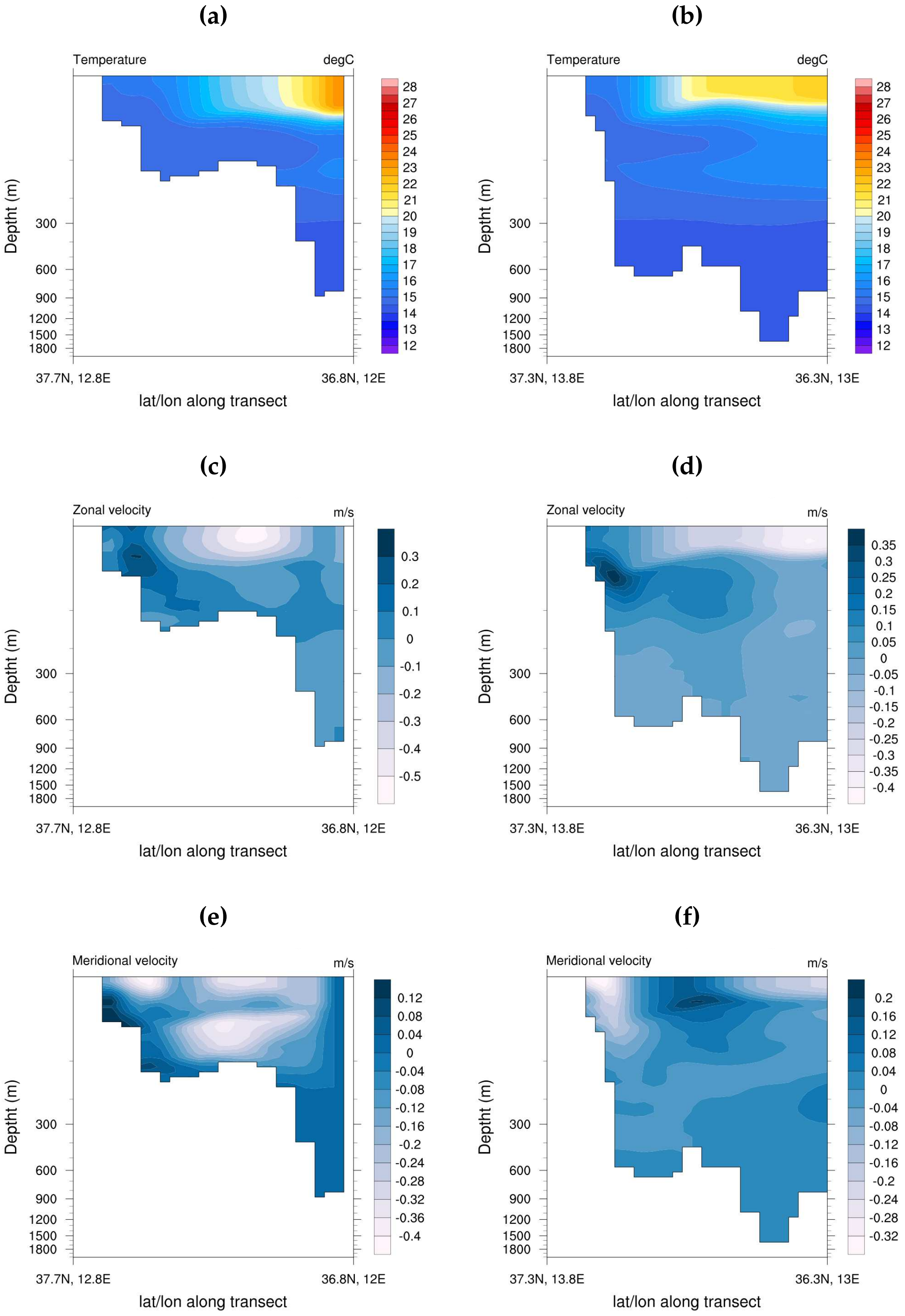

Figure 4.5: Snapshots of temperature (upper row), zonal (mid row) and meridional velocity (bottom row) along transects 2 (left) and 5 (right). The fields are at the 3rd day of simulation, when the upwelling is already active. Units are degC for temperature and m/s for velocity.

a) evidences an eastward jet that crosses the strait and flows close to the southern coast of Sicily. At the entrance of the strait and after passing Sicily, the jet forms meanders. On contrast, the mesoscale zonal velocity (panel b) is related to the instantaneous wind pattern. After the second day, the velocity becomes negative south to Sicily as a result of the Ekman transport at surface.

The large scale meridional velocity (panel c) reflects the main current, presenting negative values where the current moves southward. The mesoscale field (panel d), instead, reflects the wind event effect, showing negative values south of Sicily, corresponding to the surface southwestern Ekman transport forced by the wind.

Both the large scale (panel e) and the mesoscale (panel f) density show an upwelling signature at the southern coast of Sicily. However, the origin of these signals is different: the large scale positive anomaly seen along the coast is a consequence of past upwelling events that occurred in this area (it is present from the beginning of the simulation) while the event that we catch during the simulation is only seen in the mesoscale fields. In fact, the mesoscale density shows the positive anomaly only during the days when the upwelling is active, and dissapears towards the end of the simulation (when the wind ceases).

In light of the decomposed fields, we can say that the upwelling dynamics manifest mainly in the mesoscale energy fields, while the large scale responses to the background dynamics of the area. This is in contrast with our idealized experiment, where the upwelling signature was seen mainly on the large scale, since the circulation was fully driven by the wind.

First we look at the total kinetic energy (Figure 4.7). At the second day of simulation, a clear maximum occurs coinciding with the wind input. After this maximum, energy oscillates and decreases slowly. On the last day of simulation, energy increases because a second wind event is starting.

By decomposing both the wind stress and the surface current into their time mean and deviation components, we can infer how the energy imposed by the wind is distributed into the two scales considered (equation 3.2). The energy input by the wind to the ocean is shown in Figure 4.8. We can see that in the upwelling zone, most of the work is done by the large scale. Its value is generally positive around the coasts and at the strait of Sicily, and close to zero offshore. Three maxima are seen at the southern coast of Sicily, which are created during the windy days; otherwise the wind work is small all over the basin (not shown). This is similar to what happened in the idealized experiments in Chapter 3, where the wind input was confined to the area where the upwelling

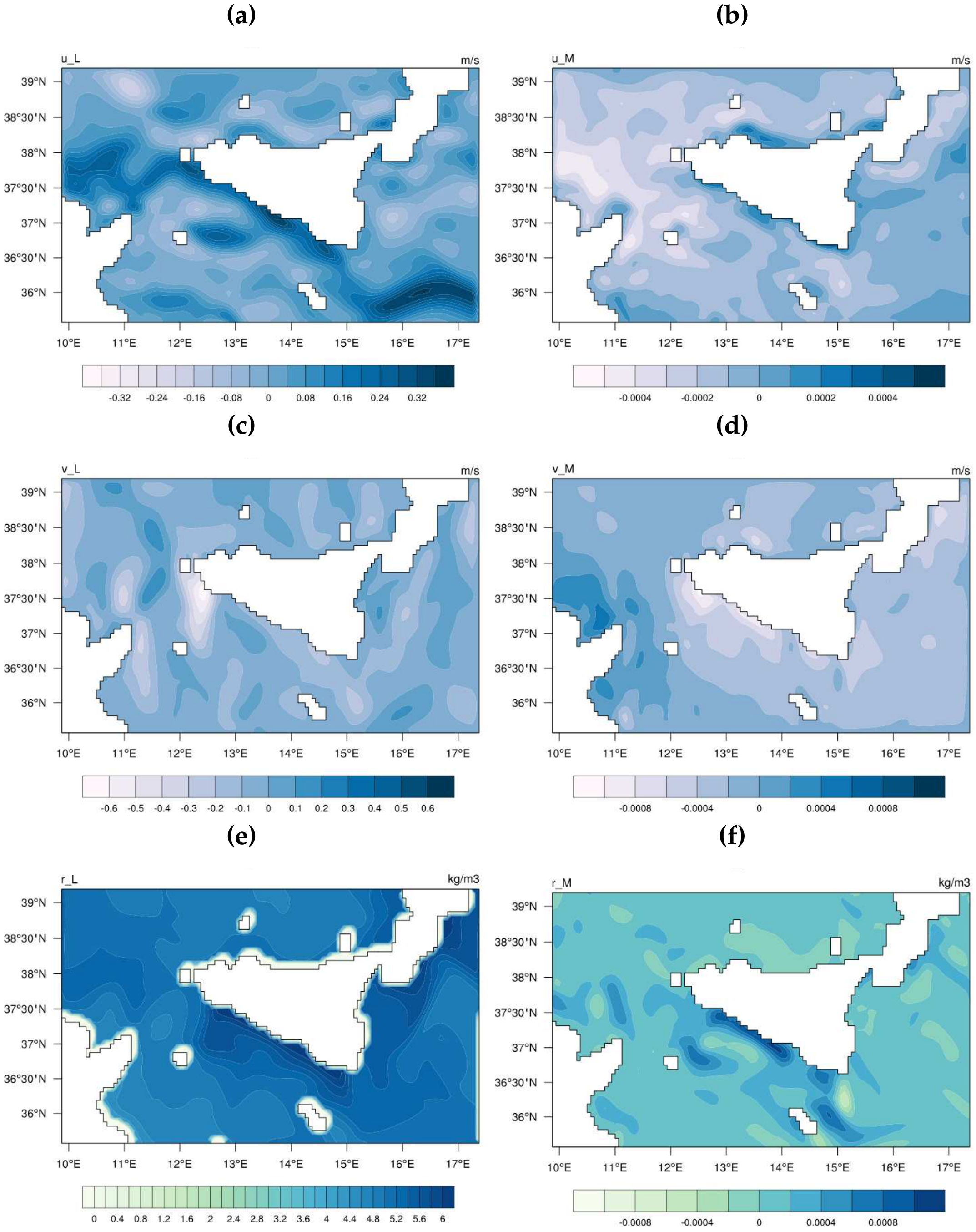
(a) (b) (c) (d) (e) (f)

Figure 4.6: Reconstructed surface fields: large scale (left) and mean mesoscale (right) reconstructed fields: zonal velocity (a, b), meridional velocity (c, d) and density anomaly (e, f). Units are m/s for the velocity and kg/m^3 for density.

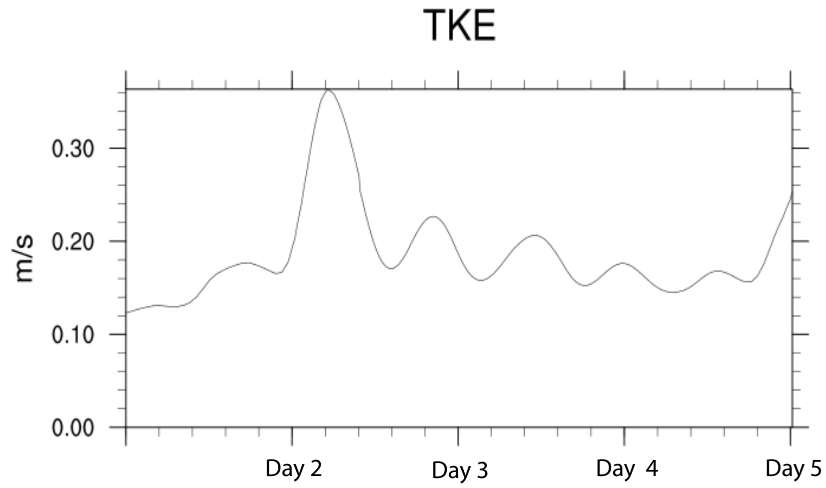

Figure 4.7: Horizontally averaged, vertically integrated Total Kinetic Energy (m^2/s^2).

was active, just a few kilometers off the coast. In that case, since the wind was homogeneous, all the work was done by the large scale fields. Here the wind is not constant any more.

The spatial patterns of the energy terms are investigated in the following. Both near surface and cross-shore transects are checked. Near surface plots help us to identify the main features of the surface circulation, while the transects give us more insight on the vertical distribution of energy related with the upwelling circulation as in Chapter 3.

The mean large and mesoscale available potential energy terms are shown at surface in Figure 4.9. We start with the large scale (left panels). The surface rate of change (panel a) indicates that the APE increases in time in all the region. Maximum values are seen at the strait, close to the capes, and along the southern coast of Sicily. The alongshore increase of APE is consistent with the idealized experiment, where APE changes were concentrated at the coastal region.

The surface lateral advection (panel b) displays positive and negative values at each side of the front, and negative values along most of the southern coast of Sicily.

The lateral advection is largely compensated by the transferences. Indeed, the spatial pattern of the transference terms (panel e) shows similar features to the lateral advection pattern, but with opposite sign. The surface panel in Figure 4.9 shows a small increase of APE all along the coast, and a region where energy is drained at the front location. This energy is in part transferred to the mesoscale (panel f).

The vertical advection (panel c) is small compared with the lateral advection and transferences. However, it is important since vertical motion is a key process in the upwelling. It is positive at surface close to the coast and slightly negative offshore, similar to the idealized experiments.

The buoyancy conversion (panel d) is also too small to contribute to the APE change, but it may be important for the KE. Buoyancy is mainly a source of large scale APE, on contrast with the idealized experiments. We can see that maximum values are connected to the frontal current between Sicily and Pantelleria. Buoyancy increases the large scale energy also along the southern coast of Sicily. Positive values of buoyancy were also seen in the idealized experiments close to the coast.

The large scale dynamics described here are closely related to the background circulation. The main feature is the region of intense energy changes between Sicily and the small island of Pantelleria. This area coincides with a front that separates the near-coast cold water, to the warmer surrounding waters. The origin of this cold water region is not the upwelling event simulated, but the fingerprint of previous upwellings that affect the area during the year. The main terms are the advection and transferences, which large values are caused by the strong current flowing parallel to the front (Figure 4.3). The large scale dynamics of points situated farther east are more related to pure upwelling dynamics. The upwelling signature is seen in the vertical advection and buoyancy conversion, which signatures close to the coast match the ones in the idealized cases. However, buoyancy conversion is a source of APE energy, rather than an input to the kinetic energy.

The mesoscale available potential energy is shown on the right panels of Figure 4.9. The surface change of mesoscale APE (panel a) is positive in all the region, specially at the southern coast of Sicily.

The lateral advection (panel b) increases the energy at surface close to the coast, while reduces it a few km from the coast. This feature was also seen in the idealized cases with topography.

The vertical advection (panel c) is negative along the southern coast of Sicily as in the idealized cases. Note also the opposite (a patch of positive vertical advection values) occurs at the northern coast, where the same wind produces downwelling.

The mesoscale buoyancy (panel d) conversion is negative close to the coast. Positive values are associated to the front at surface.

From the surface panels, it is seen that transferences (panel e) are positive close to the coast. From the interpretation of the large scale, the transferences should be positive at the front. However, this is not visible in the mean surface fields. The baroclinic conversion term (panel f) in the instantaneous fields (not shown) reveals the presence of intermittent baroclinic instabilities at the front. It is also positive along the southern coast of Sicily during the days of active upwelling.

The mesoscale energetics presented are largely in agreement with the mesoscale dynamics described in the idealized experiments. This suggests that the upwelling dynamics are dominant at short scales during our simulation.

The large and mesoscale kinetic energy terms are shown at surface in Figure 4.10. At first sight, we note that the KE content is much lower than the APE, suggesting that the energy dynamics are controlled by the APE. The large scale (left panels) kinetic energy rate of change (panel a) is negative, indicating a decrease of KE at surface, especially at the front location. Along the coast, both positive and negative values are visible, the negative values coinciding with the points where the meandering current detachs from the coast. Along the southern coast of Sicily, the reduction is not so intense but still negative values are seen at surface. This decrease of KE is in contrast with the idealized cases, which presented positive values of KE along the domain.

The vertical advection (panel c) presents a minimum at the front, while the buoyancy (panel d) pattern at surface looks similar to the vertical advection.

The pressure work terms (panels e and f), which were second order terms in the idealized simulations, are dominant here. At surface, large values are found around all the coasts, and in the area between Sicily and the northern coast of Africa, probably related to the bottom relief.

The transference term (panel g) is minimum at the southwestern part of Sicily, and negative values follow what remembers the large scale current path in Figure 4.6. Barotropic instabilities (panel h) are induced at the western part of the basin close to the coast.

The large scale KE patterns described here differ from the ones in the idealized cases. As in the large scale APE, the main features are related to the frontal region between Sicily and Pantelleria. The presence of the front and the circulation in the area control the lateral and vertical advection, as well as the buoyancy. A noticeable issue is the difference of the pressure work with respect with the idealized simulations, where it was unimportant for KE change. Nevertheless, pressure work seems to be related to the topography, as in the idealized cases.

The mesoscale fields are shown on the right panels. The rate of change of KE (panel a) increases in time, especially along the southern coast of Sicily. This increase of mesoscale KE close to the coast agrees with the idealized cases.

The upwelling signature is recognized in the vertical advection term (panel c) and buoyancy (panel d) with the exception of the frontal region. The patterns are similar to the one seen in the idealized experiment V2 (Figure 3.14 in Chapter 3), with a positive buoyancy conversion and positive vertical advection close to the coast. This is clearly seen from the surface panels.

The relative importance of the pressure work (panels e and f) is much larger than in the idealized case. Larger variations are seen in the mixed part of the column, as in the idealized case.

The transference term (panel g) shows some regions where barotropic instability occurs. The temporal variation of the barotropic conversion term (not shown) does not agree with the wind variability during the period, suggesting that the wind upwelling is not the source of barotropic instability.

Upwelling dynamics are recognized only in part in the mesoscale KE patterns. The fact that there is a background circulation, which may not depend only on the wind forcing as in the idealized experiments leads to a kinetic energy distribution that does not reflect only the upwelling dynamics. This is evident at the frontal region, where dynamics differ most from the idealized experiments.

Now we examine the energy patterns along transects 2 and 5 pictured in Figure 4.4. A careful inspection to the vertical distribution of the energy patterns of both transects allows us to set connections with the upwelling circulation described in Chapter 3, as well as to evidence the differences with the idealized experiment. Recall that the circulation in the two transects evaluated is different. The circulation in Transect 2 is mainly affected by the presence of a frontal region close to Pantelleria, the circulation along Transect 5 does reflect the signature of the reproduced upwelling event.

The mean large scale and mesoscale APE and KE are shown for transect 2 in Figure 4.11 and Figure 4.12. In general, a common feature to all the energy terms is that are magnified around the front between Sicily and Pantelleria.

In Figure 4.11, the rate of change of large scale APE (left panels, panel a) presents a maximum located offshore. The larger changes occur at the base of the mixed layer. Lateral advection (panel b) and transference terms (panel e) present a dipole, with positive and negative values at both sides of the front.

Both terms compensate between them, since the patterns are nearly opposite. Vertical advection (panel c) is positive near the coast and slightly negative offshore, as in the idealized cases. The buoyancy conversion (panel d) is positive (representing hence an increase of APE from KE) along all the column depth where the front is located.

Looking at the mesoscale APE (right panels in Figure 4.11) we can observe that the rate of change of APE (panel a) presents positive values which are confined at surface. Large changes are associated with the frontal area, where all the terms show large values at subsurface. The buoyancy (panel d) is still positive at the frontal region, but only at surface. The baroclinic term (panel f) has a maximum close to the coast.

Regarding the large scale KE (left panels in Figure 4.12), we can see that the KE rate of change is negative at surface, and positive values are only found at subsurface. This is in contrast with the idealized cases, where energy was always increasing in time. As in the APE terms, the larger values are associated to the front: lateral advection (panel b) shows a large positive patch at surface, while vertical advection and buoyancy (panels c and d) are both minimum offshore. The negative values of the buoyancy extend along all the column depth. The dominant terms are the pressure work (panels e and f), whose larger values are concentrating close to the bottom, confirming their relation with the bathymetry. The lateral and vertical pressure work nearly compensate between them.

The mesoscale energetics are represented in the right panels. In this case, the rate of change of KE (panel a) is positive in surface. Also in the mesoscale fields, the signature of the frontal region is obvious in the different terms: the distribution of the lateral (panel b) and vertical advection (panel c) is similar to the large scale patterns, while now the buoyancy (panel d) changes sign with depth. The contribution of the pressure work (panels e and f) does not concentrate at the bottom, but is diffuse along the whole column. The barotropic term (panel h) shows a positive patch close to the coast. This value is much smaller than the baroclinic term in Figure 4.11, confirming that the instabilities generated at the coast are of baroclinic nature.

The large scale and mesoscale APE terms for transect 5 are shown in Figure 4.13. We will see in the following that, opposite to transect 2 where the background state was the dominant signal in all the energy terms, the main signature along transect 5 is the one related to the upwelling.

The large scale (left panels) rate of change of APE (panel a) is positive at surface and close to the coast, as in the idealized cases. The energy terms peak close to the coast, either at surface, or at the base of the mixed layer. The vertical advection (panel c) is positive at the coast and negative just below, as in the idealized case. The buoyancy is positive close to the coast, indicating a conversion from KE to APE in this region, and opposite to the idelialized cases, where the conversion was mainly from APE to KE. Lateral advection (panel b) and transferences (panel e) nearly equilibrate each other, and present a dipole of positive and negative values at the base of the mixed layer. This feature was also seen in the idealized cases.

The mesocale APE is shown on the right panels. The rate of change is positive at surface. Lateral advection (panel b) and transferences (panel e) increase the energy close to the coast. Negative values of vertical advection (panel c) and buoyancy conversion (panel d) are seen close to the coast, in accordance with the idealized cases. The baroclinic term (panel f) indicates the presence of baroclinic instabilities at the coastal area.

The last figure that we will comment is Figure 4.13, which shows the large scale and mesoscale mean KE terms along transect 5. The large scale (left panels) rate of change of KE (panel a) shows a series of maxima and minima at surface. We can see that the lateral advection (panel b) and the transfer term (panel g) present a maximum at surface close to the coast and a minimum below. Negative values of vertical advection (panel c) occur close to the coast, consistent to what happened in the idealized cases. Also the buoyancy conversion (panel d) is negative here, but in this case the path extends deeper. The pressure work (panels e and f) presents large values close to the topography, with opposite signs in the lateral and vertical directions.

The mesoscale (right panels) KE rate of change (panel a) is positive at surface and maximum close to the coast. The increase of energy close to the coast agrees with the idealized cases. The upwelling signature is recognized in the vertical advection (panel c) and buoyancy (panel d) terms, with positive values close to coast and negative values below. The pressure work (panels e and f) contribution is concentrated in the mix layer. The barotropic term (panel h) does not indicate a clear source of instabilities.

4.4 Summary and discussion

In this chapter, we explored the energy dynamics of a realistic experiment in the Mediterranean Sea. The so called *realistic experiment* was done using a state of the art atmospheric and ocean coupled model. The model was run for a period of 6 days, where an upwelling-favorable wind was blowing over the region of Sicily. The basic upwelling mechanism is set up immediately: the wind forces a surface current that is deflected to the right of the wind by Coriolis, and cold water is brought to the surface close to the coast. The upward motion of water at the southern coast of Sicily generates a cold tongue close to the coast that is seen during three days. This signature is superposed to a background state where a cold pool of water occupies the southern coast of Sicily, and a mean eastward flow.

The existence of a background state complicates the interpretation of the energy dynamics. The energy input by the wind to the ocean modifies the background state by affecting the circulation and the stratification. Local processes redistribute the energy, or convert it between the two types of energy and the different scales. By looking at the spatial patterns of energy, we tried to differentiate which features could be attributed to the upwelling. To do it, we used the knowledge gained trough the study of the idealized experiments.

The large scale dynamics depicted by the energy analysis are a consequence of the background circulation. A conspicuous feature is seen in all large scale and mesoscale APE and KE at the western end of Sicily. At this point, the current entering the strait encounters the land, and is deflected southward. The current flows parallel to a density front that separates the cold water pool south of Sicily to the surrounding areas, and then meanders while moving to the East. Strong energy advection and transferences are associated with the current at the frontal area, but not only. Also the vertical advection and buoyancy fields present minimum values in this region. The frontal region is a source of both baroclinic and barotropic instabilities. The energy fields in this region do not reflect the upwelling dynamics, but the main circulation there. This is seen in both surface figures and the transects analyzed. Among the two transects analyzed, the importance of the background state is evident particularly in transect 2, where little traces from the idealized experiments can be found, suggesting that it is the background state and not the upwelling dynamics the dominating factor here.

The upwelling signature is seen mostly in the APE fields, particularly in the mesoscale fields, along the southern coast of Sicily. It was indeed transect 5 the one showing more similarities to the idealized cases. The observed alongshore increase of APE is consistent with the idealized experiment, where APE changes were concentrated at the coastal region. The energy is redistributed by the advection terms, while buoyancy is a source of KE. Vertical advection is the best indicator of the upwelling. Baroclinic transferences occur during the upwelling period. While the APE fields are in general agreement with the ones described in the idealized upwelling, the upwelling dynamics are not easily recognized in the KE fields. The background field dominates the dynamics in both large scale and mesoscale, and the main signals are generally the ones at the front. Transfer terms lead to barotropic instabilities at the western end of Sicily. However, the barotropic term does not vary as the wind forcing, suggesting that it is not related to the upwelling.

The divergences of the realistic simulation with respect to the realistic experiment were expected: the physics contained in the idealized simulations were much more simplified, and the circulation was fully forced by the wind. As a result, the background state in the idealized experiment can only reflect the wind driven dynamics, which dominate in the large scale. On the contrary, the circulation in the realistic simulation is the consequence of a number of factors as atmospheric heat and mass fluxes, atmospheric pressure loading, or remote forcing signals carried out by waves, that were not considered in the idealized experiments. All these processes interact and add complexity to the signal, and generate a background state that is far from purely wind driven. Furthermore, the realistic experiment contains variations in both the meridional and zonal directions, while in the idealized experiment latitudinal variations were not considered.

In spite of all, part of the upwelling dynamics are reflected in the energy fields, suggesting that, when active, the circulation induced by the upwelling dominates. This is an advantage of the methodology, that can detect features of the energy evolution inherent to the physical process despite the presence of a background circulation.

The role of the background circulation is highlighted here as the main cause for the differences between the realistic and the idealized experiments. However, there are lot of opened questions, and a deeper analysis would be necessary in order to fully understand the impact of the background circulation. At this respect, looking for different upwelling events with different background states would be useful to disentangle their contribution. This issue may be the center of future work.

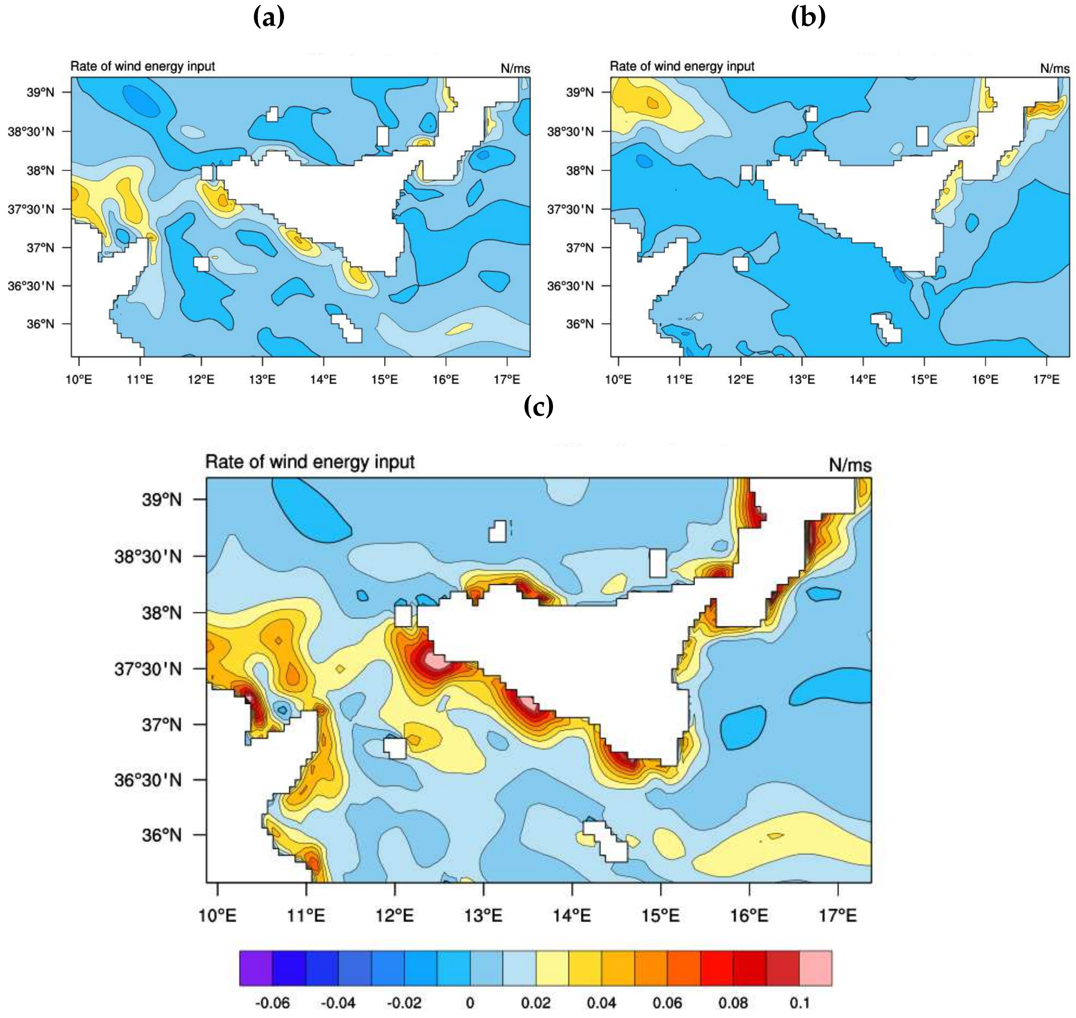

Figure 4.8: Wind work (N/ms) averaged along the simulation time: wind work to the mean flow (a) and wind work to the deviation flow (b) and total wind work (c).

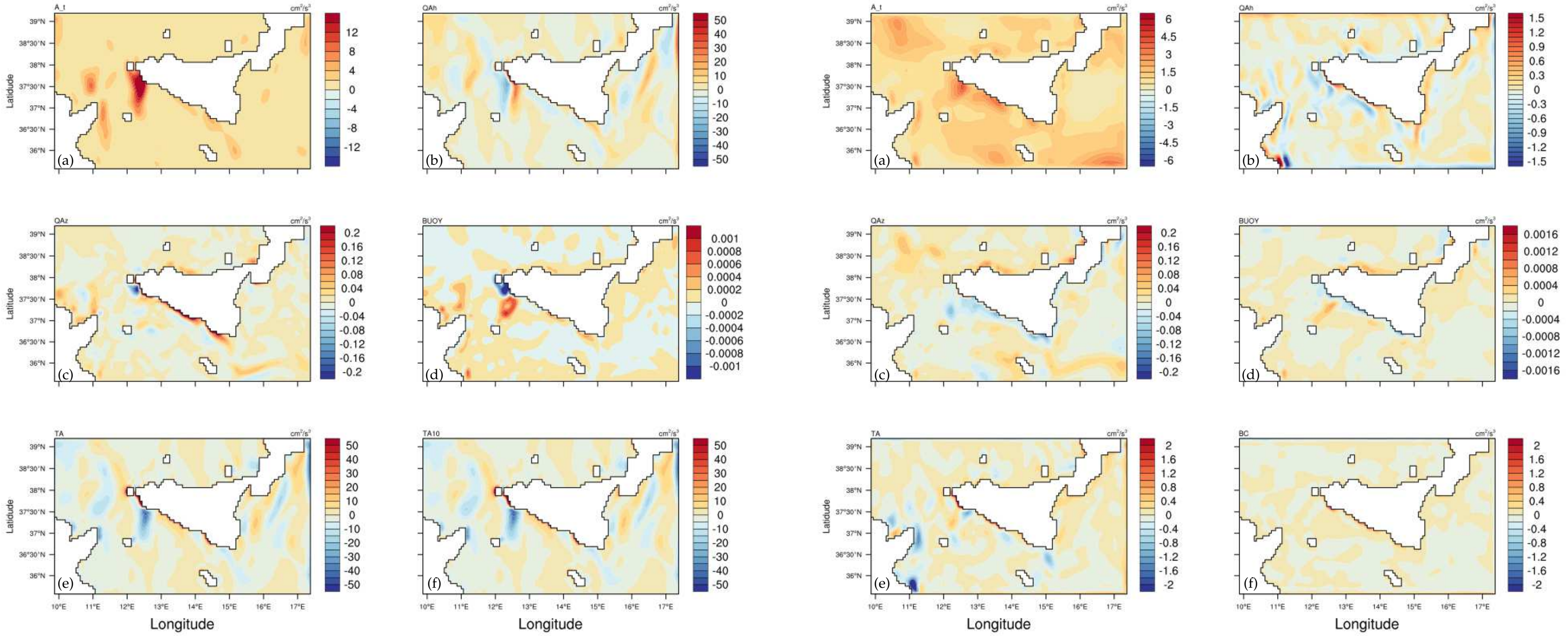

(a) Large scale.

(b) Meso scale.

Figure 4.9: Mean APE terms (m^2/s^3) for the realistic experiment at 4.6 m depth. Terms in each panel are the time rate of change of available potential energy (a), horizontal (b) and vertical (c) advection of energy, buoyancy conversion (d), total transference term (e) and large-mesoscale transference (f), which in the case of the mesoscale is the Baroclinic Term (f in right panel).

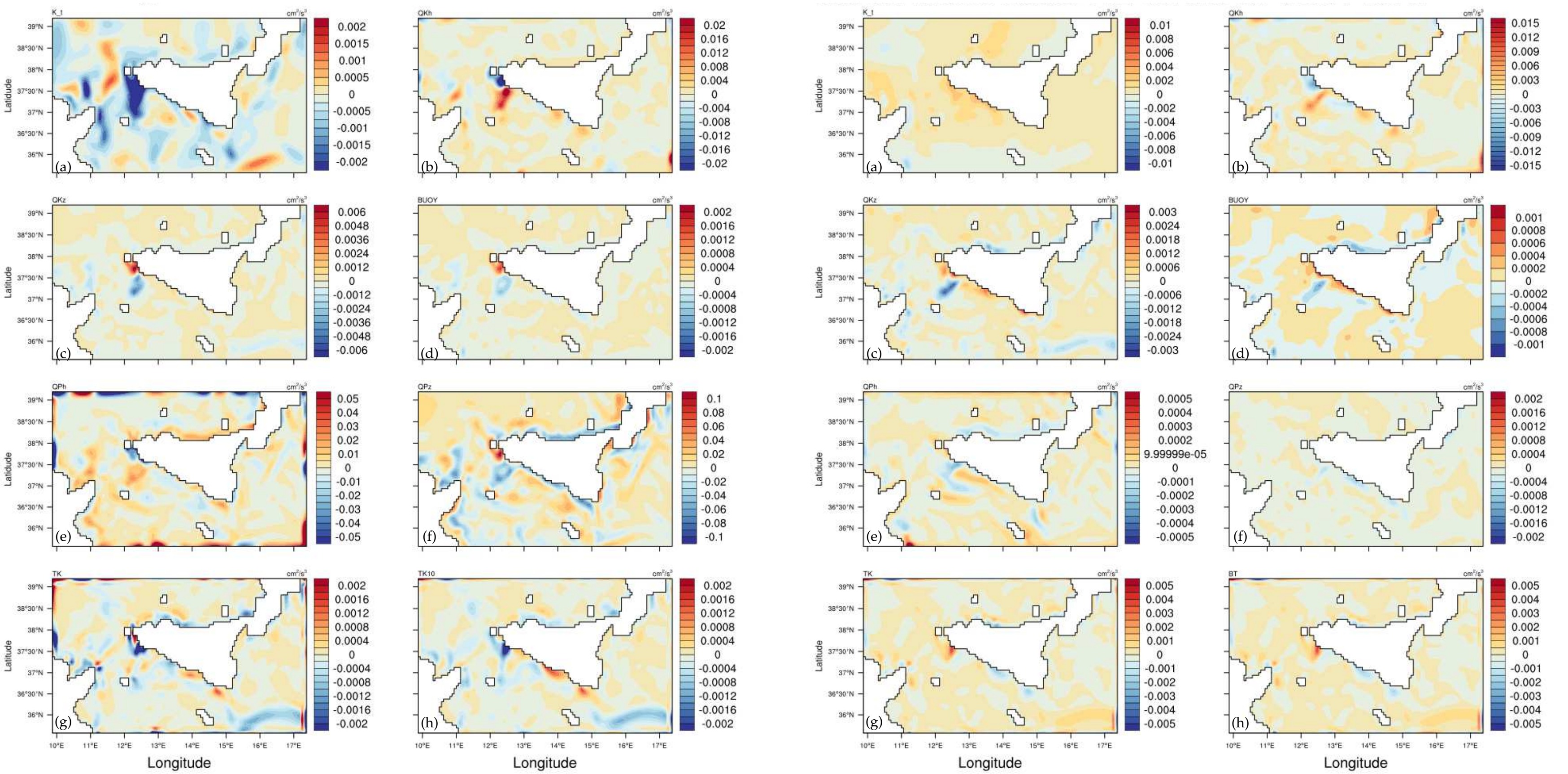

(a) Large scale

(b) Meso scale

Figure 4.10: Mean KE terms (m^2/s^3) for the realistic experiment at 4.6 m depth. Terms in each panel are the time rate of change of kinetic energy (a), horizontal (b) and vertical (c) advection of energy, buoyancy conversion (d), horizontal (e) and vertical (f) pressure work, total transference term (g) and large-mesoscale transference (h), which in the case of the mesoscale is the Barotropic Term (h in right panel).

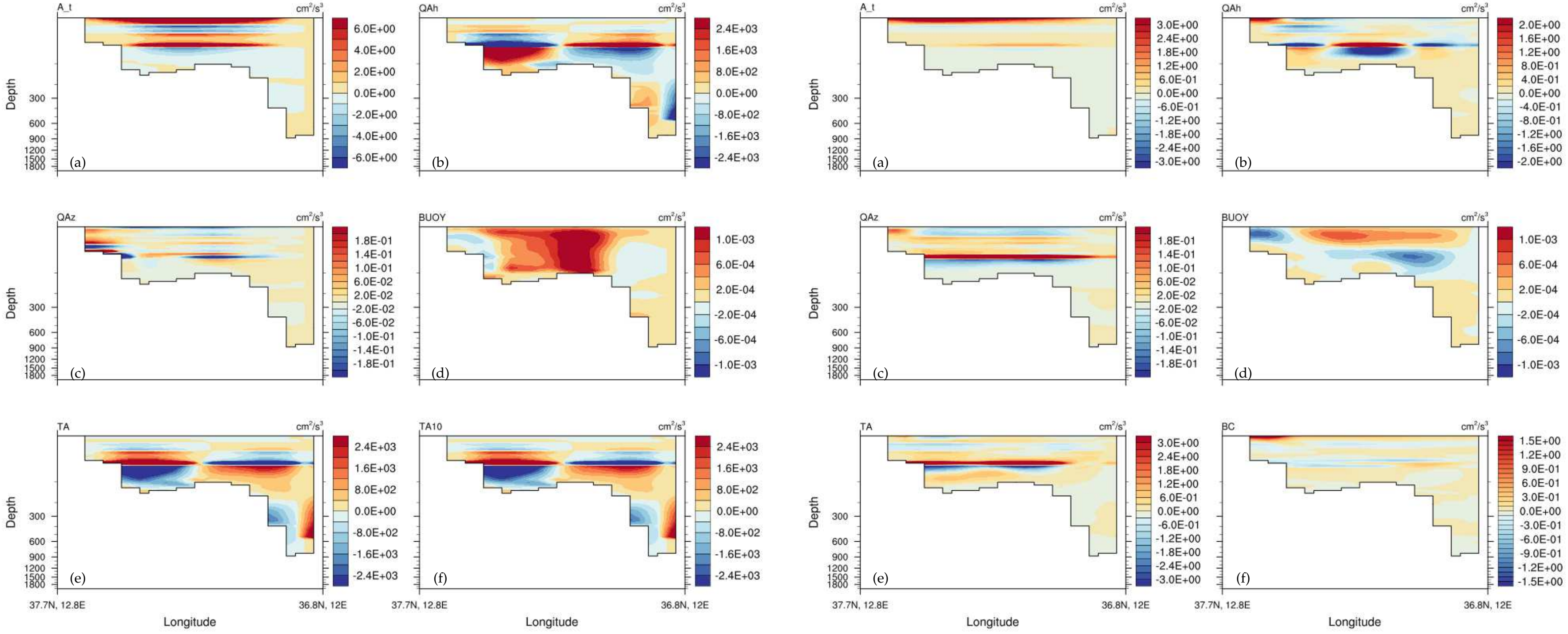

(a) Large scale.

(b) Meso scale.

Figure 4.11: Mean APE terms (m^2/s^3) for the realistic experiment along transect 2. Terms in each panel are the time rate of change of available potential energy (a), horizontal (b) and vertical (c) advection of energy, buoyancy conversion (d), total transference term (e) and large-mesoscale transference (f), which in the case of the mesoscale is the Baroclinic Term (f in right panel).

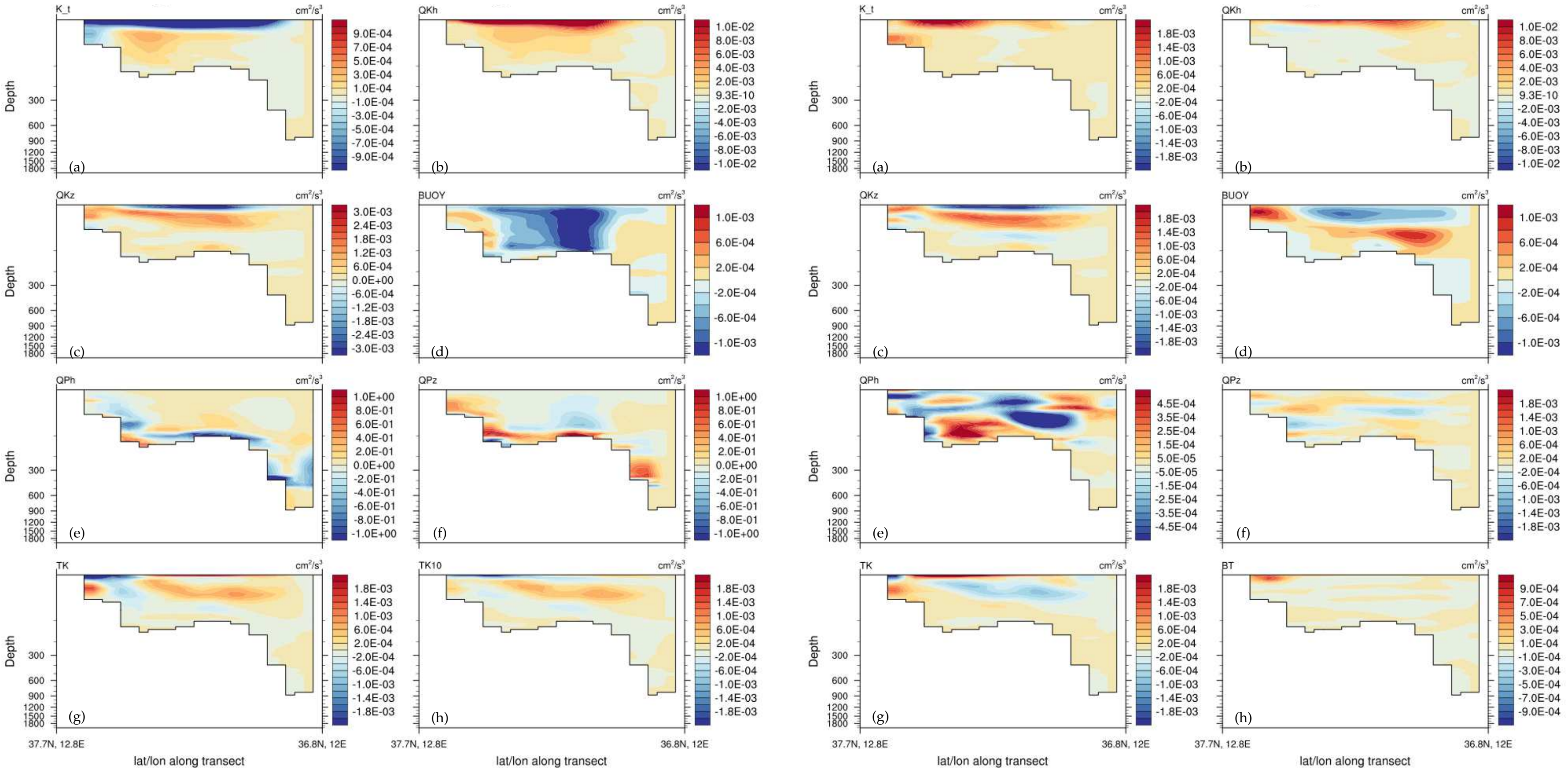

(a) Large scale

(b) Meso scale

Figure 4.12: Mean KE terms (m^2/s^3) for the realistic experiment along transect 2. Terms in each panel are the time rate of change of kinetic energy (a), horizontal (b) and vertical (c) advection of energy, buoyancy conversion (d), horizontal (e) and vertical (f) pressure work, total transference term (g) and large-mesoscale transference (h), which in the case of the mesoscale is the Barotropic Term (h in right panel).

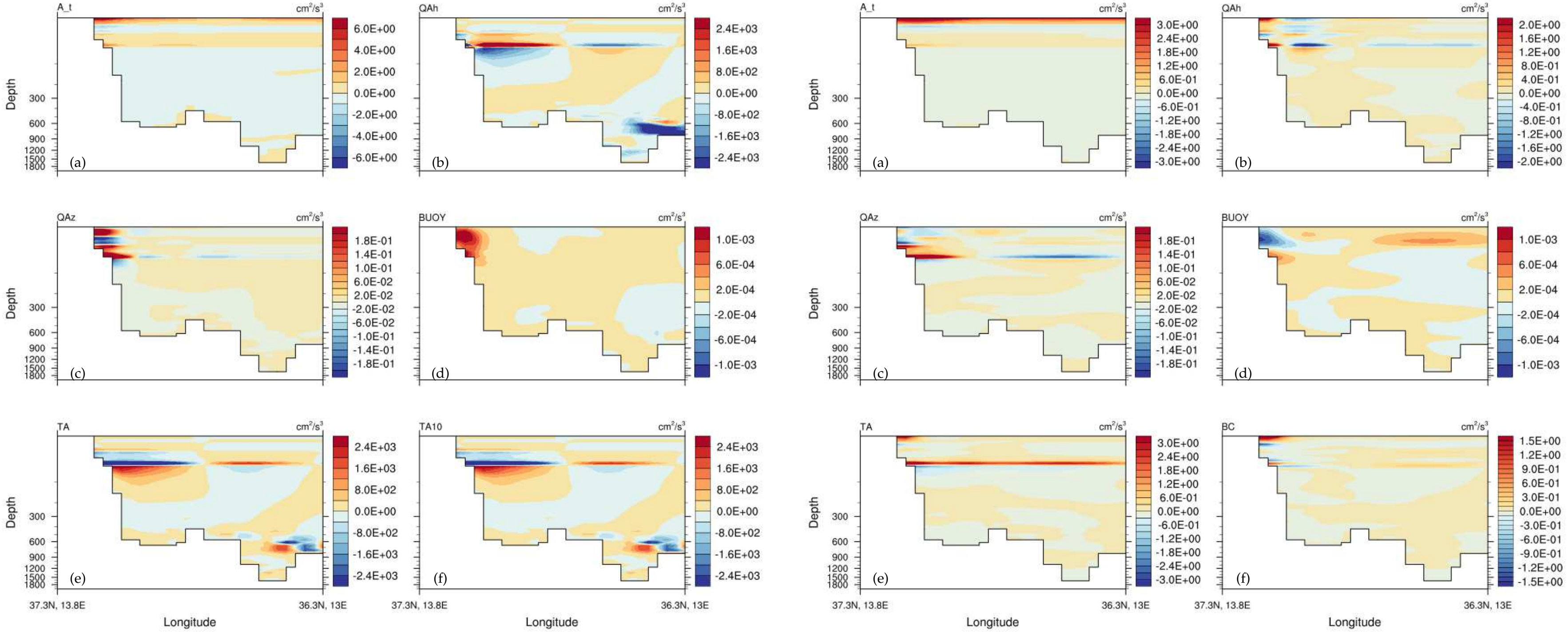

(a) Large scale.

(b) Meso scale.

Figure 4.13: Mean APE terms (m^2/s^3) for the realistic experiment along transect 5. Terms in each panel are the time rate of change of available potential energy (a), horizontal (b) and vertical (c) advection of energy, buoyancy conversion (d), total transference term (e) and large-mesoscale transference (f), which in the case of the mesoscale is the Baroclinic Term (f in right panel).

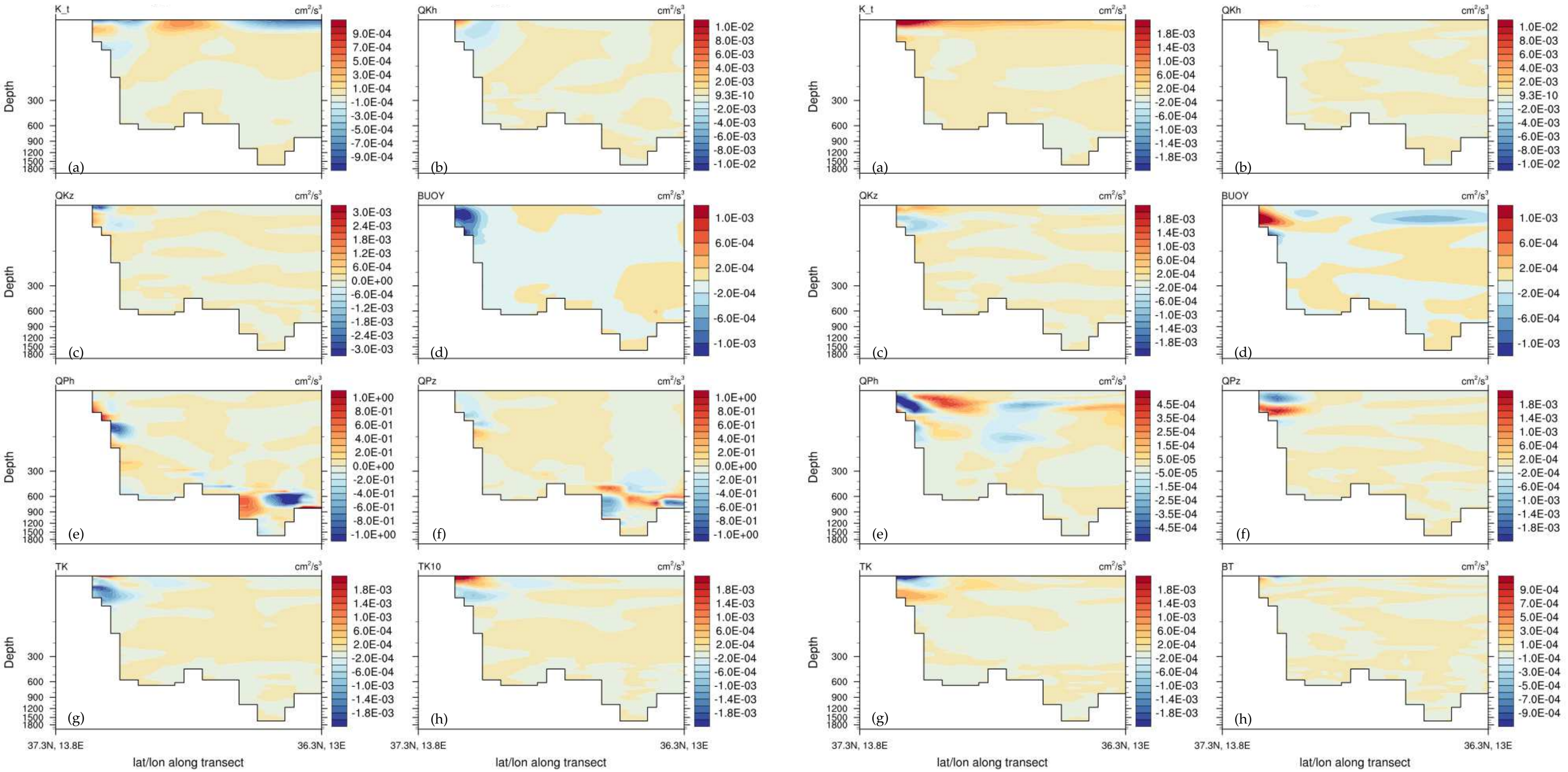

(a) Large scale

(b) Meso scale

Figure 4.14: Mean KE terms (m^2/s^3) for the realistic experiment along transect 5. Terms in each panel are the time rate of change of kinetic energy (a), horizontal (b) and vertical (c) advection of energy, buoyancy conversion (d), horizontal (e) and vertical (f) pressure work, total transference term (g) and large-mesoscale transference (h), which in the case of the mesoscale is the Barotropic Term (h in right panel).

Conclusions

In this work we use local energy analysis to unravel the dynamics of coastal upwelling. The first chapter was devoted to the review of existing methods for field decomposition used in energy analysis. We compared the strong and weak points of Reynolds-like decomposition and spectral methods based on Fourier and wavelet transforms. Among the methods presented the one we used in this thesis is called Multi Scale Energy and Vorticity Analysis (MS-EVA). It provides a localized decomposition of the energy in scales, which is particularly suitable for the study of processes that are heterogeneous in space and non stationary, as most of the geophysical problems. The widely used Reynolds-like decomposition is used complementary to validate the methodology.

The first step in our energy analysis was to validate the methodology. To this aim, we made use of the Eady model, an analytical model reproducing pure baroclinic instabilities, to demonstrate the effectiveness of the MS-EVA. We produced a dataset and performed a two scale energy analysis. Under these conditions, MS-EVA is analogous to the Reynolds decomposition, so we checked that both types of analysis were in agreement. MS-EVA revealed the mechanism producing the growing perturbation as a pure baroclinic instability, as expected. The perturbation grows at the expense of mean Available Potential Energy extracted from the mean stratification. Part of this energy is converted to Kinetic Energy, and part is simply redistributed along the domain by the mean flow. The method was also successful when tested on a second case with a non growing instability, and when compared with the Reynolds-like analysis.

After the validation, we performed a set of idealized experiments that allowed us to investigate the dynamics of a simple upwelling under controlled conditions. We built three experiments with different topographies, and carried out numerical simulations with the ocean model NEMO. The physics of the experiments were greatly simplified by excluding horizontal friction, and reducing the forcing to a constant, homogeneous wind. The results were compared with an analytical model reproducing the exact solutions of wind-driven upwelling in order to ensure the consistency. A typical upwelling circulation was generated in each of the experiments: the wind induces offshore Ekman transport generating divergence close to the coast that lead to upward motion. A geostrophic alongshore current compensates the pressure differences formed between the coast and offshore regions. The energy analysis revealed the main path of energy related to this type of circulation. The wind work puts in motion the current, which increases the Kinetic Energy. As water moves, the background stratification is modified and Available Potential Energy is released. Part of this energy is converted to Kinetic energy. Energy is also transferred to smaller scales via both Baroclinic and Barotropic instabilities. Although the basic mechanism is the same for all the idealized simulations, the topography experiments presented some differences. The presence of a topography modifies the circulation. The flow is intensified close to the coast, and in some case secondary circulation structures are formed. These changes affect in fact the energy distribution, producing more energetic features close to the coast and benefiting the formation of coastal instabilities. In the idealized experiments, the energy is inputed to the large scale, and the upwelling signature is visible mainly in the large scale fields. This is because the circulation is completely wind driven, and there is no other process forcing the motion.

The last experiment was done using a high-resolution state of the art coupled model (COSMO-NEMO-MFS-OASIS3), configured for the Mediterranean Region. We used the coupled model to make an energy scale analysis in the case of an upwelling under realistic conditions. The region studied was the southern coast of Sicily, where upwelling is a common phenomenon. An upwelling-favorable wind pulse lasting 3 days was enough to generate the upwelling. The background state showed the signature of previous upwelling events, and exhibited a main eastward circulation. The upwelling circulation was set up immediately after the wind pulse, superposing to the background state. A cold tongue developed close to the coast, and the surface current turned to the right of the wind.

The energy analysis of the realistic experiment showed some common features with respect to the idealized experiments. The upwelling-induced circulation generated an increase of the Available Potential Energy, with only part of this energy being converted to Kinetic Energy. The energy was redistributed by advection and transferences, and the flow was baroclinically unstable. Barotropic instabilities were present along the coast, but could not be related to the upwelling. However, in the realistic experiment, the signal of the upwelling is mostly found in the mesoscale, instead of the large scale as in the idealized case. In a more complex framework, where many forces apart from the wind interact to create a background circulation, the large scale dynamics are related to this background state, rather than to the upwelling dynamics. The upwelling signal is therefore associated to the smaller scales, where it can be recovered. Further work is necessary to unravel the role of the background circulation, that has to be left for the future.

With this thesis, we demonstrated the potentiality of a relatively unused methodology, the MS-EVA, in the study of oceanic processes. It can be used as diagnostic instrument for assessing the capability of numerical models in reproducing specific physical processes, while it has proved to be useful for unraveling the basic mechanisms underpinning oceanic processes. We adressed a simple problem, a coastal upwelling, which is well known and ubiquitous in the ocean, but a great number of processes are suitable for the study with MS-EVA. Basically any process involving different scales, where the basic state is not stationary but evolving in time can be analyzed with this instrument: the evolution of jets, meanders and eddies are all good examples for the application of the methodology. Further developments can involve also the atmospheric processes, as the methods has been recently adapted to the atmosphere equations (San Liang, 2016).

Appendix A

Multi scale energy equations

This appendix contains the derivation of the equations governing the multiscale energy evolution, following Liang (2002); Liang and Robinson (2005, 2007). We start from the primitive equations under the Boussinesq and hydrostatic approximations. They can be expressed in its vector invariant form as:

$$\frac{\partial \mathbf{v}}{\partial t} = -\nabla\cdot(\mathbf{v}\cdot\mathbf{v}) - w\frac{\partial \mathbf{v}}{\partial z} - f\mathbf{k}\times\mathbf{v} - \frac{1}{\rho_0}\nabla P + \mathbf{F_{mh}} + F_{mv} \tag{A.1a}$$

$$\nabla\mathbf{v} + \frac{\partial w}{\partial z} = 0 \tag{A.1b}$$

$$\frac{\partial P}{\partial z} = -\rho g \tag{A.1c}$$

$$\frac{\partial \rho}{\partial t} = -\nabla\cdot(\mathbf{v}\rho) - w\frac{\partial \rho}{\partial z} + w\frac{N^2\rho_0}{g} + F_{\rho h} + F_{\rho v} \tag{A.1d}$$

where $\mathbf{v} = (u, v)$ is the horizontal velocity vector; w the vertical velocity; ∇ the horizontal gradient operator; $f = 2\Omega sin\phi$ the Coriolis term, with Ω the constant Earth rotation rate; $F^{mh}, F^{mv}, F^{\rho h}, F^{\rho v}$ the horizontal and vertical eddy viscosity and diffusion coefficients.

$N^2 = -\frac{g}{\rho_0}\frac{\partial \bar{\rho}}{\partial z}$ is the buoyancy frequency, with $\bar{\rho} = \rho(z)$ being the stationary density profile. ρ is the density perturbation (to which the $\rho(z)$ has been subtracted), ρ_0 the reference density, and P is the dynamic pressure [1].

In order to examine the energy budget, we make the separation of the fields into scales by applying the multi scale window transform. The large-, meso- and submeso- scale energy equations derived from the PE equations are shown here. The scales (or windows) are indicated by $S = 0, 1, 2$ (the large, meso and

---

[1] The pressure associated to a fluid in motion. It is a form of kinetic energy, indeed)

submeso scales respectively). Generally, for each scale, the procedure is the following:

(I) Apply the Multi Window Transform (in Chapter 1).

(II) Take dot product with $\hat{\mathbf{v}}_n^{\sim S}$ in the case of the KE equation, and with $\frac{g^2}{\rho_0^2 N^2}\hat{\rho}_n^{\sim S}$ in the APE equation. Manipulate the equations to obtain physical meaningful terms. All the terms must be multiplied by 2^{j_2} before being physically interpreted. The factor 2^{j_2} is necessary to ensure the conservation of energy when applying the transform. It is omitted in the equations for simplicity.

Evolution of Kinetic Energy

The kinetic energy on each window S and location n is defined as:

$$K_n^S = 2^{j_2}\left[\frac{1}{2}\hat{\mathbf{v}}_n^{\sim S}\cdot\hat{\mathbf{v}}_n^{\sim S}\right] \tag{A.2}$$

By taking dot product of the momentum equation with $\hat{v}_n^{\sim S}$ and applying the MWT, we can obtain the evolution of the kinetic energy.

$$\begin{aligned}\overbrace{\hat{\delta}_n K^S}^{\text{Time rate of change of mesoscale KE}} &= \overbrace{\underbrace{\Delta_h Q_{K_n^S} + \Delta_z Q_{K_n^S}}_{\text{Transport}} + \underbrace{T_{K_n^S,h} + T_{K_n^S,z}}_{\text{Transfer}}}^{\text{Advection terms}} + \overbrace{\underbrace{\Delta_h Q_{P_n^S} + \Delta_z Q_{P_n^S}}_{\text{Pressure terms}} - \underbrace{b_n^S}_{\text{Buoyancy}}}^{\text{Pressure terms}} \\ &\quad \overbrace{+\mathbf{F}^S{}_{n,mh} + F^S_{n,mv}}^{\text{Friction terms}}\end{aligned} \tag{A.3}$$

Single terms

a) Temporal rate of change [2]

$$\hat{\mathbf{v}}_n^{\sim S}\cdot[\hat{\delta}_n\hat{\mathbf{v}}_n^{\sim S}] = \hat{\delta}_n K_n^S - (\Delta t)^2(\hat{\delta}_n^2\hat{\mathbf{v}}_n^{\sim S}\cdot\hat{\delta}_n\hat{\mathbf{v}}_n^{\sim S})$$

---

[2] The time rate of change is computed in a way similar to finite differences:

$$\hat{\delta}_n K^S = \frac{1}{2\Delta t}\left(\frac{1}{2}\hat{\mathbf{v}}_n^{\sim S}\cdot\hat{\mathbf{v}}_n^{\sim S}\right); \quad \hat{\delta}_n\hat{v}_n^{\sim S} = \frac{\hat{\mathbf{v}}_{n+}^{\sim S} - \hat{\mathbf{v}}_{n-}^{\sim S}}{2\Delta t}; \quad \hat{\delta}_n^2\hat{v}_n^{\sim S} = \frac{\hat{\mathbf{v}}_{n+}^{\sim S} + 2\hat{\mathbf{v}}_n^{\sim S} - \hat{\mathbf{v}}_{n-}^{\sim S}}{(\Delta t)^2}$$

b) Advection terms:

The advection terms in (A.3) generate the transport term and transfer terms in both the horizontal and vertical directions. Each transport/transfer term is divided has a contribution in each direction, indicated with the subindexes x, y, z, or h, standing for "horizontal". Schematically:

$$\text{TRANSPORTS} = \Delta_h Q_{K_n^S} + \Delta_z Q_{K_n^S} = \Delta_x Q_{K_n^S} + \Delta_y Q_{K_n^S} + \Delta_z Q_{K_n^S}$$

$$\text{TRANSFERS} = T_{K_n^S,h} + T_{K_n^S,z} = T_{K_n^S,x} + T_{K_n^S,y} + T_{K_n^S,z}$$

Where:

$$\Delta_x Q_{K_n^S} = -\frac{\partial}{\partial x}\left[\frac{1}{2}\hat{u}_n^{\sim S}\cdot\widehat{(uu)}_n^{\sim S} + \frac{1}{2}\hat{v}_n^{\sim S}\cdot\widehat{(uv)}_n^{\sim S}\right]$$

$$\Delta_y Q_{K_n^S} = -\frac{\partial}{\partial y}\left[\frac{1}{2}\hat{u}_n^{\sim S}\cdot\widehat{(vu)}_n^{\sim S} + \frac{1}{2}\hat{v}_n^{\sim S}\cdot\widehat{(vv)}_n^{\sim S}\right]$$

$$\Delta_z Q_{K_n^S} = -\frac{\partial}{\partial z}\left[\frac{1}{2}\hat{u}_n^{\sim S}\cdot\widehat{(wu)}_n^{\sim S} + \frac{1}{2}\hat{v}_n^{\sim S}\cdot\widehat{(wv)}_n^{\sim S} + \frac{1}{2}\hat{w}_n^{\sim S}\cdot\widehat{(ww)}_n^{\sim S}\right]$$

$$T_{K_n^S,x} = -\hat{u}_n^{\sim S}\cdot\frac{\partial}{\partial x}\widehat{(uu)}_n^{\sim S} - \hat{v}_n^{\sim S}\cdot\frac{\partial}{\partial x}\widehat{(uv)}_n^{\sim S} + \Delta_x Q_{K_n^S} - \hat{K}_n^{\sim S}\frac{\partial}{\partial x}u_n^{\sim S}$$

$$T_{K_n^S,y} = -\hat{u}_n^{\sim S}\cdot\frac{\partial}{\partial y}\widehat{(vu)}_n^{\sim S} - \hat{v}_n^{\sim S}\cdot\frac{\partial}{\partial y}\widehat{(vv)}_n^{\sim S} + \Delta_y Q_{K_n^S} - \hat{K}_n^{\sim S}\frac{\partial}{\partial y}v_n^{\sim S}$$

$$T_{K_n^S,z} = -\hat{u}_n^{\sim S}\cdot\frac{\partial}{\partial z}\widehat{(wu)}_n^{\sim S} - \hat{v}_n^{\sim S}\cdot\frac{\partial}{\partial z}\widehat{(wv)}_n^{\sim S} - \hat{w}_n^{\sim S}\cdot\frac{\partial}{\partial z}\widehat{(ww)}_n^{\sim S} + \Delta_z Q_{K_n^S} - \hat{K}_n^{\sim S}\frac{\partial w_n^{\sim S}}{\partial z}$$

Note that the window transform of the product between two variables (let's say p, q) is:

$$\widehat{(pq)}_n^{\sim S} = \int_0^{\varrho}\sum_{i=0}^{1}\sum_{j=0}^{1}(\hat{p}^i\hat{q}^j)\phi_n^{j_2,\varrho}(t)dt$$

So each product is actually the sum of all the possible combinations between scales. Interaction between 2 windows is obtained by summing only the interaction terms we are interested in. For example, the Barotropic Instability term is the horizontal transferences of KE, considering only the mixed terms between scales 0 and 1.

$$BT = T_{K_n^S,h}^{0\to 1}$$

c) Pressure terms: pressure work and buoyancy conversion

$$\text{PRESSURE TERMS} = \Delta_h Q_{P_n^S} + \Delta_z Q_{P_n^S} + b_n^S = \Delta_x Q_{P_n^S} + \Delta_y Q_{P_n^S} + \Delta_z Q_{P_n^S} + b_n^S$$

$$\Delta_x Q_{P_n^S} = -\frac{1}{\rho_0}\frac{\partial}{\partial x}\left(\hat{u}_n^{\sim S}\hat{p}_n^{\sim S}\right)$$

$$\Delta_y Q_{P_n^S} = -\frac{1}{\rho_0}\frac{\partial}{\partial y}\left(\hat{v}_n^{\sim S}\hat{p}_n^{\sim S}\right)$$

$$\Delta_z Q_{P_n^S} = -\frac{1}{\rho_0}\frac{\partial}{\partial z}(\hat{w}_n^{\sim S}\hat{p}_n^{\sim S})$$

$$b_n^S = -\frac{g}{\rho_0}\hat{w}_n^{\sim S}\hat{\rho}_n^{\sim S}$$

d) Friction terms:

This terms depends on the particular subgrid parameterization of the model. If we consider a laplacian operator for both the lateral and vertical dissipation. Hence: $\mathbf{F}_{mh} = \nabla\left(A_h\nabla\mathbf{v}\right)$ $F_{mv} = \frac{\partial}{\partial z}\left(A_v\frac{\partial\mathbf{v}}{\partial z}\right)$, where A_h, A_z are the horizontal and vertical viscosities for the momentum equations.

$$\text{FRICTION TERMS} = \mathbf{F}^S{}_{n,mh} + F^S_{n,mv}$$

$$\mathbf{F}^S{}_{n,mh} = \hat{\mathbf{v}}_n^{\sim S}\nabla A_h(\nabla\hat{\mathbf{v}}_n^{\sim S})$$

$$F^S_{n,mv} = \hat{\mathbf{v}}_n^{\sim S}\frac{\partial}{\partial z}A_v\frac{\partial\hat{\mathbf{v}}_n^{\sim S}}{\partial z}$$

Available Potential Energy

The available potential energy of each window S, at location n, is defined as:

$$A_n^S = 2^{j_2}\frac{g^2}{\rho_0^2 N^2}(\hat{\rho}_n^{\sim S})^2 = 2^{j_2}c(\hat{\rho}_n^{\sim S})^2 \qquad \text{(A.4)}$$

By taking dot product of the buoyancy equation with $c(\hat{\rho}_n^{\sim S})$ and applying the MWT, we obtain the evolution equation for the A_n^S. All the terms are multiplied by 2^{j_2}. Schematically, it will be:

$$\overbrace{\hat{\delta}_n A^S}^{\text{Time rate of change of APE}} = \overbrace{\underbrace{\Delta_h Q_{A_n^S} + \Delta_z Q_{A_n^S}}_{\text{Transport}} + \underbrace{T_{A_n^S,\delta_h\rho} + T_{A_n^S,\delta_z\rho} + TS_{A_n^S}}_{\text{Transfer}}}^{\text{Advection terms}} \overbrace{+b_n^S}^{\text{Buoyancy}}$$
$$\overbrace{+\mathbf{F}^S{}_{n,\rho h} + F_{n,\rho v}^S}^{\text{Diffusion terms}} \tag{A.5}$$

Single terms

a) Time rate of change [3]

$$\hat{\rho}_n^{\sim S} \cdot \left[\hat{\delta}_n \hat{\rho}_n^{\sim S}\right] = \hat{\delta}_n A_n^S + (\Delta t)^2 c(\hat{\delta}_n^2 \hat{\rho}_n^{\sim S} \cdot \hat{\delta}_n \hat{\rho}_n^{\sim S})$$

b) Advection terms:

The advection terms in (A.5) give rise to the transport and transfer terms in the horizontal and vertical directions. There is another term that we will include in the transfers, TSA, arising from the c dependence on z, and representing a source/sink of APE from the background density.

$$\text{TRANSPORT} = \Delta_h Q_{A_n^S} + \Delta_z Q_{A_n^S} = \Delta_x Q_{A_n^S} + \Delta_y Q_{A_n^S} + \Delta_z Q_{A_n^S}$$
$$\text{TRANSFERS} = T_{A_n^S,\delta_h\rho} + T_{A_n^S,\delta_z\rho} + TS_{A_n^S} = T_{A_n^S,\delta_x\rho} + T_{A_n^S,\delta_y\rho} + T_{A_n^S,\delta_z\rho} + TS_{A_n^S}$$

Where:

$$\Delta_x Q_{A_n^S} = -\frac{\partial}{\partial x}\frac{1}{2}c\hat{\rho}_n^{\sim S}\widehat{(u\rho)}_n^{\sim S}$$

$$\Delta_y Q_{A_n^S} = -\frac{\partial}{\partial y}\frac{1}{2}c\hat{\rho}_n^{\sim S}\widehat{(v\rho)}_n^{\sim S}$$

$$\Delta_z Q_{A_n^S} = -\frac{\partial}{\partial z}\frac{1}{2}c\hat{\rho}_n^{\sim S}\widehat{(w\rho)}_n^{\sim S}$$

---

[3] The time rate of change is computed in a way similar to finite differences:

$$\hat{\delta}_n A^S = \frac{1}{2\Delta t}\left(\frac{1}{2}c\hat{\rho}_n^{\sim S}\cdot\hat{\rho}_n^{\sim S}\right); \quad \hat{\delta}_n\hat{\rho}_n^{\sim S} = \frac{\hat{\rho}_{n+}^{\sim S} - \hat{\rho}_{n-}^{\sim S}}{2\Delta t}; \quad \hat{\delta}_n^2\hat{\rho}_n^{\sim S} = \frac{\hat{\rho}_{n+}^{\sim S} + 2\hat{\rho}_n^{\sim S} - \hat{\rho}_{n-}^{\sim S}}{(\Delta t)^2}$$

$$T_{A_n^S,\delta_x\rho} = -c\hat{\rho}_n^{\sim S}\frac{\partial}{\partial x}\widehat{(u\rho)}_n^{\sim S} - \Delta_x Q_{A_n^S} + \frac{1}{2}\widehat{(\rho\rho)}_n^{\sim S}\frac{\partial}{\partial x}\hat{u}_n^{\sim S}$$

$$T_{A_n^S,\delta_y\rho} = -c\hat{\rho}_n^{\sim S}\frac{\partial}{\partial y}\widehat{(v\rho)}_n^{\sim S} - \Delta_y Q_{A_n^S} + \frac{1}{2}\widehat{(\rho\rho)}_n^{\sim S}\frac{\partial}{\partial y}\hat{v}_n^{\sim S}$$

$$T_{A_n^S,\delta_z\rho} = -c\hat{\rho}_n^{\sim S}\frac{\partial}{\partial z}\widehat{(w\rho)}_n^{\sim S} - \Delta_z Q_{A_n^S} + \frac{1}{2}\widehat{(\rho\rho)}_n^{\sim S}\frac{\partial}{\partial z}\hat{w}_n^{\sim S} + TS_{A_n^S}$$

$$TS_{A_n^S} = \frac{1}{2}\hat{\rho}_n^{\sim S}\widehat{(w\rho)}_n^{\sim S}\frac{\partial c}{\partial z} = -\frac{1}{2}\hat{\rho}_n^{\sim S}\widehat{(w\rho)}_n^{\sim S}\frac{\partial logN^2}{\partial z}$$

c) Buoyancy:

$$b_n^S = \frac{g}{\rho_0}\hat{w}_n^{\sim S}\hat{\rho}_n^{\sim S}$$

The Baroclinic Instability term is the sum of all the transferences of APE, considering only the mixed terms between scales 0 and 1.

$$BC = T^{0\to 1}_{A_n^S,\delta_h\rho} + T^{0\to 1}_{A_n^S,\delta_z\rho} + TS^{0\to 1}_{A_n^S}$$

Connection with classical formulation

Kinetic energy

The KE equation for any window $S = 0, 1$ is (friction omitted here):

$$\hat{\mathbf{v}}_n^{\sim S}\cdot\widehat{\left(\frac{\partial\mathbf{v}}{\partial t}\right)}_n^{\sim S} = \hat{\mathbf{v}}_n^{\sim S}\cdot\left[-\nabla\cdot\widehat{(\mathbf{vv})}_n^{\sim S} - \frac{\partial}{\partial z}\widehat{(w\mathbf{v})}_n^{\sim S}\right] + \Delta_h Q_{P_n^S} + \Delta_z Q_{P_n^S} - b_n^S$$

Considering $j_0 = 0, j_1 = j_2$ and a periodic extension, MS-EVA is analogous to the classical mean-eddy formulation. With this configuration, the total field is divided into:

$$q = q^{\sim 0} + q^{\sim 1}$$

And we know that with $j_0 = 0$ and a periodic extension the large scale reconstruction is equal to the time mean:

$$q^{\sim 0} = \bar{q} = 2^{j_2/2}\hat{q}_n^{\sim 0}$$

Therefore, the meso scale reconstruction is equal to the fluctuation:

$$q^{\sim 1} = q - q^{\sim 0} = q - \bar{q} = q'$$

Keeping this relation in mind, the equations of the large scale and mesoscale energy can be rewritten in terms of the mean and eddy flow. The final equations are equal to the MKE (mean KE) and MKEF (Mean KE of the eddy flow) equations in Harrison and Robinson (1978).

Large scale KE and MKE

The large scale energy:

$$K_n^L = 2^{j_2}\left(\frac{1}{2}\hat{\mathbf{v}}_n{}^{\sim 0}\hat{\mathbf{v}}_n{}^{\sim 0}\right) = \frac{1}{2}\bar{\mathbf{v}}\cdot\bar{\mathbf{v}} = MKE$$

$$\hat{\mathbf{v}}_n{}^{\sim 0}\cdot\widehat{\left(\frac{\partial \mathbf{v}}{\partial t}\right)}_n^{\sim 0} = \hat{\mathbf{v}}_n{}^{\sim 0}\cdot\left[-\nabla\cdot\widehat{(\mathbf{v}\mathbf{v})}_n^{\sim 0} - \frac{\partial}{\partial z}\widehat{(w\mathbf{v})}_n^{\sim 0}\right] + \Delta_h Q_{P_n^0} + \Delta_z Q_{P_n^0} - b_n^0$$

where the LHS is the large scale energy tendency; in the RHS, the first term contains all the transport and transfer terms, the second and third terms are the pressure work, and the last term is the buoyancy conversion. Rewritten in terms of the mean-eddy decomposition the equation reads:

$$\bar{\mathbf{v}}\cdot\overline{\left(\frac{\partial \mathbf{v}}{\partial t}\right)} = -\nabla\cdot(\bar{\mathbf{v}}MKE) - \frac{\partial}{\partial z}(\bar{w}MKE) + \bar{\mathbf{v}}\cdot\nabla_3\cdot\underline{\underline{\mathbf{T}}} - \frac{1}{\rho_0}\nabla\cdot(P\bar{\mathbf{v}}) - \frac{1}{\rho_0}\frac{\partial}{\partial z}(P\bar{w}) - \frac{g}{\rho_0}\bar{w}\bar{\rho}$$

where:

$$\nabla_3 = \mathbf{i}\frac{\partial}{\partial x} + \mathbf{j}\frac{\partial}{\partial y} + \mathbf{k}\frac{\partial}{\partial z}$$

, and

$$\underline{\underline{\mathbf{T}}} = \begin{bmatrix} -\overline{(u'u')} & -\overline{(u'v')} & -\overline{(u'w')} \\ -\overline{(v'u')} & -\overline{(v'v')} & -\overline{(v'w')} \\ -\overline{(w'u')} & -\overline{(w'v')} & -\overline{(w'w')} \end{bmatrix}$$

Meso scale KE and MKEF

For the meso scale there is no a linear relation between $\hat{q}_n^{\sim 1}$ and q', as in the large scale. We need to marginalize the meso scale KE equation (that is, after averaging the mesoscale over all the time locations) to obtain an equation equivalent to the mean eddy KE equation in Harrison and Robinson (1978).

The marginalized meso scale KE is:

$$\overline{K_n^M} = 2^{j_2}\left(\frac{1}{2}\overline{\hat{\mathbf{v}}_n{}^{\sim 1}\hat{\mathbf{v}}_n{}^{\sim 1}}\right) = \frac{1}{2}\overline{\mathbf{v}' \cdot \mathbf{v}'} = MKEF$$

$$\overline{\mathbf{v}' \cdot \left(\frac{\partial \mathbf{v}'}{\partial t}\right)} = -\overline{\mathbf{v}' \cdot \nabla \cdot (\mathbf{v}\mathbf{v})'} - \overline{\mathbf{v}' \cdot \frac{\partial}{\partial z}(w\mathbf{v})'} - \overline{\mathbf{v}' \cdot \nabla\left(\frac{P}{\rho_0}\right)}$$

where the LHS is the meso scale energy tendency; in the RHS, the first and second term give rise to all the transport and transfer terms, and the third term is to the pressure work and buoyancy conversion. Rewritten in terms of the mean-eddy decomposition:

$$\begin{aligned}\overline{\mathbf{v}' \cdot \left(\frac{\partial \mathbf{v}'}{\partial t}\right)} = & -\nabla \cdot \overline{\left(\mathbf{v}\frac{\mathbf{v}' \cdot \mathbf{v}'}{2}\right)} - \frac{\partial}{\partial z}\overline{\left(w\frac{\mathbf{v}' \cdot \mathbf{v}'}{2}\right)} - \overline{\mathbf{v}'\mathbf{v}'} : \nabla\bar{\mathbf{v}} - \overline{\mathbf{v}'w'} \cdot \frac{\partial \bar{\mathbf{v}}}{\partial z} \\ & -\nabla \cdot \overline{\left(\mathbf{v}'\frac{P'}{\rho_0}\right)} - \frac{\partial}{\partial z}\overline{\left(\mathbf{v}'\frac{P'}{\rho_0}\right)} - \frac{g}{\rho_0}\overline{w'\rho'}\end{aligned}$$

Available potential energy

The same approach is followed for the APE to obtain equivalent MAPE (APE of the mean flow) and MAPEF (mean APE of the eddy flow) equations (Tennekes and Lumley, 1972). The APE equation for any window $S = 0, 1$ is (without diffusion):

$$c_n^{\sim S}\rho \cdot \widehat{\left(\frac{\partial \rho}{\partial t}\right)}_n^{\sim S} = c_n^{\sim S}\rho \cdot \left[-\nabla \cdot \widehat{(\mathbf{v}\rho)}_n^{\sim S} - \frac{\partial}{\partial z}\widehat{(w\rho)}_n^{\sim S}\right] + b_n^S$$

Large scale APE and MAPE

The large scale energy:

$$A_n^L = 2^{j_2}\left(\frac{1}{2}c\hat{\rho}_n{}^{\sim 0}\hat{\rho}_n{}^{\sim 0}\right) = \frac{1}{2}c\bar{\rho}^2 = MAPE$$

$$c\hat{\rho}_n{}^{\sim 0} \cdot \widehat{\left(\frac{\partial \rho}{\partial t}\right)}_n^{\sim 0} = c\hat{\rho}_n{}^{\sim 0} \cdot \left[-\nabla \cdot \widehat{(\mathbf{v}\rho)}_n^{\sim 0} - \frac{\partial}{\partial z}\widehat{(w\rho)}_n^{\sim 0}\right] + b_n^0$$

The LHS is the tendency, and the terms in the RHS are the transport/transfers and buoyancy conversion. [4] Rewritten in terms of the mean-eddy decomposition:

$$\overline{c\rho \cdot \left(\frac{\partial \rho}{\partial t}\right)} = -\nabla \cdot (\bar{\mathbf{v}} MAPE) - \frac{\partial}{\partial z}(\bar{w} MAPE) - c\bar{\rho}\nabla \cdot (\overline{\mathbf{v}'\rho'}) - c\bar{\rho}\frac{\partial}{\partial z}(\overline{w'\rho'}) + \frac{g}{\rho_0}\bar{w}\bar{\rho}$$

Meso scale APE and MAPEF

The meso scale APE equation is:

$$\overline{A_n^M} = 2^{j_2}\left(\frac{1}{2}\overline{c\hat{\rho}_n{}^{\sim 1}\hat{\rho}_n{}^{\sim 1}}\right) = \frac{1}{2}c\overline{\rho'^2} = MAPEF$$

$$\overline{c\rho' \cdot \left(\frac{\partial \rho'}{\partial t}\right)} = \overline{c\rho' \cdot \left[- \nabla \cdot (\mathbf{v}\rho)' - \frac{\partial}{\partial z}(w\rho)' \right]} + \frac{g}{\rho_0}\overline{w'\rho'}$$

The LHS is the tendency, and the terms in the RHS are the transport/transfers and buoyancy conversion. Rewritten in terms of the mean-eddy decomposition:

$$\overline{c\rho' \cdot \left(\frac{\partial \rho'}{\partial t}\right)} = -\nabla \cdot \overline{\left(\mathbf{v} \cdot \frac{c\rho'\rho'}{2}\right)} - \frac{\partial}{\partial z}\overline{\left(w\frac{c\rho'\rho'}{2}\right)} - c(\overline{\rho'\mathbf{v}'}) \cdot \nabla\bar{\rho} - c(\overline{\rho' w'})\frac{\partial \bar{\rho}}{\partial z} + \frac{g}{\rho_0}\overline{w'\rho'}$$

---

[4] The apparent source/sink of energy due to the background density profile coming out from the z dependence of c has been omitted.

Bibliography

Allen, J., P. A. Newberger, and J. Federiuk, 1995: Upwelling circulation on the oregon continental shelf. Part I: Response to idealized forcing. *Journal of Physical Oceanography*, **25 (8)**, 1843–1866.

Antonijuan Rull, J., J. Guillem, G. Simarro, M. Nogueras Cervera, and J. del Río Fernandez, 2015: Characterization of coastal upwelling events during the generation of the water column stratification in spring (vilanova i la geltrú, NW Mediterranean). *Oceans 2015 MTS/IEEE*, Institute of Electrical and Electronics Engineers (IEEE).

Arakawa, H., 1953: On the time rate of work done by the eddy stresses in the free air, and the maintenance of the westerlies in middle latitudes. *Tellus*, **10 (5)**, 392–393.

Bakun, A., and V. Agostini, 2001: Seasonal patterns of wind-induced upwelling/downwelling in the Mediterranean Sea. *Scientia Marina*, **65 (3)**, 243–257.

Berkooz, G., P. Holmes, and J. Lumley, 1993: The proper orthogonal decomposition in the analysis of turbulent flows. *Annual review of fluid mechanics*, **25 (1)**, 539–575.

Brink, K., 1983: The near-surface dynamics of coastal upwelling. *Progress in Oceanography*, **12 (3)**, 223–257.

Cavicchia, L., S. Gualdi, A. Sanna, and P. Oddo, 2015: The regional ocean–atmosphere coupled model COSMO—NEMO–MFS. *CMCC Research Paper*, **(RP0254)**.

Charney, J. G., 1947: The dynamics of long waves in a baroclinic westerly current. *Journal of Meteorology*, **4 (5)**, 136–162.

Choboter, P., D. Duke, J. Horton, and P. Sinz, 2011: Exact solutions of wind-driven coastal upwelling and downwelling over sloping topography. *Journal of Physical Oceanography*, **41 (7)**, 1277–1296.

Cushing, D., 1971: Upwelling and the production of fish. *Advances in marine biology*, **9**, 255–334, review upwelling, physics and biology.

Daubechies, I., 1992: *Ten lectures on wavelets*, Vol. 61. SIAM, 198–202 pp.

Eady, E., 1949: Long waves and cyclone waves. *Tellus*, **1 (3)**, 33–52.

Ekman, V., 1905: On the influence of the earth's rotation on ocean currents. *Arkiv för matematik, astronomi och fysik*, **2 (1)**, 1–53.

Estrada, M., 1996: Primary production in the northwestern Mediterranean. *Scientia Marina*, **60 (2)**, 55–64.

Estrade, P., P. Marchesiello, D. Verdière, A. Colin, and C. Roy, 2008: Cross-shelf structure of coastal upwelling: A two-dimensional extension of ekman's theory and a mechanism for inner shelf upwelling shut down. *Journal of marine research*, **66 (5)**, 589–616.

Ferrari, R., and C. Wunsch, 2008: Ocean circulation kinetic energy: Reservoirs, sources, and sinks. *Annual Review of Fluid Mechanics*, **41 (1)**, 253.

Fiúza, A. F., 1983: Upwelling patterns off Portugal. *Coastal Upwelling its sediment record*, Springer, 85–98.

Fjørtoft, R., 1953: On the changes in the spectral distribution of kinetic energy for twodimensional, nondivergent flow. *Tellus*, **5 (3)**, 225–230.

Fournier, A., 2002: Atmospheric energetics in the wavelet domain. Part I: Governing equations and interpretation for idealized flows. *Journal of the atmospheric sciences*, **59 (7)**, 1182–1197.

Gill, A. E., 1982: *Atmosphere-ocean dynamics*, Vol. 30. Academic press.

Giorgi, F., and P. Lionello, 2008: Climate change projections for the Mediterranean Region. *Global and Planetary Change*, **63 (2)**, 90–104.

Hansen, A., and T. Chen, 1982: A spectral energetics analysis of atmospheric blocking. *Monthly Weather Review*, **110 (9)**, 1146–1165.

Harrison, D., and A. Robinson, 1978: Energy analysis of open regions of turbulent flows: mean eddy energetics of a numerical ocean circulation experiment. *Dynamics of Atmospheres and Oceans*, **2 (2)**, 185–211.

Huang, R., 2004: Energy flows in ocean. *Encyclopedia of Energy*, **4**, 497–509.

Korres, G., N. Pinardi, and A. Lascaratos, 2000: The ocean response to low-frequency interannual atmospheric variability in the Mediterranean Sea. Part I: sensitivity experiments and energy analysis. *Journal of Climate*, **13 (4)**, 705–731.

Kuo, H., 1952: Three–dimensional disturbances in a baroclinic zonal current. *Journal of Meteorology*, **9 (4)**, 260–278.

Liang, X., 2002: Wavelet–based Multiscale Window Transform and Energy and Vorticity Analysis. Ph.D. thesis, Harvard University.

Liang, X., and D. Anderson, 2007: Multiscale Window Transform. *Multiscale Modeling & Simulation*, **6 (2)**, 437–467.

Liang, X., and A. Robinson, 2005: Localized multiscale energy and vorticity analysis I. Fundamentals. *Dynamics of Atmospheres and Oceans*, **38 (3-4)**, 195–230.

Liang, X., and A. Robinson, 2007: Localized multi–scale energy and vorticity analysis II. Finite–amplitude instability theory and validation. *Dynamics of Atmospheres and Oceans*, **44 (2)**, 51–76.

Liang, X., and A. Robinson, 2009: Multiscale processes and nonlinear dynamics of the circulation and upwelling events off Monterey Bay. *Journal of Physical Oceanography*, **39 (2)**, 290–313.

Lorenz, E., 1955: Available potential energy and the maintenance of the general circulation. *Tellus*, **7 (2)**, 157–167.

Madec, G., and the NEMO team, 2012: Nemo ocean engine v3. 4. *Note du Pole de modélisation*, **27**, URL `http://www.nemo-ocean.eu`.

Marchesiello, P., M. T. Gibbs, and J. Middleton, 2000: Simulations of coastal upwelling on the Sydney continental shelf. *Marine and freshwater research*, **51 (6)**, 577–588.

Margalef, R., and A. Ballester, 1967: Fitoplancton y producción primaria de la costa catalana, de junio de 1965 a junio de 1966. *Investigaciones Pesqueras*, **31 (1)**, 165–182.

Mieghem, J., 1952: Energy conversions in the atmosphere on the scale of the general circulation. *Tellus*, **4 (4)**, 334–351.

Minas, H., 1968: A propos d'une remontée d'eaux profondes dans les parages du golfe de marseille (octobre 1964): conséquences biologiques. *Cahier Oceanographique*, **20**, 647–674.

Molemaker, M., J. McWilliams, and X. Capet, 2010: Balanced and unbalanced routes to dissipation in an equilibrated Eady flow. *Journal of Fluid Mechanics*, **654**, 35–63.

Oddo, P., M. Adani, N. Pinardi, C. Fratianni, M. Tonani, and D. Pettenuzzo, 2009: A nested Atlantic–Mediterranean Sea general circulation model for operational forecasting. *Ocean science*.

Pedlosky, J., 1987: *Geophysical fluid dynamics*. 2nd ed., New York and Berlin, Springer-Verlag.

Phillips, N. A., 1956: The general circulation of the atmosphere: A numerical experiment. *Quarterly Journal of the Royal Meteorological Society*, **82 (354)**, 535–539.

Pinardi, N., and E. Masetti, 2000: Variability of the large scale general circulation of the Mediterranean Sea from observations and modelling: a review. *Palaeogeography, Palaeoclimatology, Palaeoecology*, **158 (3)**, 153–173.

Pinardi, N., and A. Robinson, 1986: Quasigeostrophic energetics of open ocean regions. *Dynamics of atmospheres and oceans*, **10 (3)**, 185–219.

Pujol, M., and G. Larnicol, 2005: Mediterranean sea eddy kinetic energy variability from 11 years of altimetric data. *Journal of Marine Systems*, **58 (3)**, 121–142.

Reynolds, O., 1895: On the dynamical theory of incompressible viscous fluids and the determination of the criterion. *Philosophical Transactions of the Royal Society of London. A*, 123–164.

Robinson, A., W. Leslie, A. Theocharis, and A. Lascaratos, 2001: Mediterranean sea circulation. *Ocean Currents: A Derivative of the Encyclopedia of Ocean Sciences*, 1689–1705.

Rockel, B., A. Will, and A. Hense, 2008: The regional climate model COSMO-CLM (CCLM). *Meteorologische Zeitschrift*, **17 (4)**, 347–348.

Rowe, G. T., and R. J. Menzies, 1968: Deep bottom currents off the coast of North Carolina. *Deep Sea Research and Oceanographic Abstracts*, Elsevier, Vol. 15, 711–719.

Saltzman, B., 1957: Equations governing the energetics of the larger scales of atmospheric turbulence in the domain of wave number. *Journal of Meteorology*, **14 (6)**, 513–523.

San Liang, X., 2016: Canonical transfer and multiscale energetics for primitive and quasigeostrophic atmospheres. *Journal of the Atmospheric Sciences*, **73 (11)**, 4439–4468.

Sapsis, T., and P. Lermusiaux, 2009: Dynamically orthogonal field equations for continuous stochastic dynamical systems. *Physica D: Nonlinear Phenomena*, **238 (23)**, 2347–2360.

Sapsis, T., M. Ueckermann, and P. Lermusiaux, 2013: Global analysis of Navier–Stokes and Boussinesq stochastic flows using dynamical orthogonality. *Journal of Fluid Mechanics*, **734**, 83–113.

Schmid, P., 2010: Dynamic mode decomposition of numerical and experimental data. *Journal of Fluid Mechanics*, **656**, 5–28.

Sorgente, R., A. Olita, P. Oddo, L. Fazioli, and A. Ribotti, 2011: Numerical simulation and decomposition of kinetic energy in the Central Mediterranean: insight on mesoscale circulation and energy conversion. *Ocean Science (OS)*.

Spall, M., 1989: Regional primitive equation modeling and analysis of the POLYMODE data set. *Dynamics of Atmospheres and Oceans*, **14**, 125–174.

Tennekes, H., and J. Lumley, 1972: *A first course in turbulence*. MIT press.

Valcke, S., 2013: The OASIS3 coupler: a European climate modeling community software. *Geoscientific Model Development*, **6 (2)**, 373–388.

Vallis, G., 2006: *Atmospheric and oceanic fluid dynamics: fundamentals and large–scale circulation*. Cambridge University Press.